



Barboni, M., Annen, C., & Schoene, B. (2015). Evaluating the construction and evolution of upper crustal magma reservoirs with coupled U/Pb zircon geochronology and thermal modeling: A case study from the Mt. Capanne pluton (Elba, Italy). *Earth and Planetary Science Letters*, 432, 436-448.

<https://doi.org/10.1016/j.epsl.2015.09.043>

Peer reviewed version

Link to published version (if available):
[10.1016/j.epsl.2015.09.043](https://doi.org/10.1016/j.epsl.2015.09.043)

[Link to publication record in Explore Bristol Research](#)
PDF-document

University of Bristol - Explore Bristol Research

General rights

This document is made available in accordance with publisher policies. Please cite only the published version using the reference above. Full terms of use are available:
<http://www.bristol.ac.uk/pure/user-guides/explore-bristol-research/ebr-terms/>

Evaluating the construction and evolution of upper crustal magma reservoirs with coupled U/Pb zircon geochronology and thermal modeling: A case study from the Mt. Capanne pluton (Elba, Italy)

Mélanie Barboni¹, Catherine Annen² and Blair Schoene³

¹ Department of Earth, Planetary and Space Sciences, University of California Los Angeles

Phone number: +1 (609) 510 4782; Fax number: +1 (310) 825 2279; Email: mbarboni@epss.ucla.edu

2 School of Earth Sciences, University of Bristol (UK)

3 Department of Geosciences, Princeton University

Keywords: U-Pb geochronology; ID-TIMS; zircon; heat transfer; magma reservoir; volcanic-plutonic connection

Abstract

Evaluating mechanisms and rates for magma transport and emplacement in the upper crust is important in order to predict the thermal and rheological state of the crust, and understand the relationship between plutonism and volcanism. U-Pb geochronology on zircon is commonly used to constrain magma emplacement and storage time in the crust, but interpreting complex zircon age populations in terms of in-situ crystallization versus crystallization at a deeper level is not trivial. This study focuses on the Mt. Capanne pluton in Elba (Italy), a well-documented example of arc-related laccolith emplaced in the upper continental crust. Previous studies proposed that the Mt. Capanne intrusion was accreted in less than 10,000 years by distinct and mappable magma pulses. Here, we couple high-precision ID-TIMS U-Pb zircon geochronology with numerical

26 thermal simulations to evaluate emplacement rates, test different emplacement models, inform
27 zircon age interpretations and evaluate the potential for melt storage during construction of the
28 Mt. Capanne pluton. Our results require that the Mt. Capanne intrusion was built in at least
29 300,000 years by multiple magma injections. A variety of emplacement scenarios show that melt
30 was preserved for < 60'000 years after each pulse and that the maximum eruptible volumes were
31 approximately equal to the volume of each pulse. Our results also require that the majority of
32 zircon crystallization occurred in zircon saturated reservoirs at deeper crustal levels prior to final
33 magma emplacement and cooling, which has implications for using zircon U-Pb geochronology
34 to infer upper crustal magma residence times.

35

36 **1. Introduction**

37

38 The flux of magma to the upper crust plays an important role in how continental crust is made
39 and the relationship between volcanic and plutonic systems (e.g. Lipman, 2007; Bartley, 2008;
40 Glazner et al., 2004; Deering et al., 2011; Miller and Miller, 2002; Miller et al., 2011; Bachmann
41 et al., 2007). Low upper crustal temperatures and the associated brittle rheology of host rocks
42 limit the rate at which large magma bodies can be emplaced (Clemens, 1992; Coleman et al.,
43 2004), which has led to the hypothesis that many igneous bodies grow incrementally by accretion
44 of smaller sills and dikes (e.g. Coleman et al., 2004; Lipman, 2007; Menand, 2011). Therefore,
45 geochronology that constrains magma emplacement rates into the upper crust is important for
46 building models linking magma reservoirs with volcanic and plutonic products (e.g. Barboni and
47 Schoene, 2014).

48 Plutons are time-integrated records of magma reservoirs residing beneath volcanic systems (e.g.
49 Bachmann et al., 2007; de Silva and Gosnold, 2007; Bartley, 2008; Menand et al., 2015), and

50 deciphering intrusion geometries and emplacement modes is critical to testing models for
51 volcanic-plutonic systems (Farina et al., 2010). However, interpreting plutonic records in the field
52 is rarely straightforward, as critical information such as contacts between different sills or pulses
53 and original magmatic textures (Bartley, 2008) can be obscured. Quantifying models for upper
54 crustal pluton construction thus involves a combination of thermal and mechanical models tested
55 by field observation, geophysics, petrology and geochronology.

56 Heat transfer calculations using a range of “typical” magma emplacement rates show that in the
57 cool shallow crust successive magma pulses separated by long time intervals solidify before the
58 next one is emplaced (Annen, 2009; Schöpa and Annen, 2013; de Saint Blanquat et al., 2010).
59 This has led some authors to consider that upper crustal magma chambers with volumes
60 equivalent to plutons are rare and short-lived (Glazner et al., 2004; Coleman et al., 2004; de Saint
61 Blanquat et al., 2010). However, further evidence from thermal models (Annen, 2009; Gelman et
62 al., 2013) has shown that high magma emplacement rates can result in magma chambers
63 equivalent in size to large-volume ignimbrites associated with caldera collapse (Lipman, 2007;
64 Bachmann and Bergantz, 2008). Testing model results with examples from the geologic record
65 requires estimates of magma flux in the crust derived from geochronology (e.g. Caricchi et al.,
66 2014). U-Th-Pb and U-series geochronology of magmatic accessory minerals have been used to
67 infer rates of emplacement and melt storage in the crust (e.g. Coleman et al., 2004; Schmitt et al.,
68 2011; Schoene et al., 2012; Barboni and Schoene., 2014). However, an increasing number of
69 studies from both plutonic and volcanic rocks reveal complexities in zircon age populations that
70 are difficult to interpret in terms of emplacement time (e.g. Lissenberg et al., 2009; Schoene et al.,
71 2012). In essence, the ability of zircon to retain age information at magmatic temperatures –
72 which itself makes zircon such an attractive geochromometer in magmatic systems – also increases

73 its propensity to record protracted crystallization and recycling that obscure the connection
74 between zircon date and magma emplacement rates.

75 In this study, we couple high-precision U-Pb zircon geochronology with thermal modeling to
76 test models of pluton construction. We use differing interpretations of zircon dates to model
77 magma emplacement rates, and use the model results to in turn place constraints on zircon age
78 interpretations. Our case study is the Miocene Mt. Capanne intrusion located on Elba Island
79 (Italy), which is a well-documented example of an upper-crustal laccolith (e.g. Westerman et al.,
80 2004; Rocchi et al., 2010). Previous work has proposed that different mappable magma batches
81 contributed to pluton construction (Farina et al., 2010), therefore providing an excellent
82 opportunity to test and refine the incremental emplacement paradigm for upper crustal plutons
83 and to measure the potential for such systems to generate and store eruptible liquid.

84

85 **2. Geological background**

86

87 Elba Island formed behind the eastwards-progressing compressive front of the Apennine
88 orogeny (Malinverno and Ryan, 1986) during the stacking of five tectonic complexes in the early
89 Miocene. The arc-related Elba intrusive complex was emplaced as a nested “Christmas-tree”
90 laccolith at ca. 6 km depth within the tectonic complexes in what is now western and central Elba
91 (Fig. 1; Rosenbaum and Lister, 2004; Gasparon et al., 2009; Bussy, 1991; Westerman et al.,
92 2004; Rocchi et al., 2010). Crosscutting relationships show the following sequence of intrusion
93 (Westerman et al., 2004; Farina et al., 2010; Rocchi et al., 2010; Fig.1): The Capo Bianco aplite,
94 the Portoferraio porphyry, the San Martino porphyry, the ca. ~200 km³ Mt. Capanne granitic
95 pluton, and lastly late dykes of intermediate compositions (Orano dyke swarm; Fig.1; Dini et al.,
96 2008).

97 Early intrusions such as the Capo Bianco aplite and the Portoferraio porphyry have been
98 interpreted as anatetic crustal melts. Large chemical variability within the later intermediate to
99 felsic pluton facies and within individual megacrystic K-feldspars have been used to generate
100 models whereby the magma mixing and mingling occurred at lower crustal depths synchronous
101 with upper crustal emplacement of the Mt. Capanne pluton (Dini et al., 2002; Dini et al., 2004;
102 Farina et al., 2010; Gagnevin et al., 2004; Gagnevin et al., 2005; Gagnevin et al., 2008;
103 Westerman et al., 2004). Several mixing models have been proposed to explain variation
104 observed in the Elba magmatic system. Liquid-liquid mixing of mantle and crustal melts has
105 been used to explain textures and chemical/isotopic zoning in plagioclase and K-feldspar within
106 the Mt. Capanne granite (e.g. Bussy, 1991; Gagnevin et al., 2004; Dini et al., 2002). Previously
107 hybridized products, represented in the field by abundant mafic microgranular enclaves in the Mt.
108 Capanne facies, were also proposed as potential mixing sources (e.g. Bussy, 1991; Dini et al.,
109 2002). Melt-solid interaction such as assimilation and fragmentation of cumulates has also been
110 used to explain isotopic variability and observed feldspar xenocrysts (Bussy, 1991). Farina et al.
111 (2012), however, proposed that much of the chemical and isotopic variability observed is related
112 to progressive lower- to mid-crustal anatexis of isotopically heterogeneous sources, and that
113 hybridization was most important in generating the intermediate Orano dykes and mafic enclaves
114 of the Mt. Capanne granite.

115

116 **3. Model for the Mt. Capanne pluton construction**

117

118 The calc-alkaline Mt. Capanne pluton has monzogranitic composition (SiO_2 between 66 and 70
119 wt%) and slightly peraluminous character (ASI=1.11) (Dini et al., 2002; Farina et al., 2012).
120 Farina et al. (2010) distinguish three geochemically- and texturally-distinct facies within the Mt.

121 Capanne pluton that correlate with the abundance of K-feldspar megacrysts. The Sant'Andrea
122 facies (SA) contains the highest content of megacrysts and mafic enclaves and is mostly
123 preserved along the pluton margin and at high elevation (Fig.1), suggesting it forms the roof of
124 the pluton (Farina et al., 2010; Westerman et al., 2015). The San Piero (SP) is the structurally
125 lowest facies and contains a low abundance of K-feldspar megacrysts and mafic enclaves. The
126 two facies display subtle but systematic geochemical differences such as higher SiO₂ contents and
127 biotite Mg# in the SA compared to the SP (Farina et al., 2010). The San Francesco facies (SF) is
128 intermediate between the SA and SP in geochemical signature, K-feldspar megacryst content, and
129 structural level. Westerman et al. (2015) interpreted the three facies as three distinct magma
130 batches that were emplaced from the top down (i.e., under accretion) in the order SA, SF, SP.
131 Injection of the SF and SP successively deformed the preexisting sheets into the geometry
132 observed today (Farina et al., 2010; Westerman et al., 2015; Fig.1). Construction by under-
133 accretion is supported by the absence of feeder dikes and contractional strain in the roof (Farina
134 et al., 2010). The original diameters and thicknesses of the SA, SF and SP sills are estimated at
135 9.5x0.25, 9.0x0.65 and 8.0x1.5 km, respectively (Farina et al., 2010), yielding to volumes of
136 about 17, 41 and 75 km³ (assuming a cylinder geometry; Table 2). Although the dimensions of
137 SA and SF are derived from field observations, the thickness of the SP facies has been estimated
138 through a magnetic data model (Dini et al., 2008). Only the top of the SP is outcropping and the
139 buried portion may be composed of another facies, and the possibility that the Mt. Capanne
140 intrusion is thicker than proposed by Dini et al. (2008) cannot be excluded at present.

141 A striking feature of the Mt. Capanne pluton is the absence of clear contacts between the
142 different pulses of Farina et al., (2010). This led these authors to propose that melt was preserved
143 between injections, and using a simple numerical model, concluded that the whole Mt. Capanne

144 intrusion was built in less than 10,000 years. Barboni and Schoene, (2014) showed that one
145 facies of the Cappane (SA) intruded and cooled to below its solidus in <40 ka, but could not
146 further test the Farina et al. (2010) model for the whole pluton. A recent study by Gagnevin et al.
147 (2011) presented U-Pb dates on zircon by Secondary Ion Mass Spectrometry (SIMS) from the
148 Mt. Capanne pluton, and found no age differences within the pluton. Those data are consistent
149 with rapid intrusion of the Mt. Capanne pluton but large uncertainties on single zircons ($\geq \pm 0.15$
150 Ma) prevent a rigorous testing of the intrusion model of Farina et al. (2010).

151

152 **4. ID-TIMS U-Pb geochronology**

153

154 *4.1. sample description*

155

156 In this study, we carry out U-Pb geochronology on zircon using Isotope Dilution Thermal
157 Ionization Mass Spectrometry (ID-TIMS), which provides the temporal resolution necessary to
158 test incremental emplacement models for the Mt. Capanne pluton. Sample locations are shown in
159 Fig.1 and representative CL images of zircon are presented in Fig. 2. Additional CL images are
160 given in Supplementary Materials. Detailed descriptions of hand samples, zircon populations, and
161 field photos are given in the Supplementary Materials. One sample each of the Portoferraio
162 (MB11-11) and San Martino (MB11-14) porphyries, as well as six samples from the Mt. Capanne
163 intrusion and one sample from the Orano dykes were collected for U-Pb ID-TIMS analysis.
164 Following the nomenclature of Farina et al., (2010), we collected two samples from the San Piero
165 facies (MB11-1 and MB11-2, elevation of 150 and 350 m respectively), two from the San
166 Francesco facies (MB12-4 and MB12-8, elevation of 608 and 1000 m respectively) and two from
167 the Sant'Andrea facies (MB11-6 and MB12-9, elevation of 0 and 50 m respectively). Unfolding

168 the sills to estimate the geometry at the time of emplacement following the model of Farina et al.
169 (2010), the SP samples would have been close to the same structural level. On the other hand, the
170 SA and SF samples represent a range of depths within the sheets. MB11-6 would have been ca.
171 150 m higher than MB12-9, which is located close from the contact with the SF facies (Fig.1).
172 MB12-4 would have been ca. 100 m higher than MB12-8 in the SF sheet. The Orano sample was
173 collected from a dyke crosscutting the Sant'Andrea facies (Fig.1; Supplement Fig.1).

174

175 *4.2 ID-TIMS U-Pb geochronology*

176

177 A total of 164 zircons were measured for U-Pb ID-TIMS geochronology. CL imaging was
178 performed on each grain before dissolution to identify old metamorphic cores and characterize
179 growth zoning. When visible cores were present, zircons were broken so that only the tips were
180 dissolved and analyzed (Fig. 2). Many zircons showed complex magmatic textures, but our dating
181 of ~200 zircons from Elba (including the data presented in Barboni and Schoene, 2014) illustrates
182 qualitatively that intragrain complexity does not correlate with date (Fig. 2; Supplementary
183 Material). Fig. 1 presents the $^{206}\text{Pb}/^{238}\text{U}$ dates for each sample. A detailed methodology section
184 and data tables can be found in the Supplementary Material. All uncertainties in the text, figures,
185 tables and supplements are reported to the 2-sigma level and include internal uncertainties only.

186 Fourteen zircons were analyzed from the Portoferraio porphyry and the results show a spread
187 of $^{206}\text{Pb}/^{238}\text{U}$ dates ranging from 7.942 ± 0.008 to 8.009 ± 0.012 Ma ($\Delta t = 67 \pm 14$ ka). A cluster of 9
188 zircons yield a weighted mean of 8.001 ± 0.002 Ma (MSWD of 2.3), which does not overlap with
189 the youngest zircon measured in the sample (7.942 ± 0.008 Ma; Fig.1). Sixteen zircons were
190 analyzed for the San Martino porphyry (data published in Barboni and Schoene, 2014). $^{206}\text{Pb}/^{238}\text{U}$
191 ages spread between 7.437 ± 0.011 and 7.947 ± 0.005 Ma, with most of the ages ranging between

192 7.437±0.011 to 7.541±0.006 Ma ($\Delta t=105\pm12$ ka). Weighted means yield unreasonably high
193 MSWDs of >100 (Wendt and Carl, 1991). Three grains are distinctively older (7.783, 7.947 and
194 9.149 Ma).

195 Thirty-two zircons were analyzed for the Sant'Andrea facies of the Mt. Capanne pluton
196 (twenty for MB11-6; previously published in Barboni and Schoene, 2014; and twelve for MB12-
197 9; Fig.1). Both samples show a large spread in $^{206}\text{Pb}/^{238}\text{U}$ dates with data spanning over 0.3 Ma
198 ($\Delta t=331\pm8$ ka; Fig.1), from 7.236±0.005 to 7.567±0.006 Ma (ignoring older outliers at 7.65 and
199 7.87 Ma; Fig.1). MB12-9 yields younger dates compared to MB11-6 (youngest zircons of
200 7.236±0.005 and 7.323±0.019 Ma, respectively).

201 Forty-three zircons were analyzed for the San Francesco Facies (twenty-seven for MB12-4 and
202 sixteen for MB12-8; Fig.1). Most $^{206}\text{Pb}/^{238}\text{U}$ ages span between 7.166±0.007 and 7.404±0.005
203 Ma ($\Delta t=238\pm9$ ka), with four older outliers in sample MB12-4 (from 7.563±0.005 to 9.316±0.006
204 Ma) and one in MB12-8 (7.715±0.028 Ma). The youngest zircons from both samples overlap
205 within uncertainties at 7.166±0.007 Ma (MB12-4) and 7.171±0.005 Ma (MB12-8).

206 Thirty-seven zircons were analyzed from the San Piero facies (fifteen for MB11-1 and twenty-
207 two for MB11-2). The SP samples display the largest spread in $^{206}\text{Pb}/^{238}\text{U}$ ages within the Mt.
208 Capanne pluton ($\Delta t=531\pm9$ ka), between 7.007±0.007 and 7.538±0.005 Ma (excluding older
209 outlier at 7.72, 7.81, 12.06 and 12.74 Ma; Fig.1; Supplement Table 1). The youngest zircon from
210 MB11-1 overlaps within uncertainties with the youngest zircon from MB11-2 (7.007±0.007 and
211 7.009±0.004 Ma, respectively).

212 Twenty-six zircons were measured for the Orano dyke sample (Fig.1). Similar to the Mt.
213 Capanne intrusion samples, a large spread in $^{206}\text{Pb}/^{238}\text{U}$ ages is observed ($\Delta t=423\pm9$ ka), ranging
214 from 7.080±0.005 to 7.503±0.007 Ma (with two older out layers at 7.73 and 7.90 Ma).

216 4.3 U-Pb results: Summary

217

218 All the samples measured in this study display a large spread in $^{206}\text{Pb}/^{238}\text{U}$ dates of ca. 200-
219 400 ka (with average uncertainties of ± 8 ka), raising the question of the significance of any single
220 date or series of dates in terms of magma emplacement and solidification. We suggest two end-
221 member interpretations of the zircon record given the constraint that all analyzed zircons show
222 magmatic zoning (Fig. 2) and therefore crystallized in the presence of melt: (1) the youngest date
223 represents the best estimate for intrusion and the older dates correspond to zircon recycling from
224 a deeper level of the system, and (2) the oldest grain represents post-emplacement zircon
225 saturation and all other dates represent in situ growth. Below we use numerical thermal modeling
226 to test these possibilities.

227

228 5. Thermal model setup

229

230 We numerically simulated the assembly of the Mt. Capanne pluton by addition of sills and
231 calculated the evolution of temperature and melt fraction in the igneous body and country rock
232 system. The equation of heat:

234

$$238 \rho c \frac{\partial T}{\partial t} + \rho L \frac{\partial f}{\partial t} = k \nabla^2 T \quad (1)$$

239 where ρ is density, c is specific heat, T is temperature, L is latent heat of crystallization or fusion,
240 f is melt fraction, and k is thermal conductivity, was solved with an explicit finite difference
241 scheme on a 2D numerical grid using cylindrical coordinates. The numerical domain extends
242 from the surface to a depth of 13 km and radially to a distance of 10 km from the central axis of

243 symmetry. We used $\rho = 2700 \text{ kg/m}^3$ (Rocchi et al., 2010), $c = 1200 \text{ J/kg K}$ (Robertson, 1988) and
244 $L = 3.5 \times 10^5 \text{ J/kg}$ (Hale et al., 2007). The conductivity k varies with temperature as in
245 Whittington et al. (2009). More information on the numerical method can be found in Annen et al.
246 (2008).

247 The top of the pluton was emplaced at 6 km depth (Rocchi et al., 2010 Farina et al., 2010). The
248 initial system temperature as a function of depth is determined by linear geothermal gradients of
249 either 25°C/km (150°C at 6 km depth) or 40°C/km (240°C/km at 6 km depth). Early and distant
250 intrusions such as the Portoferraio and San Martino porphyries do not significantly affect crustal
251 temperature at the time of Mt. Capanne emplacement, supported by the lack of contact
252 metamorphism associated with those earlier sills.

253 Solving eq. 1 and calculating melt fraction with time requires knowledge of the temperature-
254 melt fraction relationship. We used the Rhyolite-MELTS phase equilibria package (Gualda et al.,
255 2012) with the chemical composition of the SA, SF and SP facies as inputs (see Supplementary
256 material for details on the MELTS model). Inaccuracies in Rhyolite-MELTS results have been
257 reported for felsic, hydrated melts (Gardner et al., 2014), and so we compared a series of
258 Rhyolite-MELTS outputs (by varying, e.g., pressure and water content) to petrological
259 observations, modal proportions and microprobe mineral measurements made on Mt. Capanne
260 granite thin sections (e.g., Barboni and Schoene, 2014). The runs that did not closely match
261 observed records were discarded. The remaining runs that were used in our numerical simulations
262 (Fig. 3) are in good agreement with experimental data acquired on similar granitic compositions
263 (Naney, 1983; Whitney, 1988).

264 According to Rocchi et al., (2010) and Barboni and Schoene, (2014), the magma was rich in
265 feldspar and quartz at the time of emplacement. The zircon saturation temperature was estimated
266 at about 805°C for all three Mt. Capanne facies at the emplacement level (see Supplementary

267 Material for details on the Zr saturation model). In a first series of simulations, we test the
268 hypothesis that the magma is emplaced above zircon saturation temperature and that zircons are
269 crystallised after emplacement. Accordingly, in those simulations the magma is emplaced with
270 20% crystals and emplacement temperatures of 878, 906, and 856 °C for SA, SF and SP
271 respectively (Fig.3). We determined the period τ during which zircon can crystallize by
272 calculating the time spent by the magma between the saturation temperature and the solidus (688,
273 676 and 666 °C for SA, SF and SP facies respectively). We infer from those simulations (c.f.
274 section 5.1 below) that zircon saturation preceded emplacement because the range of observed
275 zircon dates is far longer than the time that liquid is present as permitted by the numerical
276 models. In a second series of simulations, the magma is emplaced at 800°C with a crystal fraction
277 of 40%. In this case τ is the time spent by the magma above solidus.

278 The results are reported in Table 2 and 3 as τ_{sample} , which is τ at an estimated sample
279 paleodepth (Fig. 4b) and τ_{batch} , which is the maximum τ within a given batch, so that:

280 $\tau_{sample} = \tau(z = z_{sample})$ (2)

281 $\tau_{batch} = Max[\tau(z_u < z < z_l)]$ (3)

282 with z , the depth, z_{sample} the depth of a sample, z_u the depth of a batch upper boundary and z_l
283 the depth of a batch lower boundary.

284 Since cooling times are the longest close to the batch center, τ_{batch} is significantly longer than
285 τ_{sample} if a sample has been collected far away from the batch center. This is the case for SP (Fig.
286 4b).

287 We tested two scenarios for the construction of the Mt. Capanne pluton. In the first scenario,
288 (3-batch scenario) we followed Farina et al., (2010) in assuming that SA, SF, and SP facies each
289 correspond to a single magma batch that are respectively 250, 650 and 1500 m thick (Fig.4a,

290 Table 2) with emplacement times determined by samples MB11-6 (SA), MB12-4 (SF) and
291 MB11-2 (SP). In the second scenario, the magma emplacement sequence is determined by the
292 zircon dates from samples MB11-6, MB12-9, MB12-8, MB12-4, and MB11-2, such that each
293 sample is treated as an individual batch of magma (Fig.4b, Table 3). In other words, the second
294 scenario assumes multiple pulses per facies, each one of them represented by one of our samples.
295 The thicknesses of those pulses were approximated on the basis of the cross-section after
296 removing the deformation of successive pulses (unfolding the cross-section on Fig.1). We did not
297 include MB11-1 because in the unfolded intrusion it is located at the same vertical level than
298 MB11-2 and hence should belong to the same sill. In all cases, we used a diameter for the
299 intrusions of 9 km (Farina et al., 2010).

300

301 **6. Numerical simulation results**

302

303 *6.1 Testing the significance of zircon date spectra*

304

305 The numerical simulations were used to test the hypothesis that magma emplacement is
306 recorded by the oldest zircon ages from each pulse, outliers excluded (Table 1), and that the range
307 of zircon ages reflects in-situ crystallization. We decided to consider as outliers the grains that
308 were older than the main population by a large gap in dates (Fig.1; Table 1).

309 As a preliminary test, we emplaced the entire Mt. Cappane pluton instantly and observed
310 whether the cooling time between zircon saturation and solidus within the pluton matched the
311 zircon age spectra. In this scenario (using an intrusion temperature of 906 °C and composition
312 equivalent to the SF), the maximum predicted range in zircon dates is 78 ka and 52 ka for a
313 geotherm of 40 and 25 °C/km, respectively (Fig.5a). This is much shorter than the observed

314 zircon age range ($\Delta t=560\pm10$ ka for the all Mt. Capanne intrusion; Fig.1 and Table 1), and is thus
315 insufficient to explain the zircon dataset.

316 In the 3-batch scenario, the oldest zircon date of two samples within a facies was initially
317 taken as the emplacement age for the facies and emplacement is by underaccretion (Table 2).
318 By contrast, in the 5-batch scenario, successive batches are injected randomly within the intrusive
319 body rather than below, as dictated by the zircon dates (Fig.4a ; Table 3), and thus there is no
320 relationship between facies and timing. In this set of models, magmas were emplaced at low
321 crystallinity (20%) to test the duration of liquid residence from above zircon saturation to the
322 solidus. Table 2 and 3 reports τ_{batch} the longest magma residence time between zircon saturation
323 and solidus temperature for each of the 3 and 5 batches, respectively. For both scenarios, the
324 maximum zircon crystallization time predicted by our simulation is less than 60,000 years in the
325 SP facies (Table 3; Fig.5) and is much shorter than the range of observed zircon dates (minimum
326 0.3 Ma; Fig. 1) even when a steep 40°C/km geothermal gradient is considered. The modeled
327 maximum zircon crystallization time in Sant'Andrea facies is 750 years for a 3-batch scenario and
328 1100 years in a 5-batch scenario and incommensurate with the observed spread in SA zircon
329 dates ($\Delta t=331\pm8$ ka; Fig.1). This discrepancy between the model results and zircon dates suggests
330 that our working hypothesis – that the oldest zircon dates record emplacement and that the range
331 of dates records continuous in situ crystallization – is not correct. The alternate hypothesis, that
332 most of the zircons crystallized at depth and were recycled (antecrustic, using terminology of
333 Miller et al., 2007), is more accurate.

334

335 *6.2. Testing for the presence of melt between batches*

336

337 Farina et al. (2010) argue that retaining melts between the three injections is necessary in order
338 to erase contacts between the sheets. We tested their hypothesis in the light of our new temporal
339 constraints. Based on the result described above, we now test the other end-member assumption
340 that magma is emplaced at or below zircon saturation temperature (Figs. 6 and 7) and that the
341 youngest zircon date from each facies or sample corresponds to the pulse emplacement time
342 (Table 2 and 3). This results in emplacement by underaccretion for both construction scenarios.
343 In these sets of models, magmas were emplaced at high crystallinity (40%) to be in line with the
344 Zr-saturation temperature (ca. 805°C; Supplement Material) The simulations unequivocally show
345 that for both the 3- and 5-batch scenarios, no melt remains in the system between the successive
346 batches even with a high initial geotherm of 40 °C/km (Table 2 and 3; Fig. 6 and 7). The
347 maximum volumes of melts present in the system do not exceed the volume of the last pulse
348 (Fig.6A and 7), which indicates that remelting of former pulse is absent or very limited. For the
349 3-batch model, the geotherm is only slightly perturbed at the time of emplacement of San
350 Francesco and San Piero (Fig.6B and 6B). Our simulations also show that increasing the number
351 of batches (while still respecting the final volume and duration of intrusion of the Mt. Capanne
352 pluton) would only give shorter liquid residence time, and would not satisfy the hypothesis of
353 residual melt persistence. We concur with Farina et al. (2010) that fast emplacement of Mt.
354 Capanne over less than 10,000 year is necessary for maintaining melt between pulses but our
355 zircon ages indicate much longer emplacement timescale. Therefore, the integration of thermal
356 models and zircon ages does not support the hypothesis that the absence of mappable contacts
357 between facies in the pluton is due to the presence of melt between pulses.

358

359 *6.3. The size of magma reservoirs*

360

361 Both for the 3-pulse and 5-pulse scenarios each pulse completely solidifies before the next one
362 so that the maximum volume of melt corresponds to the volume of individual pulses. According
363 to our geochronologic data, and assuming that the youngest zircon has been sampled and dates
364 emplacement, the minimum number of pulses is 4. The youngest dates of MB12-4 and MB12-8
365 overlap and those two samples may belong to the same pulse. The largest possible pulse has the
366 inferred thickness (1.5 km) and diameter (8 km) of the San Piero facies, which corresponds to a
367 volume of about 75 km³. However, pulses may have been much more numerous, in which case
368 any magma reservoir would have been of smaller volume.

369

370 **7. Discussion**

371

372 *7.1 Constraints on pluton assembly provided by combined zircon geochronology and thermal*
373 *modeling*

374

375 7.1.1 Zircon sources and crystallization histories

376

377 The ID-TIMS U-Pb geochronology presented here illustrates that temporal resolution of tens
378 of thousands of years is necessary to resolve the intrusion history of the Mt. Capanne pluton.
379 Previous U-Pb data obtained by SIMS (Gagnevin et al., 2011) was consistent with a rapid
380 emplacement of the pluton, but due to inherently larger uncertainties associated with that method
381 ($\geq \pm 150$ ka in Gagnevin et al., 2011) were unable to differentiate between the ages of different
382 magma pulses and therefore could not test the top-down laccolith emplacement model (Farina et
383 al., 2010). The drawback of ID-TIMS geochronology is the larger volume of zircon analyzed,
384 which can integrate protracted zircon growth histories into a single precise crystallization date.

385 We show in this study that careful CL-imaging followed by microsampling can avoid analysis of
386 complexities such as inherited cores (Fig.2; Supplementary Figure 2) in an effort to date the
387 youngest zone of a zircon. However, we observe that removing and selectively analyzing zircon
388 tips does not necessarily yield the youngest dates within a sample (Fig. 2; Supplementary Figure
389 2), suggesting that complexities in zircon saturation and nucleation at small spatial scales and/or
390 grain armoring affects the zircon growth record.

391 Experimental data for zircon saturation show that granodioritic to granitic melts reach zircon
392 saturation at temperatures well above the solidus and therefore could carry significant amounts of
393 early-crystallized zircon during remobilization and transport of magma (Watson and Harrison,
394 1983; Boehnke et al., 2013; Harrison et al., 2007; Miller et al., 2007). As a consequence, the
395 physical integrity and also age information in zircon can survive transport, reheating, and
396 reincorporation in subsequent batches of magma, and interpreting zircon dates in terms of
397 magmatic processes is difficult (Lissenberg et al., 2009; Miller et al., 2007; Schoene et al., 2012).
398 One approach to this problem is to target zircon populations included within specific phases
399 versus the bulk rock, and combine those data with petrologic observations and zircon saturation
400 and phase equilibria modeling to estimate the solidification age of certain pulses (see Barboni and
401 Schoene, 2014, for an example using the SA). Building on that approach for the entire pluton, we
402 estimated zircon saturation temperatures for our samples by modeling the Zr and bulk
403 composition evolution of the melt given by our Rhyolite-MELTS results (see Supplement for
404 detailed methodology and figures) and using the zircon saturation models of Boehnke et al.,
405 (2013). Our results suggest that saturation was reached in the Mt. Capanne magmas at
406 temperatures of ca. 805°C, well above the modeled solidi of 688-666 °C. Textures revealed by
407 CL imaging (Fig. 2) also record resorption events within the Mt. Capanne zircons (see also
408 Gagnevin et al., 2011), suggesting that zircon saturation was not constant over the time span of

409 200 to 400 ka recorded by zircon in our samples. This conclusion is supported by the results of
410 Barboni and Schoene, (2014), who show that at least 100 ka of zircon crystallization is recorded
411 in the SA prior to its emplacement, in that zircon dates from that pulse predate the intrusion of the
412 demonstrably cross-cut San Martino porphyry by ca. 100 ka.

413 Our thermal modeling and geochronology combine these data to test whether the observed range
414 of zircon dates (~300 ka) from each sample could represent post-emplacement cooling. Because
415 the maximum melt residence time determined in our models is ~58 ka for any batch of magma, it
416 is unavoidable that at least ca. 200 ka of pre-intrusion zircon crystallization (i.e. zircons carried
417 from depth) occurred and is recorded within the Mt Capanne pluton. Our results therefore limit
418 the duration of a magma reservoir in the shallow Elba magmatic system and suggest that most of
419 the zircons were recycled from a deeper crustal reservoir.

420

421 7.1.2 Construction of Mt. Capanne pluton

422

423 Farina et al., (2010) hypothesized that the SA, SF and SP facies correspond to distinct magma
424 batches injected in the upper crust and contacts between them are absent because melt was
425 preserved between magma pulses, which required pluton emplacement in less than 10 ka.
426 However, the difference between the youngest zircons dated in this study from the SA (MB11-6)
427 and the SP (MB11-2) exceeds 300 ka. A possibility is that the pluton was emplaced rapidly ca.
428 7.3 Ma (the youngest SA zircon) and that older SA zircons were inherited from deeper in the
429 crust whereas SP zircons <7.3 Ma crystallized in situ post emplacement. We tested this
430 hypothesis but found that the crystallization time of the SP in such a model is limited to 58 ka,
431 requiring the SP to intrude at least 240 ka after the SA, containing a substantial amount of
432 inherited zircon (Fig. 5 and 6). For this reason, our zircon U-Pb data and thermal modeling show

433 that the conclusion of Farina et al. (2010), that the Mt. Capanne pluton must have been emplaced
434 in <10 ka, is incorrect; this incorrect assertion stems from the assumption that melt was present
435 between pulses, explored below.

436 Our thermal modeling results therefore argue that the timing of magma emplacement for a given
437 pulse (as represented by a handsample) is closer to the youngest zircon date, and that the intrusion
438 time is constrained by the youngest zircon date and the limits of the thermal model. Though the
439 exact number of pulses is not determined by our data, we can reach several important conclusions
440 and highlight remaining uncertainties. The SA was constructed by under-accretion of at least two
441 different pulses 150 vertical meters apart represented by samples MB11-6 and MB12-9 (Fig.4b).
442 Our two samples from the SF, MB12-4 and MB12-8, have youngest zircons that are nearly
443 indistinguishable though MB12-4 was structurally 100 m higher than MB12-8. The large gap in
444 dates between the youngest and the second youngest zircon in MB12-4 imposes significant
445 uncertainty on whether the youngest zircon is in fact representative of the magma solidus.
446 Therefore any conclusion as to whether the SF intruded as one or more than one pulse based on
447 zircon dates is speculative. Similarly, zircon dates from the SP samples are very similar and the
448 youngest dates overlap within uncertainty. However, the SP outcrops sampled were emplaced at a
449 similar structural level, and may represent only one of potentially many sills. Therefore, while
450 collecting more samples within the Mt. Capanne cross-section would allow better estimation of
451 the number of pulses, our main conclusions would not likely change. These are that our zircon
452 data coupled with thermal modeling require that the Mt. Capanne pluton intruded in at least 4
453 pulses (potentially many more) over ~ 250 ka and that the maximum liquid residence time is ~60
454 ka. Our data support previous models for pluton assembly by underaccretion (Farina et al., 2010),
455 similar to some other recently studied intrusions (de Saint-Bланquat et al., 2006; Michel et al.,
456 2008; Barboni et al., 2013).

457

458 *7.2 Effect of unknown pluton geometry on the numerical simulation results*

459

460 Increasing the volume of magma underplated beneath the exposed pluton (i.e. increasing the
461 thickness of the San Piero facies) could effect the melt residence time in the deepest part of the
462 intrusion. In this case, the outcropping part of the Mt. Capanne would represent only the roof of a
463 larger magmatic system extending at depth. This possibility is in contradiction with Dini et al.
464 (2008), who used a detailed magnetic susceptibility survey of the Mt. Capanne pluton to resolve
465 the laccolith pluton shape with a maximum thickness of ca. 2.5 km (thickness used in our
466 simulation), but we consider the possibility nonetheless. Our geochronologic data for the SA
467 facies requires solidification prior to the intrusion of the SF and SP facies, consistent with the
468 results from Barboni and Schoene (2014), and without subsequent remobilization. An early SA
469 crystallization is also suggested by our Orano Dyke zircon dates, which are younger than those
470 from the SA facies it crosscuts (Supplement Fig.1), but much older than the youngest San Piero
471 zircon (7.080 ± 0.005 Ma for Orano versus 7.007 ± 0.007 Ma for SP; Fig.1). If the San Piero facies
472 was much thicker than predicted by Dini et al., (2008), its thermal effect did not significantly
473 reheat the upper part of the intrusion.

474 Another unknown that could affect our numerical results is the possibility that part of the
475 intrusion roof (represented in our case by the SA facies) was eroded away. Our models show that
476 the maximum melt residence time for the SA facies is ca. 1 ka, which is much shorter than the
477 prediction from Barboni and Schoene (2014) based on the information recorded by the SA K-
478 feldspar megacrysts (10-40 ka). This suggests a SA facies thicker than observed today, which
479 potentially biases our thermal model outputs by underestimating the original volume of the pulse.

480

481 7.3 *Absence of internal contacts within the Mt. Capanne pluton*

482

483 Integrating age data with numerical modeling shows that for the simulations we ran, melt was
484 not preserved between magma batches and therefore the absence of internal contacts within the
485 Mt. Capanne intrusion is not related to the presence of residual melt. Alternative hypotheses that
486 could explain the lack of internal contacts within an incrementally built granitic pluton include
487 (1) remelting of previously emplaced pulses by a new injection that obscures contacts (Bartley,
488 2008), and (2) sustained amphibolite facies conditions triggering subsolidus textural change and
489 erasing contacts (e.g. Hanson and Glazner, 1995). Farina et al. (2010) discarded the latter
490 hypothesis based on lack of contact metamorphism in the Mt. Capanne host rock and absence of
491 macro- or microscopic recrystallization evidence in the Mt. Capanne granite. The results of
492 Barboni and Schoene (2014), which show core-to-rim younging in zircon included within
493 megacrystic K-feldspar, require rapid cooling and solidification of early pulses without
494 substantial textural modification. Numerical models also predict only slightly perturbed
495 geotherms by successive injections at the depth and of the size of the Mt. Capanne pluton.
496 Another hypothesis for obscuring internal contacts is that (3) contacts between magma of similar
497 composition and texture, as is the case in the Mt. Capanne intrusion, could be difficult to identify
498 in the field if there is no major changes in mineralogy, mineral modal proportions or mineral size.
499 Chilled margins (i.e. reduction of the mineral size approaching the contact with the cold facies)
500 are usually the best way to identify contacts between various injections. However, if the
501 temperature gradient between the new injection and the already solidified pulse is not large
502 enough (as is usually the case for intermediate to felsic melts), then chilled margins may not be
503 expected. While our thermal models preclude large scale reheating or remelting of previous
504 sheets, heating and or physical abrasion (plucking, remobilization) of contacts at a centimeter to

505 meter scale are possible and would act to obscure pulse contacts. Though our geochronological
506 data were able to identify at least 4 pulses, it is possible that the Mt. Capanne pluton is composed
507 of many more sheets with gradational composition whose contacts could be obscured by these
508 processes. Other field examples where 100 m to km scale 3D cross-sections are visible show that
509 it is possible to identify subtle contacts within similar composition sheets (e.g. Torres de Paines
510 laccoliths; Michel et al., 2008; Himalayan leucogranites; Searle et al., 2010), but such
511 relationships are elusive at the outcrop level (Bartley, 2008). We suspect the Mt. Capanne pluton
512 is one of these cases where the compositions and textures of the different increments are too
513 similar to generate obvious contacts in the field.

514

515 *7.4 Eruptible volumes for the upper-crustal Mt. Capanne reservoir and implication for modern*
516 *arc volcanism.*

517

518 A difficulty in understanding active volcanic systems is that very little information is available
519 about the longevity and size of subvolcanic reservoirs. “Fossilized” reservoirs such as the Mt.
520 Capanne pluton can be used to constrain emplacement rates and reservoir lifespan, and contrast
521 volcanic and plutonic records. Calc-alkaline magmatism in Elba occurred in a similar tectonic
522 context as modern arc systems (Rosenbaum and Lister, 2004; Gasparon et al., 2009). Our thermal
523 models show that small upper-crustal systems such as the Mt. Capanne pluton do not contain
524 magma chambers on timescales of hundreds of ka, regardless of the intrusion mechanism. For the
525 scenarios modeled, each pulse injected in the Mt. Capanne system solidifies before the next one
526 intrudes, and therefore the maximum eruptible volume for the system is the volume of each
527 injection. Those volumes range from 2 to 60 km³, depending upon the crystallinity of the magma
528 at time of melt extraction and eruption (eruption between 40% and 60% crystals; e.g. Bachmann,

529 2004) and are similar to those observed in recent arc eruptions (Mt. Pinatubo 1991, 8-10 km³,
530 Wolf et Hoblitt, 1996; Mt. Saint Helens 1980, 1.25 km³, Tilling, 1984). If magma was indeed
531 emplaced at about 40% crystals, then our results show that melt remained eruptible for only a
532 very short period of time (<50 ka, but for most pulses in less than several ka), which is in line
533 with the conclusions of Barboni and Schoene (2014) and Cooper and Kent (2014). Volatiles
534 would also have a strong effect on the eruptibility of the system but their nature and role are
535 unfortunately currently poorly understood in Elba.

536

537 **8. Conclusions**

538

539 Our study on the Mt. Capanne intrusion from Elba island shows that coupling a large dataset of
540 high-precision ages with thermal modeling can help assess the emplacement history and thermal
541 evolution of incrementally built upper-crustal reservoirs. Our results suggest that the Mt. Capanne
542 intrusion was built in minimum 250,000 years by multiple magma increments in the crust.
543 Numerical models of sill accretion constrained by U-Pb ID-TIMS dates indicate that no melt was
544 preserved between individual injections. The thermal contribution of each pulse is not large
545 enough to generate long-lasting magma reservoirs and the maximum volumes that can be erupted
546 correspond to the volume of each pulse injected. These results provide interesting insight into
547 understanding active volcanism in modern arcs. Elba magmatism was very similar, both in
548 tectonic context and magma volumes, to some modern arc volcanoes (e.g. Mt. St. Helen; Mt.
549 Pinatubo) and would have produced similar eruptible volumes (< 10 km³). While active magma
550 chambers can only be assessed indirectly, information recorded in a “fossilized” reservoir such as
551 the Mt. Capanne can give insight into time-integrated rates of magma recharge and duration of
552 potential eruption windows in active system.

553 We also show that absence of contacts within intermediate to granitic intrusions does not
554 require melt preservation in the contact zones between magma sheets, as was previously proposed
555 by Farina et al. (2010) for the Mt. Capanne intrusion. Our thermal models unambiguously
556 indicate that every new magma increment will have a very short liquid residence time in the
557 upper crust, with no melt remaining in-between pulses. Contacts between sheets of similar texture
558 and composition might be unidentifiable at the outcrop scale, as suggested by Bartley et al.,
559 (2008). In such cases, the use of high-precision dating on zircon can discriminate between
560 different magma injections (Schoene et al., 2012).

561 Complexities in U-Pb age populations resulting from zircon recycling introduce complexities
562 in resolving incremental emplacement in evolved melts. However, coupling zircon ages with
563 thermal modeling aids interpretation of complex age spectrums and identifying zircon inherited
564 from deeper crustal levels. Our results suggest that for the Mt. Capanne pluton, the majority of
565 the zircon record is inherited from a deeper level of the system and that only a small portion of
566 the ages record in-situ crystallization.

567

568 **Acknowledgements**

569 Funding for this project was provided by the Swiss National Science Foundation (fellowship
570 PBLAP2-134389 to Barboni) and Princeton University. We thank F. Bussy for assistance in the
571 field and use of thin sections. Three anonymous reviewers provided very useful reviews that
572 greatly improved an early version of this manuscript.

573

574 **References Cited**

575

576 Annen, C., 2009. From plutons to magma chambers: Thermal constraints on the accumulation of

- 577 eruptible silicic magma in the upper crust. *Earth and Planetary Science Letters* 284, 409–416.
- 578 Annen, C., Pichavant, M., Bachmann, O., Burgisser, A. 2008. Conditions for the growth of a
579 long-lived shallow crustal magma chamber below Mount Pelee volcano (Martinique, Lesser
580 Antilles Arc). *Journal of Geophysical Research* 113, B07209.
- 581 Bachmann, O. 2004. On the Origin of Crystal-poor Rhyolites: Extracted from Batholithic Crystal
582 Mushes. *Journal of Petrology* 45, 1565–1582.
- 583 Bachmann, O., Bergantz, G.W. 2008. Deciphering Magma Chamber Dynamics from Styles of
584 Compositional Zoning in Large Silicic Ash Flow Sheets. *Reviews in Mineralogy and*
585 *Geochemistry* 69, 651–674.
- 586 Bachmann, O., Miller, C., de Silva, S. 2007. The volcanic–plutonic connection as a stage for
587 understanding crustal magmatism. *Journal of Volcanology and Geothermal Research* 167, 1–
588 23.
- 589 Barboni, M., Schoene, B. 2014. Short eruption window revealed by absolute crystal growth rates
590 in a granitic magma. *Nature Geoscience* 7, 524–528.
- 591 Barboni, M., Schoene, B., Ovtcharova, M., Bussy, F., Schaltegger, U., Gerdes, A. 2013. Timing
592 of incremental pluton construction and magmatic activity in a back-arc setting revealed by
593 ID-TIMS U/Pb and Hf isotopes on complex zircon grains. *Chemical Geology* 342, 76-93.
- 594 Bartley, J. M., Coleman, D.S., Glazner, A.F. 2008, Incremental pluton emplacement by magmatic
595 crack-seal. *Trans. Royal Soc. Edinburgh: Earth Sci.* 97, 383-396.
- 596 Boehnke, P., Watson, E.B., Trail, D., Harrison, T.M., Schmitt, A.K. 2013. Zircon saturation re-
597 visited. *Chemical Geology* 351, p. 324-334.
- 598 Bussy, F. 1991. Pétrogenèse des enclaves microgrenues associées aux granitoïdes calco-alcalins :
599 exemple des massifs varisque du Mont-Blanc (Alpes occidentales) et Miocène du Monte
600 Capanne (Ile d'Elbe, Italie). *Mémoire de Géologie Lausanne* 7, 309 pp.

- 601 Caricchi, L., Simpson, G., Schaltegger, U. 2014. Zircons reveal magmatic fluxes in the Earth's
602 crust. *Nature* 511, 457-461.
- 603 Clemens, J.D., Mawer, C.K. 1992. Granitic magma transport by fracture propagation.
604 *Tectonophysics* 204, 339-360.
- 605 Coleman, D.S., Gray, W., Glazner, A.F. 2004. Rethinking the emplacement and evolution of
606 zoned plutons: Geochronologic evidence for incremental assembly of the Tuolumne Intrusive
607 Suite, California. *Geology* 32, 433-436.
- 608 Cooper, K.M., Kent, A.J. 2014. Rapid remobilization of magmatic crystals kept in cold storage.
609 *Nature* 506, 480-483.
- 610 de Saint Blanquat, M., Horsman, E., Habert, G., Morgan, S., Vanderhaeghe, O., Law, R., Tikoff,
611 B. 2010. *Tectonophysics* 500, 20–33.
- 612 de Saint-Bланquat, M., Habert, G., Horsman, E., Morgan, S., Tikoff, B., Launeau, P., Gleizes, G.
613 2006. Mechanisms and duration of non-tectonically assisted magma emplacement in the
614 upper crust: The Black Mesa pluton, Henry Mountains, Utah. *Tectonophysics* 428, 1–31.
- 615 de Silva, S.L., Gosnold, W.D. 2007. Episodic construction of batholiths: Insights from the
616 spatiotemporal development of an ignimbrite flare-up. *Journal of Volcanology and*
617 *Geothermal Research* 167, 320–335.
- 618 Deering, C.D., Bachmann, O., Dufek, J., Gravley, D.M. 2011. Rift-Related Transition from
619 Andesite to Rhyolite Volcanism in the Taupo Volcanic Zone (New Zealand) Controlled by
620 Crystal-melt Dynamics in Mush Zones with Variable Mineral Assemblages. *Journal of*
621 *Petrology* 52, 2243–2263.
- 622 Dini, A., Innocenti, F., Rocchi, S., Tonarini, S., Westerman, D. 2002. The magmatic evolution of
623 the late Miocene laccolith-pluton-dyke granitic complex of Elba Island, Italy. *Geological*
624 *Magazine* 139, 257-279.

- 625 Dini, A., Rocchi, S., Westerman, D. 2004. Reaction microtextures of REE–Y–Th–U accessory
626 minerals in the Monte Capanne pluton (Elba Island, Italy): a possible indicator of
627 hybridization processes. *Lithos* 78, 101–118.
- 628 Dini, A., Westerman, D.S., Innocenti, F., Rocchi, S. 2008. Magma emplacement in a transfer
629 zone: the Miocene mafic Orano dyke swarm of Elba Island, Tuscany, Italy. *Geological
630 Society London Special Publications* 302, 131–148.
- 631 Farina, F., Dini, A., Innocenti, F., Rocchi, S., Westerman, D.S. 2010. Rapid incremental
632 assembly of the Monte Capanne pluton (Elba Island, Tuscany) by downward stacking of
633 magma sheets. *Geological Society of America Bulletin* 122, 1463–1479.
- 634 Farina, F., Stevens, G., Dini, A., Rocchi, S. 2012. Peritectic phase entrainment and magma
635 mixing in the late Miocene Elba Island laccolith–pluton–dyke complex (Italy). *Lithos* 153,
636 243–260.
- 637 Gagnevin, D., Daly, J., Poli, G. 2004. Petrographic, geochemical and isotopic constraints on
638 magma dynamics and mixing in the Miocene Monte Capanne monzogranite (Elba Island,
639 Italy). *Lithos* 78, 157–195.
- 640 Gagnevin, D., Daly, J., Waught, T., Morgan, D., Poli, G. 2005. Pb isotopic zoning of K-feldspar
641 megacrysts determined by laser ablation multi-collector ICP-MS: Insights into granite
642 petrogenesis. *Geochimica et Cosmochimica Acta* 69, 1899–1915.
- 643 Gagnevin, D., Daly, J.S., Horstwood, M.S.A., Whitehouse, M.J. 2011. In-situ zircon U–Pb,
644 oxygen and hafnium isotopic evidence for magma mixing and mantle metasomatism in the
645 Tuscan Magmatic Province, Italy. *Earth and Planetary Science Letters* 305, 45–56.
- 646 Gagnevin, D., Daly, J.S., Poli, G. 2008. Insights into granite petrogenesis from quantitative
647 assessment of the field distribution of enclaves, xenoliths and K-feldspar megacrysts in the
648 Monte Capanne pluton, Italy. *Mineralogical Magazine* 72, 925–940.

- 649 Gardner, J.E., Befus, K.S., Gualda, G.A.R., Ghiorso, M.S. 2014. Experimental constraints on
650 rhyolite-MELTS and the Late Bishop Tuff magma body. Contributions to Mineralogy and
651 Petrology 168, 1051–14.
- 652 Gasparon, M., Rosenbaum, G., Wijbrans, J., Manetti, P. 2009. The transition from subduction arc
653 to slab tearing: Evidence from Capraia Island, northern Tyrrhenian Sea. Journal of
654 Geodynamics 47, 30–38.
- 655 Gelman, S. E., Gutiérrez, F. J., & Bachmann, O., 2013. On the longevity of large upper crustal
656 silicic magma reservoirs. Geology 41, 759-762.
- 657 Glazner, A., Bartley, J., Coleman, D., Gray, W., Taylor, R. 2004. Are plutons assembled over
658 millions of years by amalgamation from small magma chambers? GSA Today 14, 4-11.
- 659 Gualda, G.A.R., Ghiorso, M.S., Lemons, R.V., Carley, T.L. 2012. Rhyolite-MELTS: a Modified
660 Calibration of MELTS Optimized for Silica-rich, Fluid-bearing Magmatic Systems. Journal
661 of Petrology 53, 875–890.
- 662 Hale, A.J., Wadge, G., Mühlhaus, H.B. 2007. The influence of viscous and latent heating on
663 crystal-rich magma flow in a conduit. Geophysical Journal International 171, 1406–1429.
- 664 Hanson, R.B., Glazner, A.F. 1995. Thermal requirements for extensional emplacement. Geology
665 23, 213–216.
- 666 Harrison, T.M., Watson, E.B., Aikman, A.B. 2007. Temperature spectra of zircon crystallization
667 in plutonic rocks. Geology 35, 635-638.
- 668 Lipman, P.W. 2007. Incremental assembly and prolonged consolidation of Cordilleran magma
669 chambers: Evidence from the Southern Rocky Mountain volcanic field. Geosphere 3, 42-70.
- 670 Lissenberg, C.J., Rioux, M., Shimizu, N., Bowring, S.A., Mével, C. 2009. Zircon Dating of
671 Oceanic Crustal Accretion. Science 323, 1048–1050.
- 672 Malinverno, A., Ryan, W.B.F. 1986. Extension in the Tyrrhenian Sea and shortening in the

- 673 Apennines as results of arc migration driven by sinking of the lithosphere. *Tectonics* 5, 227–
674 245.
- 675 Menand, T. 2011. Physical controls and depth of emplacement of igneous bodies: A review.
676 *Tectonophysics* 500, 11–19.
- 677 Menand, T., Annen, C., de Saint-Blanquat, M. 2015. Rates of magma transfer in the crust:
678 Insights into magma reservoir recharge and pluton growth. *Geology* 43, 199–202.
- 679 Michel, J., Baumgartner, L., Putlitz, B., Schaltegger, U., Ovtcharova, M. 2008. Incremental
680 growth of the Patagonian Torres del Paine laccolith over 90 k.y. *Geology* 36, 459–462.
- 681 Miller, C., Miller, J. 2002. Contrasting stratified plutons exposed in tilt blocks, Eldorado
682 Mountains, Colorado River Rift, NV, USA. *Lithos* 61, 209–224.
- 683 Miller, C.F., Furbish, D.J., Walker, B.A., Claiborne, L.L., Koteas, G.C., Bleick, H.A., Miller, J.S.
684 2011. Growth of plutons by incremental emplacement of sheets in crystal-rich host: Evidence
685 from Miocene intrusions of the Colorado River region, Nevada, USA. *Tectonophysics* 500,
686 65–77.
- 687 Miller, J., Matzel, J., Miller, C., Burgess, S., Miller, R. 2007. Zircon growth and recycling during
688 the assembly of large, composite arc plutons. *Journal of Volcanology and Geothermal
689 Research* 167, 282–299.
- 690 Naney, M.T. 1983. Phase equilibria of rock-forming ferromagnesian silicates in granitic systems.
691 *American Journal of Science* 283, 993–1033.
- 692 Robertson, E.C. 1988. Thermal properties of rocks. U.S. Geological Survey Open File Report 88–
693 441, 106 pp.
- 694 Rocchi, S., Westerman, D.S., Dini, A., Farina, F. 2010. Intrusive sheets and sheeted intrusions at
695 Elba Island, Italy. *Geosphere* 6, 225–236.
- 696 Rosenbaum, G., Lister, G.S. 2004. Neogene and Quaternary rollback evolution of the Tyrrhenian

- 697 Sea, the Apennines, and the Sicilian Maghrebides. *Tectonics* 23, TC1013.
- 698 Schmitt, A.K., Danišík, M., Evans, N.J., Siebel, W., Kiemele, E., Aydin, F., Harvey, J.C. 2011.
- 699 Acigöl rhyolite field, Central Anatolia (part 1): high-resolution dating of eruption episodes
- 700 and zircon growth rates. *Contributions to Mineralogy and Petrology* 162, 1215–1231.
- 701 Schoene, B., Schaltegger, U., Brack, P., Latkoczy, C., Stracke, A., Günther, D. 2012. Rates of
- 702 magma differentiation and emplacement in a ballooning pluton recorded by U–Pb TIMS-
- 703 TEA, Adamello batholith, Italy. *Earth and Planetary Science Letters* 355-356, 162–173.
- 704 Schöpa, A., Annen, C. 2013. The effects of magma flux variations on the formation and lifetime
- 705 of large silicic magma chambers. *J. Geophys. Res. Solid Earth* 118, 926–942.
- 706 Searle, M.P., Cottle, J.M., Streule, M.J. and Waters, D.J. 2010. Crustal melt granites and
- 707 migmatites along the Himalaya: melt source, segregation, transport and granite emplacement
- 708 mechanisms. *Geological Society of America Special Papers* 472, 219-233.
- 709 Tilling, R.I. 1984. Eruptions of the Mount St. Helens : Past, present, and future. U.S. Geological
- 710 Survey, 46 pp.
- 711 Watson, E.B., Harrison, T.M. 1983. Zircon saturation revisited' temperature and composition
- 712 effects in a variety of crustal magma types, *Earth and Planetary Science Letters* 64, 295–304.
- 713 Wendt, I., Carl, C. 1991. The statistical distribution of the mean squared weighted deviation.
- 714 *Chemical Geology* 86, 275–285.
- 715 Westerman, D.S., Dini, A., Innocenti, F., Rocchi, S. 2004. Rise and fall of a nested Christmas-
- 716 tree laccolith complex, Elba Island, Italy. *Geological Society London Special Publications*
- 717 234, 195–213.
- 718 Westerman, D.S., Rocchi, S., Dini, A., Farina, F. 2015. Rise and Fall of a Multi-sheet Intrusive
- 719 Complex, Elba Island, Italy. *in* Breitkreuz, C. and Rocchi, S. (eds.), *Physical Geology of*
- 720 *Shallow Magmatic Systems: Advances in Volcanology*, Springer

- 721 Whitney, J.A. 1988. The origin of granite: The role and source of water in the evolution of
722 granitic magmas. Geological Society of America Bulletin 100, 1886–1897.
- 723 Whittington, A.G., Hofmeister, A.M., Nabelek, P.I. 2009. Temperature-dependent thermal
724 diffusivity of the Earth's crust and implications for magmatism. Nature 458, 319–321.
- 725 Wolfe, E.W., Hoblitt R.P. 1996, in *Fire and Mud: Eruptions and Lahars of Mount Pinatubo,*
726 *Philippines*, eds Newhall, C.G. & Punongbayan, R.S. Philippine Inst. Volcanol. &
727 Seismol./Univ. Washington Press, Quezon City/Seattle, 751–766.
- 728
- 729
- 730
- 731

731

732 **Figure captions**

733

734 Figure 1. Study area and ID-TIMS U-Pb geochronology. A) Geological map of Elba with sample
735 locations and cross-section of the Mt. Capanne pluton (modified after Westerman et al., 2004 and
736 Farina et al., 2010). Numbers I-V refer to tectonic complexes (as described in Westerman et al.,
737 2004). B) Rank-order plot of $^{206}\text{Pb}/^{238}\text{U}$ zircon dates from the Elba intrusives (with youngest
738 zircon age indicated for each samples with 2-sigma uncertainties). Individual bars correspond to
739 single zircons or zircon fragments with height of bars representing 2-sigma uncertainties. See
740 Table S1 for full U-Pb data table.

741

742 Figure 2. Cathodoluminescence images of selected zircons from the Elba intrusive rocks, with
743 ID-TIMS $^{206}\text{Pb}/^{238}\text{U}$ dates and 2-sigma uncertainties. Sample name and facies labeled in each
744 panel. White dashed line indicates where grains were fractured and solid line points to which
745 fragment was analyzed. See Table S1 for full U-Pb data table.

746

747 Figure 3. Melt fraction and proportion of crystallizing phases versus temperature used in the
748 numerical simulations for the three Mt. Capanne facies, as predicted by Rhyolite-MELTS. The
749 modal mineralogy observed in thin section is plotted on the left (colour boxes); colour curves
750 represent modal proportions predicted by MELTS. The zircon saturation temperatures were
751 determined for the evolving melt composition using MELTS and mineral-melt Zr partitioning
752 (Supplementary Methods).

753

754

755 Figure 4. Setup for the numerical simulation for the 3-pulse (A) and 5-pulse (B) scenario.
756 Successive magma pulses have the geometry of sills. The colors represent the different facies
757 (Fig. 1), whose thicknesses are determined by field relations; see text. The stars show the
758 approximate position of the U-Pb geochronology samples.

759

760 Figure 5. Numerical thermal model results for simulations where the oldest zircon dates
761 approximate intrusion of magma pulse for the 1-pulse (A), 3-pulse (B) and 5-pulse (C) scenarios.
762 Here magma emplacement temperature is above zircon saturation temperature (see text). The
763 colours and contour lines show the Log10 of the time (i.e., 4 = 10,000 years) spent by the magma
764 between zircon saturation (~805 °C) and the solidus on a cross section through the intrusion.
765 Initial geothermal gradient is 40 °C/km.

766

767 Figure 6. Numerical thermal model results for simulations where the youngest zircon dates
768 approximate intrusion of magma pulse for the 3-pulses scenario. Magma emplacement
769 temperature is below zircon saturation temperature at ~40% crystals. (A) Volumes of melt over
770 time. The spikes correspond to intrusion of SF and SP. SA is intruded at time 0 and the magma is
771 too short-lived to be visible on the diagram. (B) and (C) Snapshot of temperatures on a cross
772 section of the system at time 70,300 years (B) and 229,500 years (C) just before the emplacement
773 of SF (B) and SP (C). Curves are labelled in °C. The dashed line show the contour of already
774 emplaced pulses and the arrows show the level of the next pulse. In both cases, temperatures at
775 the time and depth of the new pulse are several hundred degrees below the wet granite solidus
776 (Withney, 1988) and no melt remains in the system between pulses. Initial geothermal gradient is
777 40 °C/km.

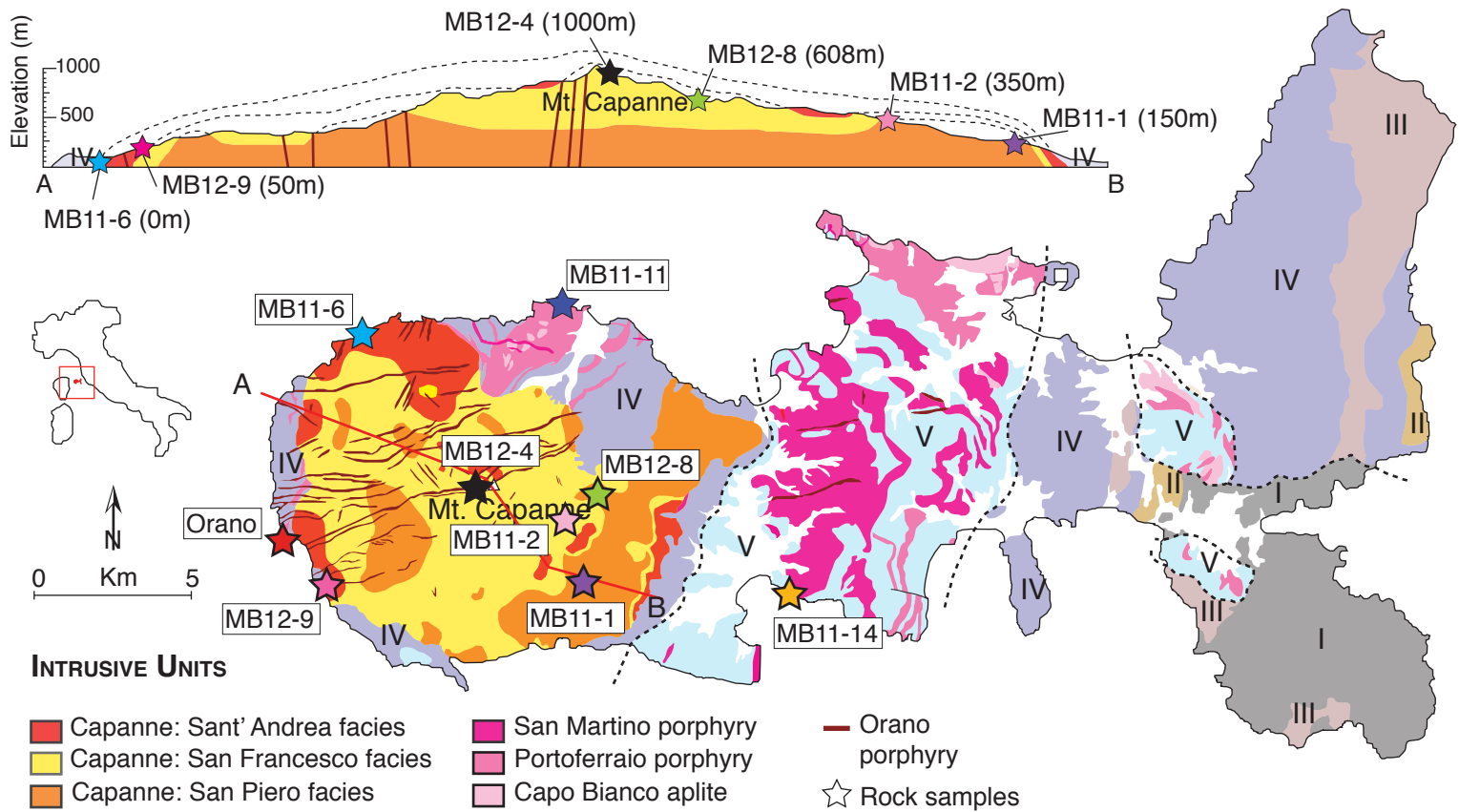
778

779

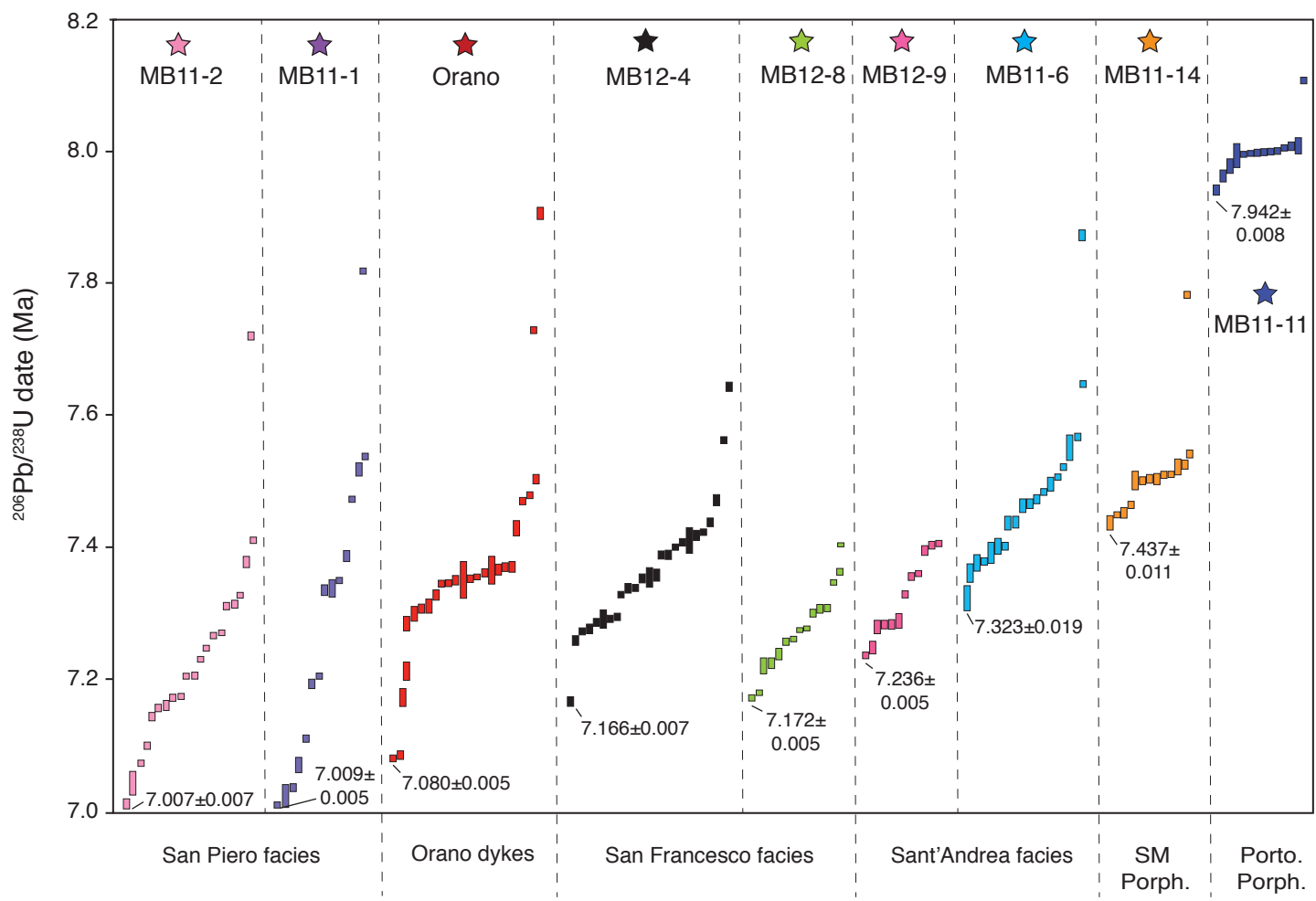
780 Figure 7. Numerical thermal model results for simulations where the youngest zircon dates
781 approximate intrusion of magma pulse for the 5-pulses scenario. Curves showing volume of
782 magma with >50% and >0% melt in the entire modelled magmatic systems are shown as a
783 function of time. Each spike corresponds to a pulse but the first pulse emplaced at time 0 is not
784 visible because it is too short-lived. No melt is retained between pulses. Initial geothermal
785 gradient is 40 °C/km.

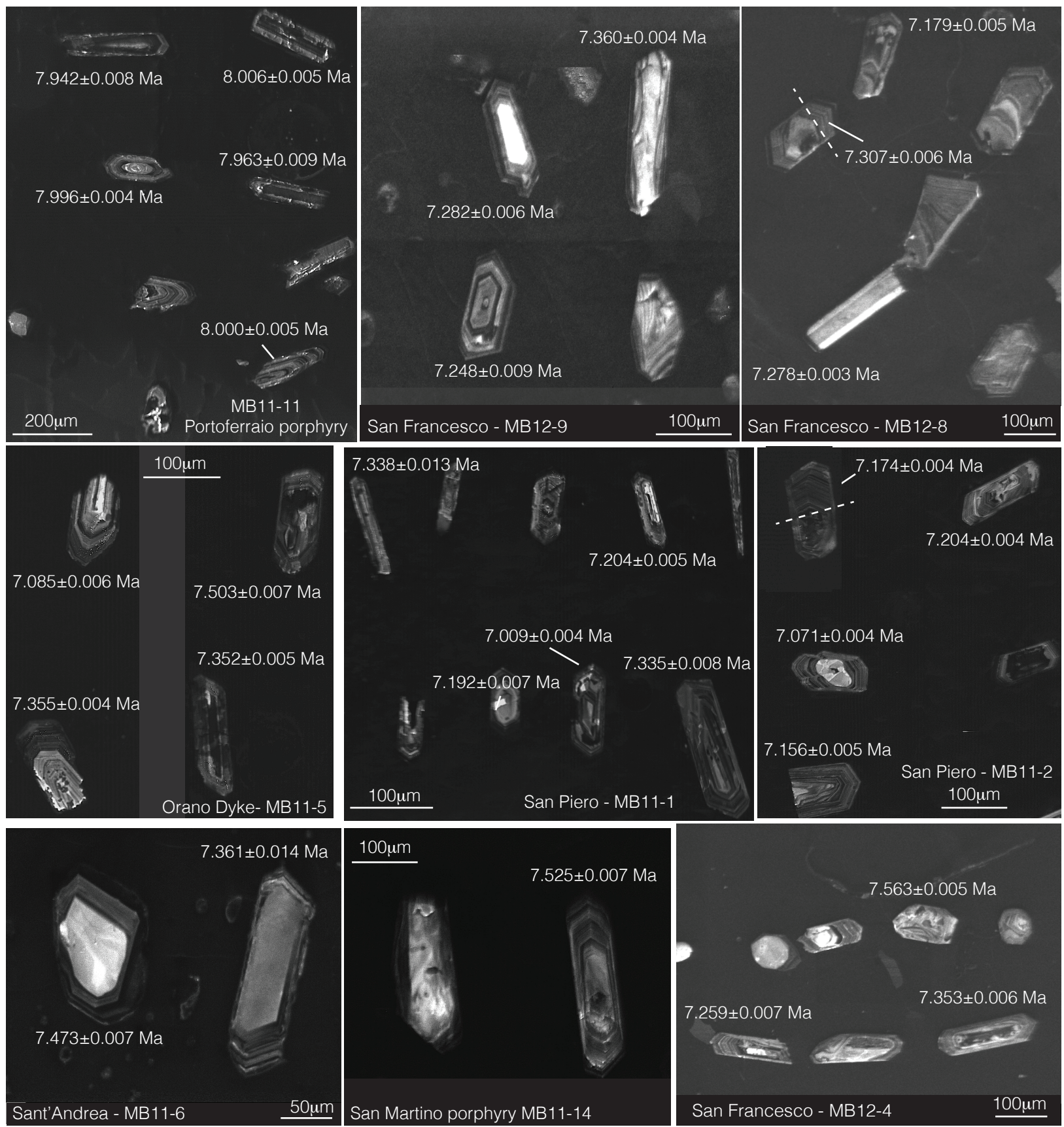
786

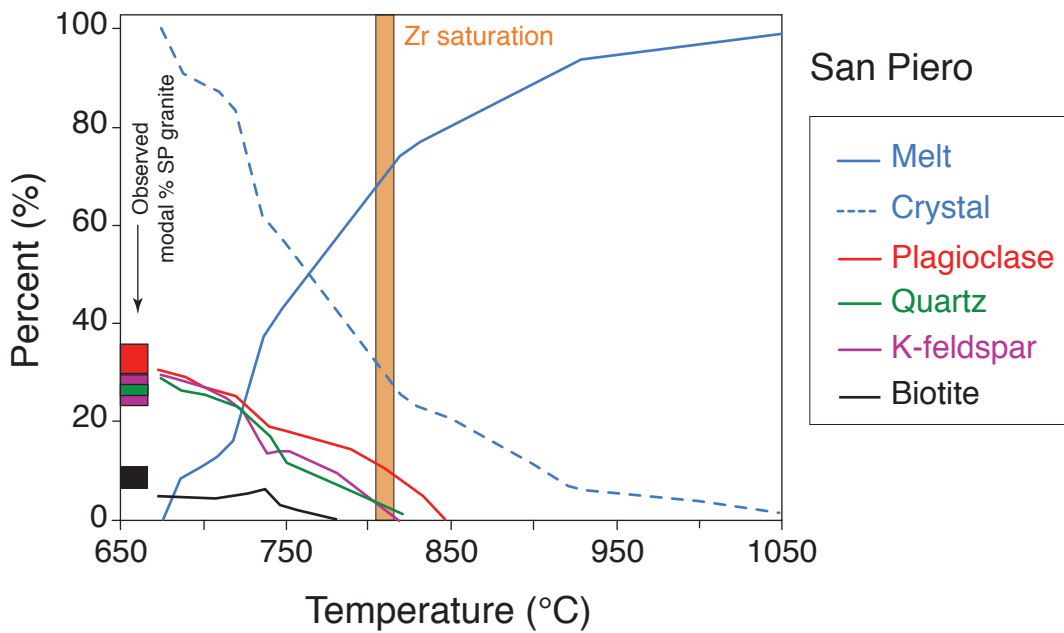
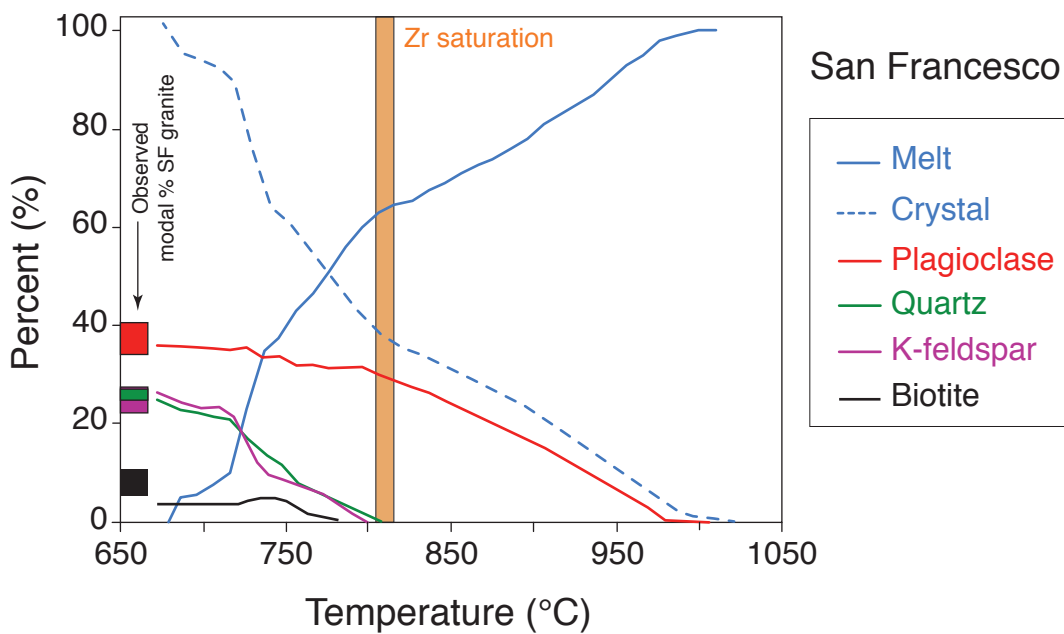
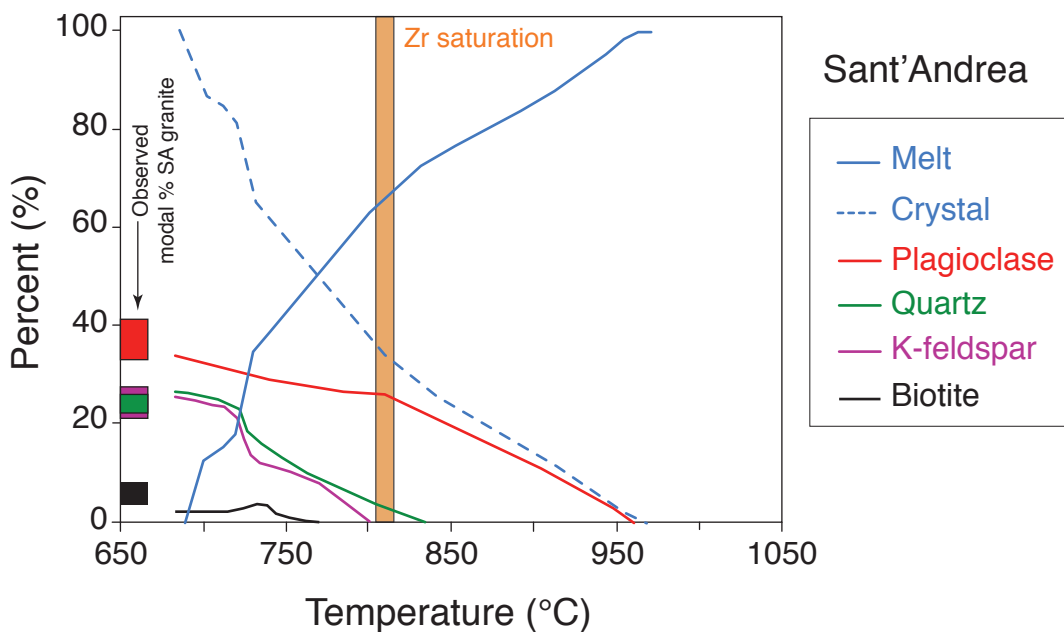
A



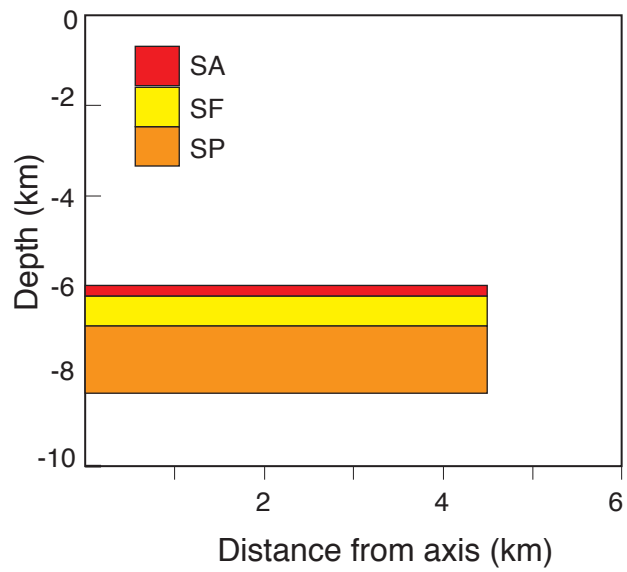
B



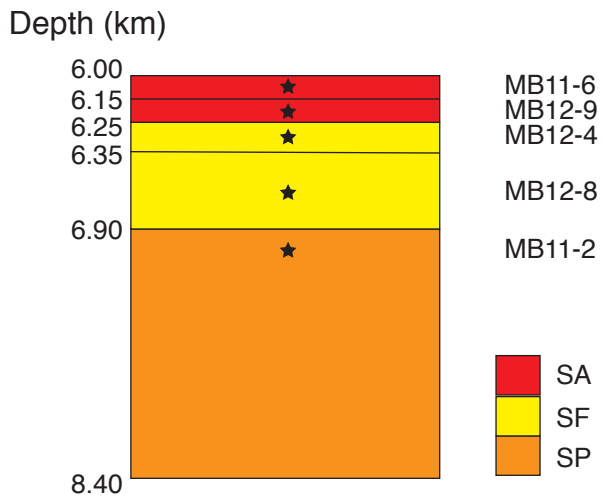


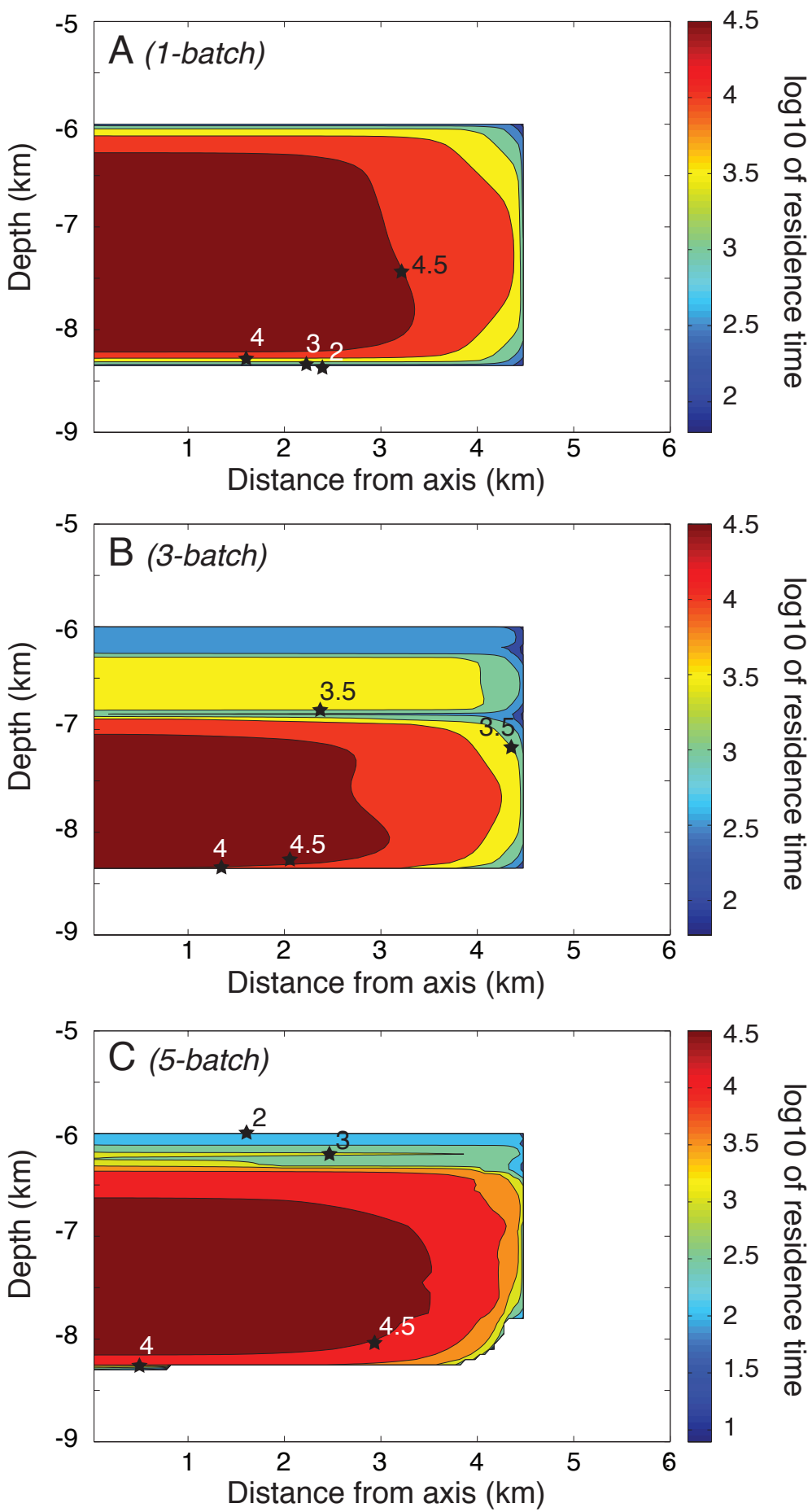


A



B





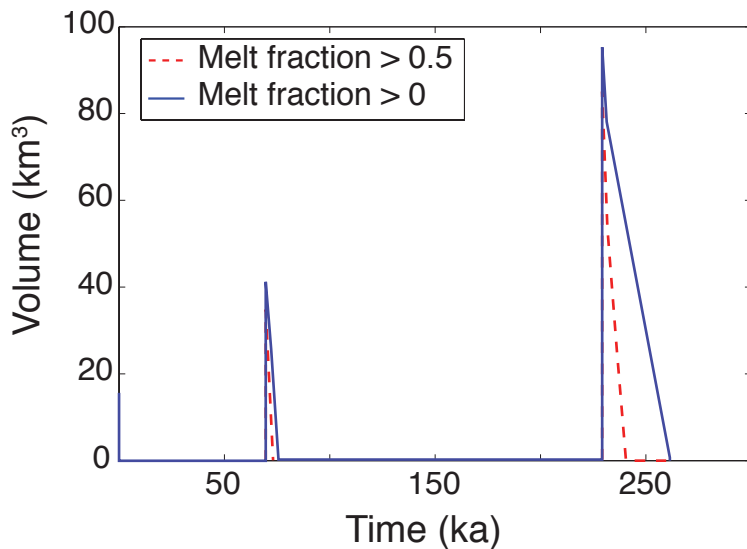
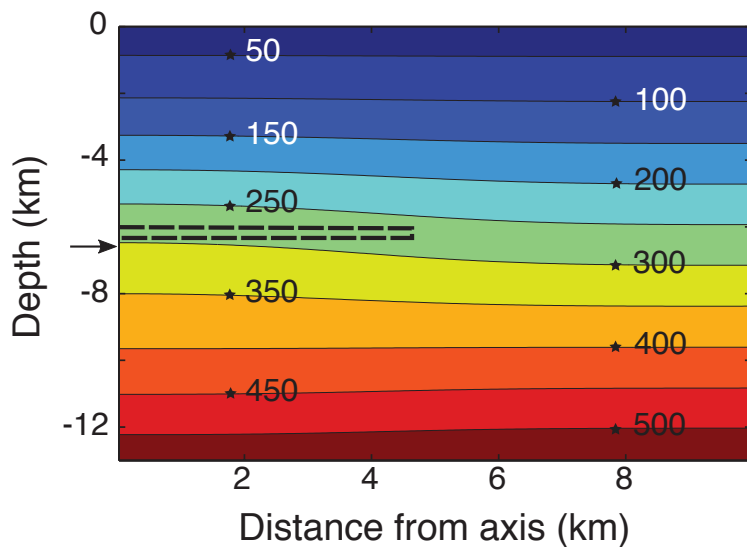
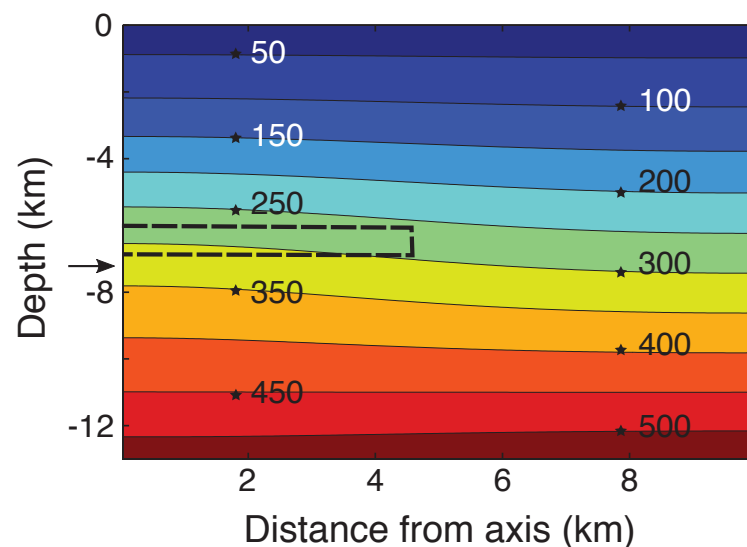
A**B****C**

Table 1 Zircon dates used in the thermal model

Facies	sample	Youngest zircon (Ma)	2-sigma (Ma)	Oldest zircon (Ma)	2-sigma (Ma)	Total age dispersion (ka)
SA	MB11-6	7.323	0.019	7.567	0.006	244 ± 20
SA	MB12-9	7.236	0.005	7.406	0.005	170 ± 7
SF	MB12-4	7.166	0.007	7.471	0.009	305 ± 11
SF	MB12-8	7.172	0.005	7.404	0.003	232 ± 5
SP	MB11-2	7.007	0.007	7.411	0.005	404 ± 9

Table 2 Three batches emplacement

Pulse	Pulse thickness (m)	Facies	Volume (km ³)
1	250	SA	17
2	650	SF	41
3	1500	SP	75

Case 1: Magma emplaced above zircon saturation temperature (20% crystals); the oldest zircon dates emplacement.

Pulse	Ages (Ma)	Sample	Emplacement time year	τ_{sample} (year) Geotherm = 25°C/km (1)	τ_{sample} (year) Geotherm = 40°C/km (1)
1	7.567	MB11-6	0	523	732
2	7.471	MB12-4	96317	1759	3576
3	7.411	MB11-2	156817	5673	20975
Pulse	Ages (Ma)	Sample	τ_{batch} (year) Geotherm = 25 °C/km (2)	τ_{batch} (year) Geotherm = 40°C/km (2)	Volumetric emplacement rate (km ³ yr ⁻¹)
1	7.567	MB11-6	567	775	1.25E-04
2	7.471	MB12-4	4217	6150	4.26E-04
3	7.411	MB11-2	32895	52060	4.78E-04

Case 2: Magma emplaced below zircon saturation temperature (40% crystals); the youngest zircon dates emplacement

Pulse	Ages (Ma)	Sample	Emplacement time year	τ_{sample} (year) Geotherm = 25°C/km (1)	τ_{sample} (year) Geotherm = 40°C/km (1)
1	7.236	MB12-9	0	141	165
2	7.166	MB12-4	70300	440	1098
3	7.007	MB11-2	229500	555	1593
Pulse	Ages (Ma)	Sample	τ_{batch} (year) Geotherm = 25 °C/km (2)	τ_{batch} (year) Geotherm = 40°C/km (2)	Volumetric emplacement rate (km ³ yr ⁻¹)
1	7.236	MB12-9	574	763	8.47E-05
2	7.166	MB12-4	4185	5433	5.83E-04
3	7.007	MB11-2	24490	32144	3.27E-04

(1) time spent by the magma between zircon saturation temperature and solidus at the sample paleodepth

(2) maximum time spent by the magma between zircon saturation temperature and solidus anywhere within a batch (see text)

Since cooling times are the longest close to the batch center, T_{batch} is significantly longer than T_{sample} if a sample has been collected far away from the batch center.

Table 3 Five batches emplacement

Case 1: Magma emplaced above zircon saturation temperature; the oldest zircon dates emplacement

Pulse	Facies	sample	Ages (Ma)	Pulse thickness (m)	Volume (km ³)	Sample depth (m)
1	SA	MB11-6	7.567	150	9	6050
2	SF	MB12-4	7.471	200	6	6300
3	SP	MB11-2	7.411	1500	13	6950
4	SA	MB12-9	7.406	100	27	6200
5	SF	MB12-8	7.404	450	75	6600

Pulse	Facies	sample	Ages (Ma)	Emplacement time year	τ_{sample} (year) Geotherm = 25°C/km (1)	τ_{sample} (year) Geotherm = 40°C/km (1)
1	SA	MB11-6	7.567	0	236	310
2	SF	MB12-4	7.471	96300	271	2132
3	SP	MB11-2	7.411	156800	44396	58548
4	SA	MB12-9	7.406	161900	803	1133
5	SF	MB12-8	7.404	163700	21050	30012

Pulse	Facies	sample	Ages (Ma)	τ_{batch} (year) Geotherm = 25 °C/km(2)	τ_{batch} (year) Geotherm = 40°C/km(2)	Volumetric emplacement rate (km ³ yr ⁻¹)
1	SA	MB11-6	7.567	236	314	6.63E-05
2	SF	MB12-4	7.471	8486	15112	1.35E-04
3	SP	MB11-2	7.411	52167	65686	4.78E-04
4	SA	MB12-9	7.406	803	1133	3.71E-05
5	SF	MB12-8	7.404	37200	48670	1.65E-04

(1) time spent by the magma between zircon saturation temperature and solidus at the sample paleodepth

(2) maximum time spent by the magma between zircon saturation temperature and solidus anywhere within a batch (see text)

Since cooling times are the longest close to the batch center, T_{batch} is significantly longer than T_{sample} if a sample has been collected far away from the batch center.

Table 3 (cont) Five batches emplacement

Case 2: Magma emplaced below zircon saturation temperature; the youngest zircon dates emplacement

Pulse	Facies	sample	Ages (Ma)	Pulse thickness (m)	Volume (km ³)	Sample depth (m)
1	SA	MB11-6	7.323	150	9	6050
2	SA	MB12-9	7.236	100	6	6200
3	SF	MB12-4	7.166	200	13	6300
4	SF	MB12-8	7.172	450	27	6600
5	SP	MB11-2	7.007	1500	75	6950

Pulse	Facies	sample	Ages (Ma)	Emplacement time year	τ_{sample} (year) Geotherm = 25°C/km (1)	τ_{sample} (year) Geotherm = 40°C/km (1)
1	SA	MB11-6	7.323	0	248	299
2	SA	MB12-9	7.236	89600	98	122
3	SF	MB12-4	7.166	159900	405	500
4	SF	MB12-8	7.172	165500	2518	3297
5	SP	MB11-2	7.007	333200	814	1424

Pulse	Facies	sample	Ages (Ma)	τ_{batch} (year) Geotherm = 25 °C/km(2)	τ_{batch} (year) Geotherm = 40°C/km(2)	Volumetric emplacement rate (km ³ yr ⁻¹)
1	SA	MB11-6	7.323	248	299	4.49E-05
2	SA	MB12-9	7.236	98	122	6.70E-05
3	SF	MB12-4	7.166	409	503	8.13E-05
4	SF	MB12-8	7.172	2636	3438	1.63E-04
5	SP	MB11-2	7.007	24314	30783	2.25E-04

(1) time spent by the magma above solidus at the sample paleodepth

(2) maximum time spent by the magma above solidus anywhere within a batch (see text)

Since cooling times are the longest close to the batch center, T_{batch} is significantly longer than T_{sample} if a sample has been collected far away from the batch center.

S1. Hand sample and zircon description:

Portoferraio and San Martino Porphyries:

The Portoferraio sample was collected near the “Aquavita” locality (Fig.1 of the main text). Latitude and Longitude (WGS84) are N 42°49'21.6"/E 10°17'13.6". It is a biotite-bearing monzogranite containing quartz phenocrysts set in a very fine matrix (Supplement Fig.1A). Zircons are very abundant, included both in the matrix and as inclusions in biotite. The present a euhedral and prismatic shape and range in size from 50-300 μ m in length, but mostly 70-200 μ m. Cathodoluminescence (CL) imaging of zircon shows oscillatory zoning typical of igneous zircon, with some grains displaying rounded cores and truncated oscillatory zoning or sector zoning (Fig.2 of the main text).

Barboni and Schoene, (2014), described the San Martino (SM) porphyry sample (MB11-14). It was collected near the “La Focce” locality (Fig.1 of the main text). Latitude and longitude (WGS84) are: N 42°74'65.4"/E 10°25'02.8". It is a biotite-bearing monzogranite containing prominent sanidine megacrysts set in a fine-grained groundmass (Supplement Fig.1B). The zircon grains are euhedral and prismatic ranging in size from 50-400 μ m in length, but mostly 100-250 μ m. Cathodoluminescence (CL) imaging of zircon shows oscillatory zoning typical of igneous zircon, though some grains contain rounded cores with truncated oscillatory zoning or sector zoning (Fig.2 of the main text).

Orano Dyke:

We collected the Orano sample from a dyke that was crosscutting the Sant’Andrea facies of the Mt. Capanne intrusion, West of the town of “Chiessi (Fig.1 of the main text; supplement Fig.3C). Latitude and longitude (WGS84) are N 42°75'89.8"/E 10°29'68.2". It is a quartz monzodiorite containing resorbed xenocrysts of quartz and K-feldspar, as well as mafic microgranular enclaves (MME) and xenoliths (insert in Supplement Fig.3C). Zircon is located in the groundmass and in inclusion in biotite. Although the largest enclaves and xenocrysts from the sample prior to crushing and zircon extraction, some smaller ones were unavoidable during crushing. The zircons therefore represent a mixed population including grains from the host granite, the MME and smaller megacrysts. The zircon grains are euhedral and prismatic ranging in size from 50-200 μ m in length, but mostly 50-150 μ m. Cathodoluminescence (CL) imaging of zircon shows oscillatory zoning typical of igneous zircon, though some grains contain rounded cores with truncated oscillatory zoning or sector zoning (Fig.2 of the main text).

Mt. Capanne pluton:

The Sant’Andrea (SA) facies rock samples were collected on the Sant’Andrea beach for MB11-6 (Fig. 1 of the main text; WGS84 latitude and longitude of N 42°80'80.1" /E 10°14'09.1"; described in Barboni and Schoene, 2014), and in the Pomonte quarry for MB12-9 (Fig. 1 of the main text; WGS84 latitude and longitude of N 42°75'08.4" /E 10°12'93.9"). Both are biotite-bearing monzogranites that contains numerous mafic microgranular enclaves (MME) and K-feldspar megacrysts (Supplementary Fig.1D). Modal proportions are the following: 38% An₃₅₋₁₂ plagioclase, 27% quartz, 22% orthoclase (Or₆₅₋₈₁), 13% biotite and accessories (apatite, zircon, tour-

maline, allanite, titanite and oxides). Zircon is located both in the matrix and included in plagioclase, orthoclase and biotite. Although the largest MME and K-feldspar were removed from the sample prior to crushing and zircon extraction, some smaller ones were unavoidable during crushing. The zircons therefore represent a mixed population including grains from the host granite, the MME and smaller megacrysts. Zircons are euhedral and prismatic, mostly elongate; grain size ranges from 50-500 μm in length, but are mostly 100-300 μm . Cathodoluminescence (CL) imaging of zircon shows oscillatory zoning typical of an igneous origin. Most of the Sant'Andrea zircon grains have rounded cores with truncated oscillatory zoning or sector zoning, sometimes showing a patchy texture (Fig.2 of the main text).

The San Francesco (SF) facies rock samples were collected near the contact with the San Piero facies on the road above the “Torre Giovanni” for sample MB12-8 (Fig. 1 of the main text; WGS84 latitude and longitude of N 42°76'93.2" /E 10°18'77.9"), and 50m bellow the summit of the Mt.Capanne for sample MB12-4 (Fig. 1 of the main text; WGS84 latitude and longitude of N 42°77'09.5" /E 10°16'89.5"). Both samples are biotite-bearing monzogranites that are very similar in compositions and modal proportion as the Sant'Andrea samples described above, at the exception of a lower content of MME and K-feldspar megacrysts and a slightly lower SiO₂ wt% composition (Supplement Fig.1E). Zircons from both samples present similar characteristics that the one from the two SA samples.

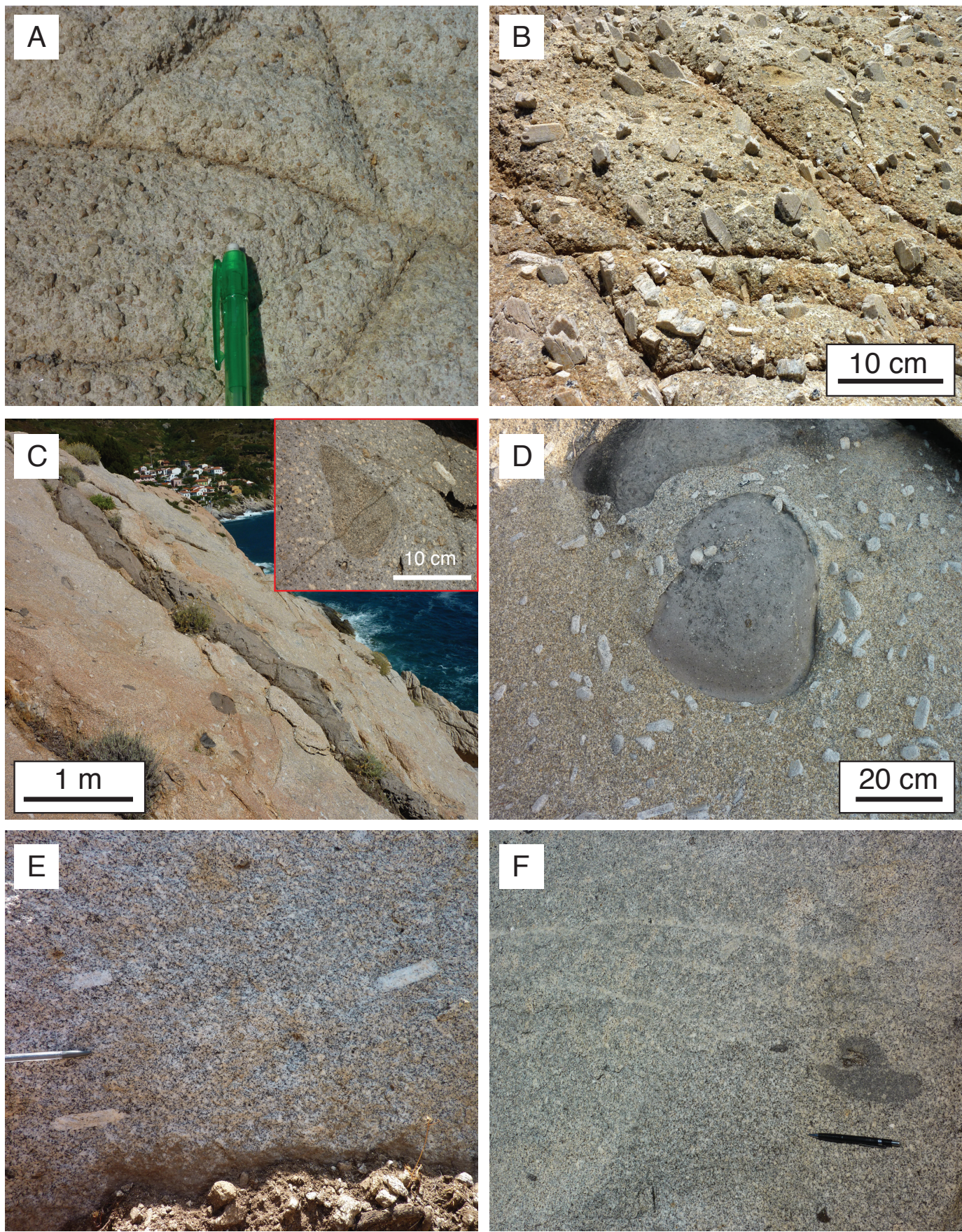
The San Piero (SP) facies rocks were collected in the San Piero quarry for MB11-1 (Fig. 1 of the main text; WGS84 latitude and longitude of N 42°74'67.2" /E 10°20'88.5"), and on the road bellow the “Torre Giovanni” (close to the contact with the San Francesco facies) for MB11-2 (Fig. 1 of the main text; WGS84 latitude and longitude of N 42°76'23.4" /E 10°20'07.6"). Both samples are monzogranites and did not contain any MME or K-feldspar megacrysts (Supplement Fig.1F). Zircons from both samples present similar characteristics that the one from the SA and SF samples.

S2. Methodology

2.1 U-Pb methodology

All samples were processed and analyzed at Princeton University. Zircon separates were prepared by standard density and magnetic mineral separation methods (crushing and milling; sieving to <500 μm ; concentration via hand-panning; magnetic separation; hand-picking). All the zircons were dated by removing grains that were imaged by CL from the epoxy mount, in order to document any correlations between internal textures and dates and also to target the simplest zircons (representative images are shown in fig.2 of the main text). However, there was no obvious correlation between the dates of the grains and the amount of core material observed in the zircon, the type of zoning (sector vs. oscillatory), the number of growth episodes, nor the brightness of the zoning. When xenocrystic cores were identified, we cut the zircon following the CL imaging in order to insolate and date only the tips (representative images are shown in fig.2 of the main text).

Analyses were performed following the same procedure as described in Barboni and Schoene, (2014) and is repeated here. Annealing was performed by loading the zircons of each sample in quartz crucibles, which were heated at 900°C for ca. 48h. Zircons were removed from Epoxy grainmount following CL imaging, loaded into 200 μl savellex capsules, leached in HF + trace HNO₃ for ca. 12 hours at 190°C and rinsed with water, 6N HCl



Supplementary Fig.1. A) Portoferaio Porphyry (sample MB11-11). B) San Martino Porphyry (sample MB11-14). C) Orano dyke crosscutting the Sant'Andrea facies of the Mt. Capanne intrusions (sample MB11-5). D) Mafic enclaves and K-feldspar megacrysts in the Sant'Andrea facies of the Capanne intrusions. F) San Francesco facies of the Capanne intrusion. D) San Piero facies of the Capanne intrusion.

and HF. Each grain was spiked with ca. 0.006 g of the EARTHTIME ^{205}Pb - ^{233}U - ^{235}U tracer solution (Condon et al., in press; Mclean et al., in press). Zircons were subsequently dissolved in ca. 70 μl 140% HF and trace HNO_3 at 210°C for 48+ hours, dried down and redissolved in 6N HCl overnight. Samples were then dried down and redissolved in 3N HCl and put through a modified single 50 μl column HCl-based anion exchange chemistry (Krogh, 1973). U and Pb were collected in single beakers, dried down with a drop of 0.02 M H_3PO_4 , and analyzed on a single outgassed Re filament in Si-gel emitter (modified from Gerstenberg and Haase, 1997).

Measurements were performed on an IsotopX Phoenix62 thermal ionization mass spectrometer at Princeton University. Pb was measured in dynamic mode on an axial ion-counting Daly photomultiplier. Deadtime for the Daly was determined at 40.5 ns by repeated measurements of NBS-981 and NBS-982 for up to 2.5 Mcps. Lead mass fractionation was calibrated by repeated NBS-981 measurements (mean α ^{208}Pb - ^{206}Pb = $0.18 \pm 0.04\text{ \% / amu}$, 2-sigma standard deviation) on mixed Pb-U aliquots of <100 pg Pb to closely imitate sample running behavior. Baseline measurements were made at each half-mass and the average intensity bounding each measured peak was subtracted. Isobaric interferences on ^{205}Pb were monitored by measuring mass 203, but repeated analyses of unspiked zircon show that the intensity of non- ^{205}Pb ions under mass 205 is trivial for this study. As a result, no corrections were applied, and the decay of mass 203 over the duration of the analysis relative to Pb is used as an indicator of declining isobaric interferences under all Pb masses. Data culling was done using decreasing 203/205 and increasing 206/204 ratios over the course of an analysis. U was measured in static mode on Faraday cups on 10^{12} ohm resistors as UO_2^+ . $^{233}\text{UO}_2$ and $^{235}\text{UO}_2$ were corrected for an oxygen isotopic composition of 0.002055 (see discussion in Condon et al., in press). Because $^{18}\text{O}/^{16}\text{O}$ typically grows at the beginning of an analysis before stabilizing, early blocks of data were deleted. Baselines were measured at ± 0.5 mass units for 15 seconds every 10 ratios. Correction for mass-fractionation of U was done using the EARTHTIME ^{205}Pb - ^{233}U - ^{235}U tracer solution assuming a sample $^{238}\text{U}/^{235}\text{U}$ ratio of 137.818 ± 0.021 (Hiess et al., 2012). All data reduction, error propagation and plotting of U-Pb data was done using the U-Pb_Redux software package (Bowring et al., 2011; McLean et al., 2011). All reported uncertainties are 2-sigma and include internal sources of uncertainty only. Including systematic sources of uncertainty such as tracer composition and decay constants should be carried out for comparison with U-Pb data collected using a different tracer or with other isotopic systems, and can be done by accessing data from this study on the Geochron data storage website, given the uncertainties for tracer composition reported in Condon et al. (in press) and uncertainties for decay constants discussed in Schoene et al. (2006).

21 procedural blanks were measured over the course of this study, spiked with the same tracer. The amount of Pb in the total procedural blanks (0.5-3.6 pg; avg. 1.1 pg) agreed well with that found in zircon analyses, and therefore all common Pb is assumed to derive from procedural blanks. After 2-sigma outlier rejection, the composition of 19 ^{205}Pb - ^{233}U - ^{235}U -spiked blanks was: $^{206}\text{Pb}/^{204}\text{Pb}$ = 18.50 ± 0.10 , $^{207}\text{Pb}/^{204}\text{Pb}$ = 15.56 ± 0.21 , $^{208}\text{Pb}/^{204}\text{Pb}$ = 37.48 ± 0.34 (2-sigma standard deviation), and these uncertainties were propagated into each U-Pb analysis.

An important consideration in U-Pb geochronology of ca. 7 Ma zircons is the correction for initial secular disequilibrium in the U-Pb decay chain. During zircon crystallization, intermediate daughters products can be incorporated or excluded from the crystal depending on the zircon/magma distribution coefficient for each element. Our primary concern is the exclusion of ^{230}Th ($t_{1/2} = 75,380$ years), a long-lived intermediate daughter product of ^{238}U , as initial depletion leads to a deficiency of ^{206}Pb and therefore apparent $^{206}\text{Pb}/^{238}\text{U}$ dates that are too young. This effect is generally corrected by using a model $\text{Th}/\text{U}_{\text{zircon}}$ calculated from the blank-subtracted $^{208}\text{Pb}/^{206}\text{Pb}_{\text{zircon}}$ measured by ID-TIMS and an estimate of the $\text{Th}/\text{U}_{\text{magma}}$ at the time of the zircon crystallization.

We calculated the Th/U_{magma} for each dated zircon by using the model Th/U_{zircon} and Th/U zircon/melt distribution coefficients (D) experimentally determined by Rubatto and Hermann (2007) for hydrous granitic melt at 800°C (DTh = 41±4; DU =167±17). Uncertainties on the distribution coefficients were not propagated into our age uncertainties because this uncertainty is regarded as systematic for each grain, assuming a restricted temperature and compositional range of the magma. Additionally, the effect of changing intensive variables on the ratio of partition coefficients (DTh/U) is far less than the absolute values of each, further supporting the systematic nature of this uncertainty. As such, the differences between dated grains are insensitive to the disequilibrium correction. Our calculated values for Th/U_{magma} are reported in Supplementary Table 1, and while these are not meant to be robust estimates of magma composition, they do illustrate that they yield Th/U_{magma} ratios that are reasonable for the Elba samples.

2.2 Ryholite-MELTS model

The crystallization sequence of the Sant'Andrea, San Francesco and San Piero magmas was simulated using the modeling package Rhyolite-MELTS optimized for silica-rich, fluid-bearing magmatic systems (Gualda et al., 2012). We assumed closed system crystallization at isobaric conditions, regulated by the QFM oxygen fugacity buffer. Starting liquid equivalent to the whole-rock compositions of the Sant'Andrea facies sample PP-334 (Dini et al., 2002), San Francesco facies sample PP-364 (Dini et al., 2002) and San Piero facies sample MB11-2 (this study) were used. All these samples are close to the average composition of all samples reported for each facies in the literature (Dini et al., 2002; Farina et al., 2010). Other compositions do not significantly change the results.

We performed multiple runs for pressures ranging from 2 to 5 kbar and water contents between 1 and 6 wt%, with temperatures decreasing from 1200 to 500°C for each of the Capanne facies. Each run with different conditions was discarded if not closely matching observed petrological observations or modal proportions and microprobe mineral measurements (Bussy, 1991) made on Sant'Andrea granite thin sections. We noticed that MELTS could not produce results below a pressure of 2.3 kbar. As our study tries to model the cooling evolution of the Capanne granite at emplacement level (ca. 2 Kbar; Bussy, 1991), we narrowed our selection to runs computed for 2.3 kbar. Our best-fit models for the three samples were performed with initial water content of 2 wt% (Supplement Fig.2A-2C). Though this water content best fit the observed mineral assemblages, we note that the absolute temperatures calculated (Supplementary Table 2) are very sensitive to the assumed water content. Uncertainties in these temperatures are therefore on the order of ±20°C for water contents of 1.5-2.5 %, with the added constraint that zircon saturation (807±11 °C, see Supplementary Methods section 2.3) must have occurred at <40% crystal content as indicated by pre-emplacement zircon crystallization and the megacryst inclusion history reported by Barboni and Schoene, (2014). Orthopyroxene was intentionally excluded as they were not observed, and MELTS produced them at the expense of biotite. The MELTS raw data are presented in Supplementary Table 2.

2.3 Zr-saturation temperature

Zircon saturation temperature was estimated using the same technique as described in Barboni and Schoene, (2014). Published saturation experiments (Watson and Harrison, 1983; Boehnke et al., 2013) were integrated with our MELTS model. We assumed an initial melt Zr concentration equal to bulk rock and calculated liquid Zr con-

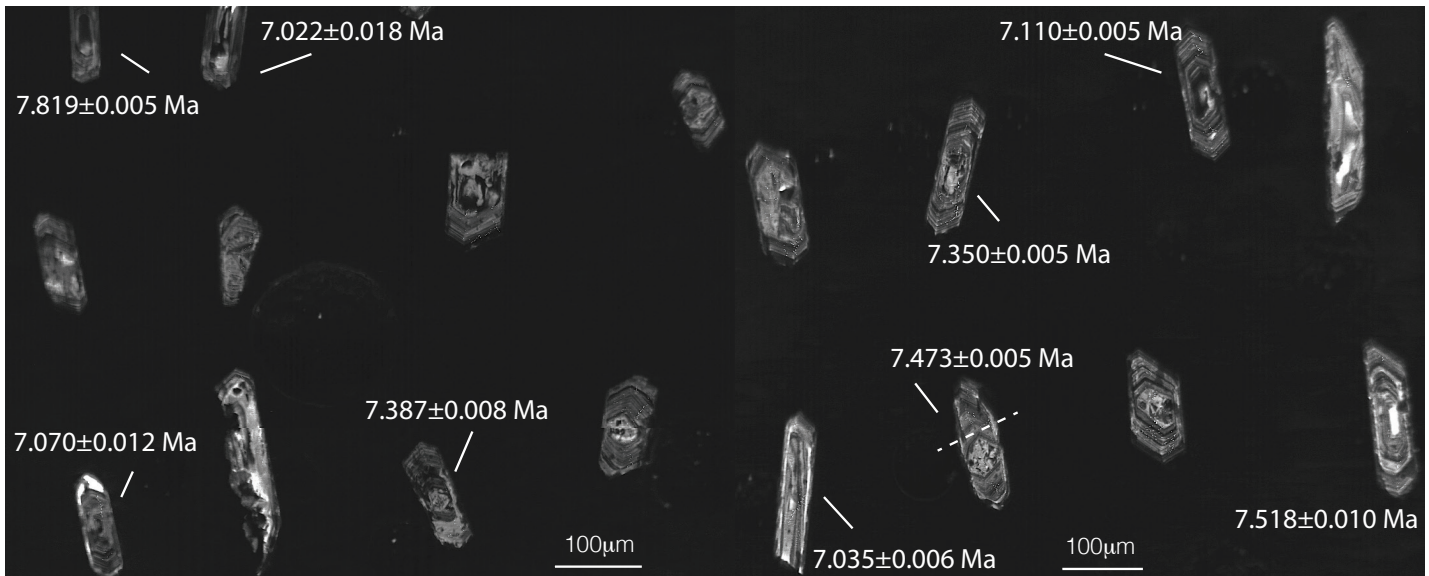
tent during crystallization using bulk partition coefficients (from the GERM database: <http://earthref.org/GERM/>) for the saturated phases predicted by MELTS. The major element composition of the coexisting liquid was used to determine the M parameter used in the zircon saturation calculation (Supplementary Table 3 and Supplementary Fig. 2). We then calculated the Zr concentration required for saturation in the evolving liquid using Watson and Harrison (1983) and Boehnke et al. (2013), yielding temperatures of ca. 805 °C for all three Capanne facies, ~10–50 °C hotter than that predicted using only bulk rock chemistry alone (Watson and Harrison, 1983; Supplement Fig.2). Uncertainties of ±11 °C in this temperature were calculated by calculating the maximum and minimum temperature permitted by the calibration uncertainties reported in Boehnke et al. (2013).

References cited

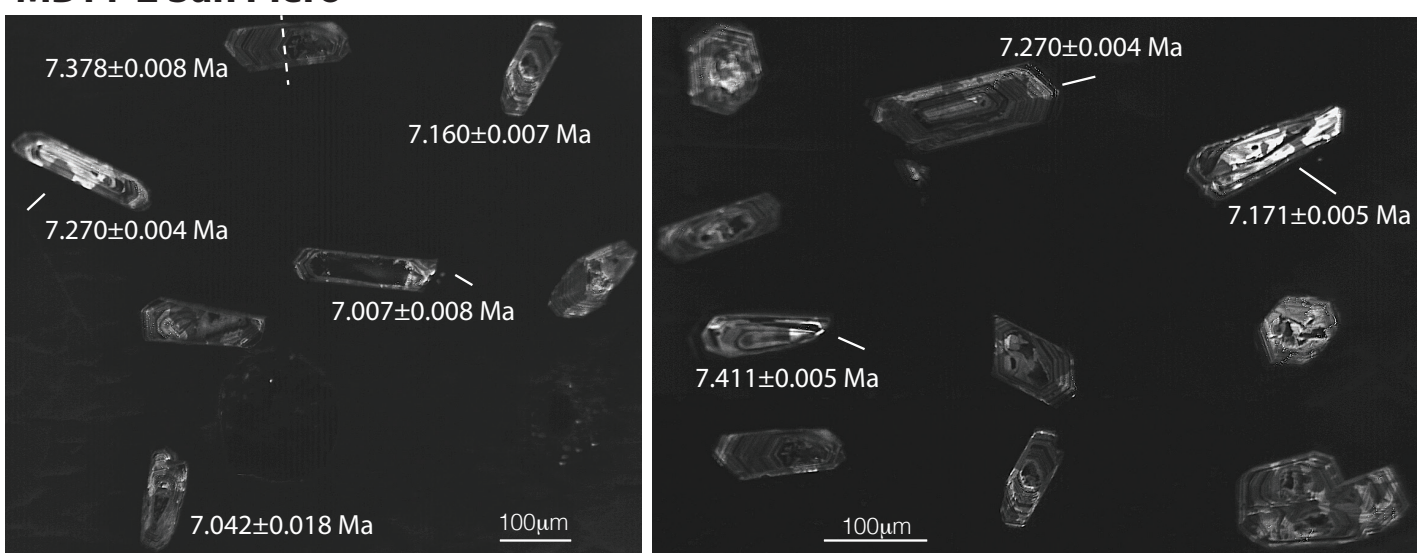
- Barboni, M. and Schoene, B. Short eruption window revealed by absolute growth rates in a granitic magma. *Nature Geosciences*. 7, 524-528 (2014)
- Boehnke, P., Watson, E.B., Trail, D., Harrison, T. M. & Schmitt, A.K. Zircon Saturation Re-revisited. *Chem. Geol.* 351, 324-334 (2013).
- Bowring, J. F., McLean, N. M. & Bowring, S. A. Engineering cyber infrastructure for U-Pb geochronology: Tripoli and U-Pb_Redux. *Geochem., Geophys., Geosyst.* 12, Q0AA19 (2011).
- Bussy, F. Pétrogenèse des Enclaves Microgrenues Associées aux Granitoïds Calco-Alcalins: Exemple des Massifs Varisques du Mont-Blanc (Alpes Occidentales) et Miocène du Monte Capanne (Ile d'Elbe, Italie): Lausanne, Switzerland, Mémoires de Géologie 7, 309 p. (1990).
- Condon, D. J., Schoene, B., McLean, N. M., Bowring, S. A., & Parrish, R. R., in press, Metrology and Traceability of U-Pb Isotope Dilution Geochronology (EARTHTIME 1 Tracer Calibration Part I). *Geochim. Cosmochim. Acta*.
- Dini, A., Innocenti, F., Rocchi, S., Tonarini, S., & Westerman, D.S. The magmatic evolution of the laccolith-pluton-dyke complex of Elba Island, Italy. *Geol. Mag.* 139, 257–279 (2002).
- Farina, F., Dini, A., Innocenti, F. Rocchi, S. & Westerman, D.S. Rapid incremental assembly of the Monte Capanne pluton (Elba Island, Tuscany) by downward stacking of magma sheets. *Geol. Soc. Am. Bull.* 122, 1463-1479 (2010).
- Gerstenberger, H., & Haase, G. A highly effective emitter substance for mass spectrometric Pb isotope ratio determinations: *Chem. Geol.* 136, 309-312 (1997).
- Harrison, T.M., Watson & Aikman, A.K. Temperature spectra of zircon crystallization in plutonic rocks. *Geology* 35, 635-638 (2007).
- Jaffey, A.H., Flynn, K.F., Glendenin, L.E., Bentley, W.C., and Essling, A.M., 1971, Precision measurement of half-lives and specific activities of ^{235}U and ^{238}U : *Physical Review*, v. C4, p. 1889-1906.
- Krogh, T.E. A low contamination method for hydrothermal decomposition of zircon and extraction of U and Pb for isotopic age determination: *Geochim. Cosmochim. Acta*, 37, 485-494 (1973).
- Mattinson, J.M. Zircon U-Pb chemical-abrasion (“CA-TIMS”) method: combined annealing and multi-step dissolution analysis for improved precision and accuracy of zircon ages: *Chem. Geol.*, 220, 47-56 (2005).
- McLean, N. M., Bowring, J. F. & Bowring, S. A. An algorithm for U-Pb isotope dilution data reduction and uncertainty propagation. *Geochem. Geophys. Geosyst.* 12, Q0AA18 (2011).
- McLean NM, Condon DC, Schoene B, Bowring SA, *in press*, Evaluating uncertainties in the calibration of isotopic reference materials and multi-element isotopic tracers (EARTHTIME tracer calibration part II), *Geochim. Cosmochim. Acta*
- Rubatto, D. & Hermann, J. Experimental zircon/melt and zircon/garnet trace element partitioning and implications for the geochronology of crustal rocks. *Chem. Geol.* 241, 38-61 (2007).

- Schoene, B., Crowley, J. L., Condon, D. C., Schmitz, M. D., and Bowring, S. A. Reassessing the uranium decay constants for geochronology using ID-TIMS U-Pb data: *Geochim. Cosmochim. Acta* 70, 426-445 (2006).
- Watson, E. B. & Harrison, T. M. Zircon saturation revisited: temperature and composition effects in a variety of crustal magma types. *Earth Planet. Sci. Lett.* 64, 295–304 (1983).

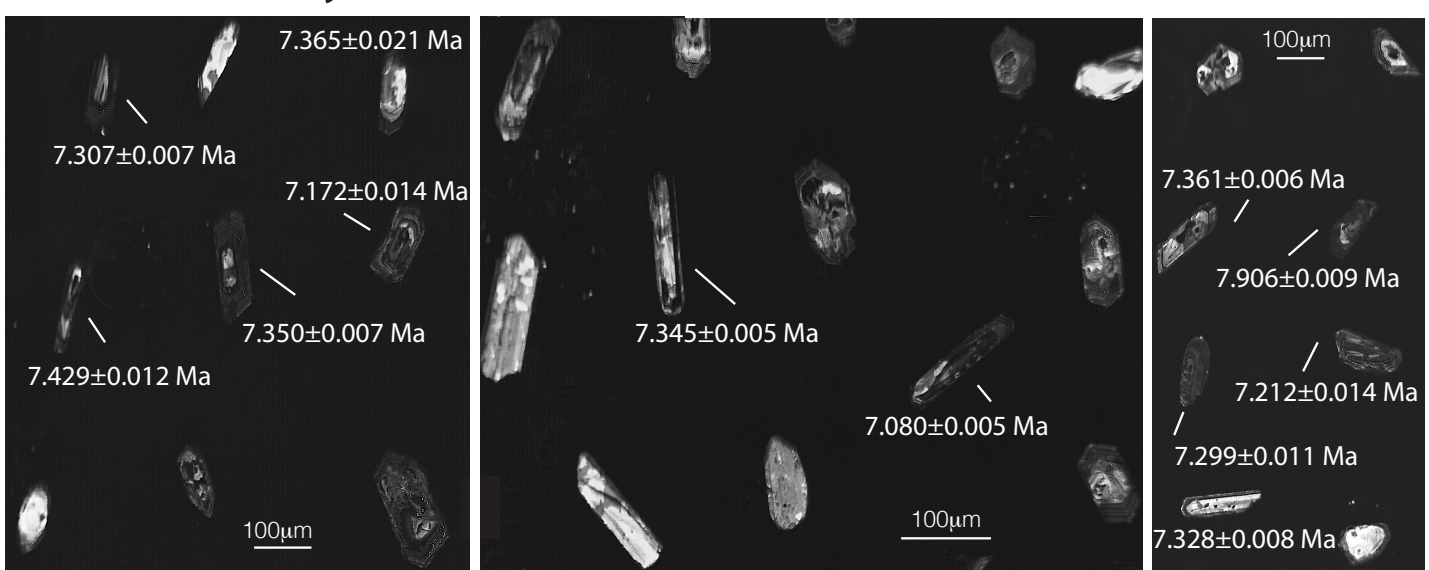
MB11-1 San Piero



MB11-2 San Piero

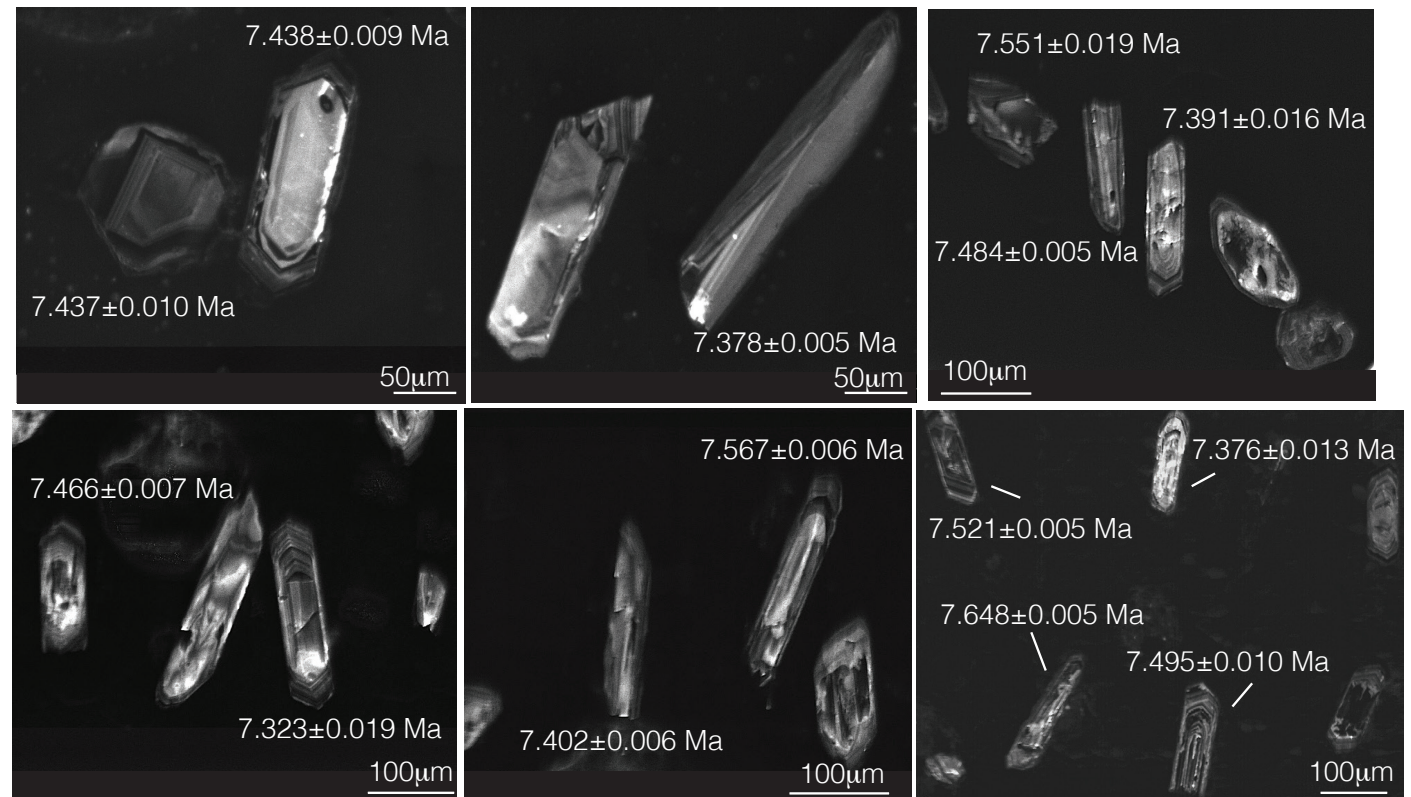


MB11-5 Orano Dyke

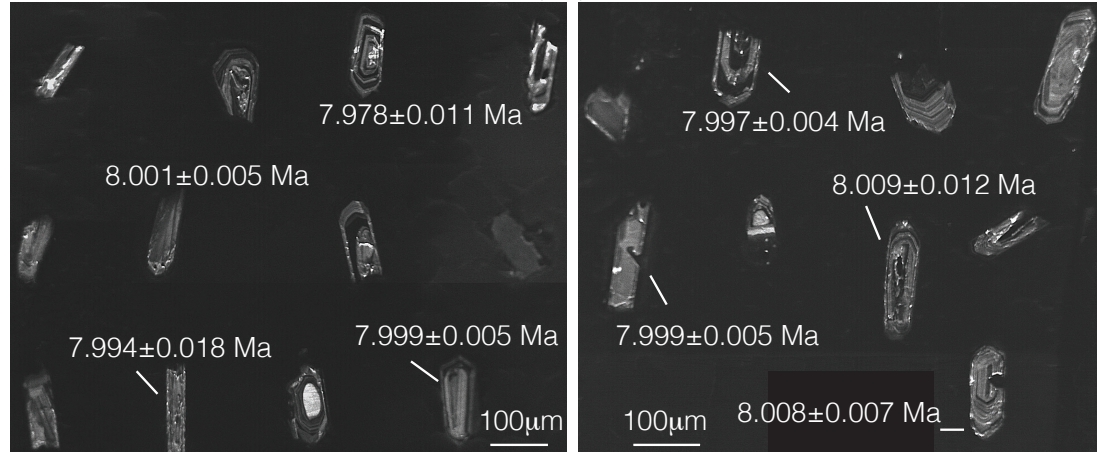


Supplementary Fig.2. CL images of the zircon measured in this study with u-Pb ages (2-sigma uncertainties)

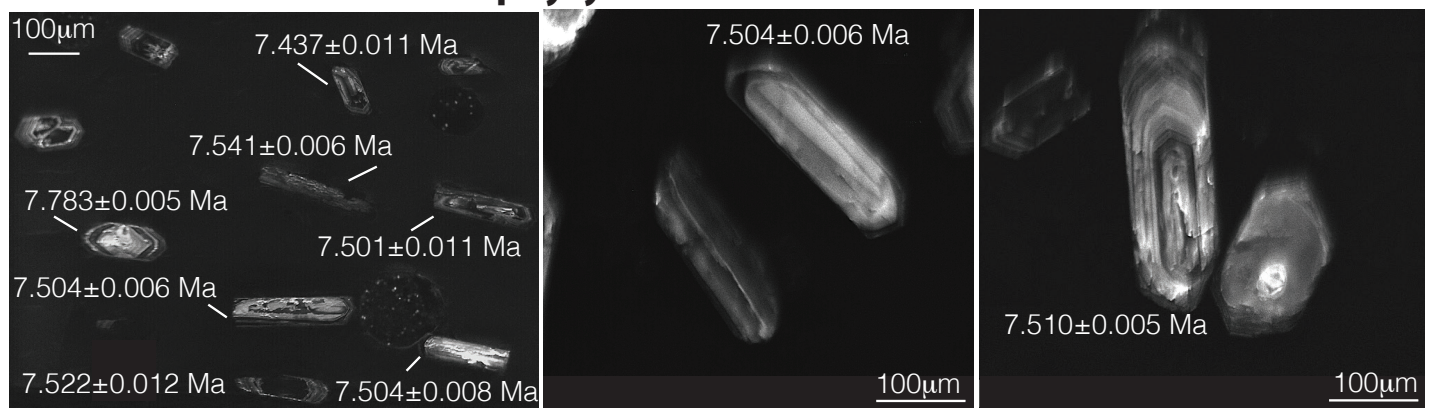
MB11-6 Sant Andrea



MB11-11 Portoferaio Porphyry

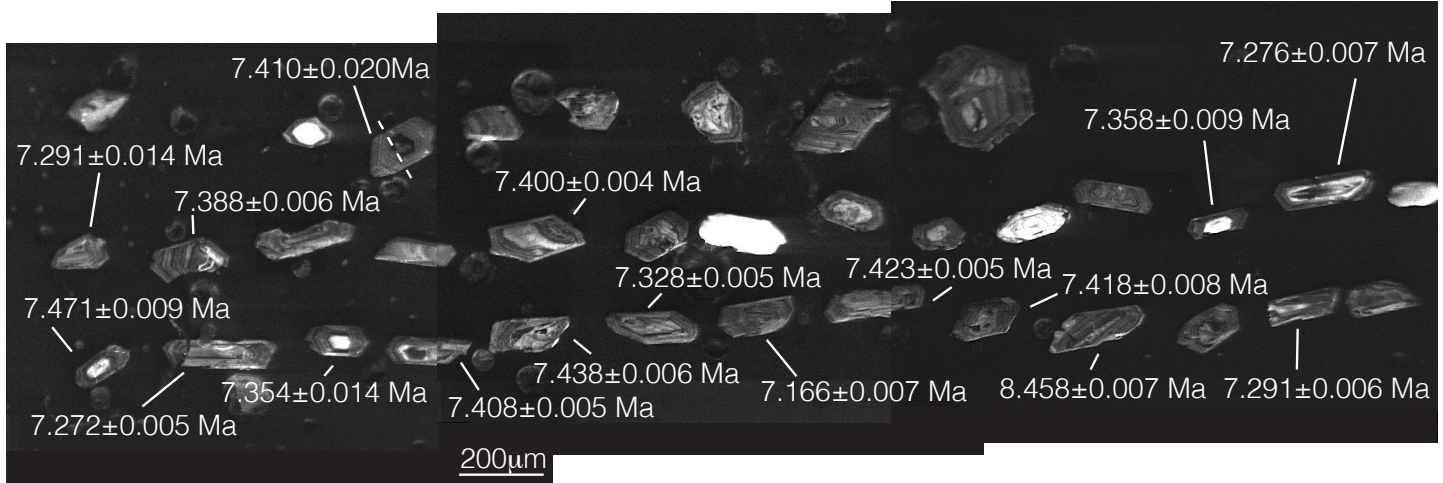


MB11-14 San Martino Porphyry

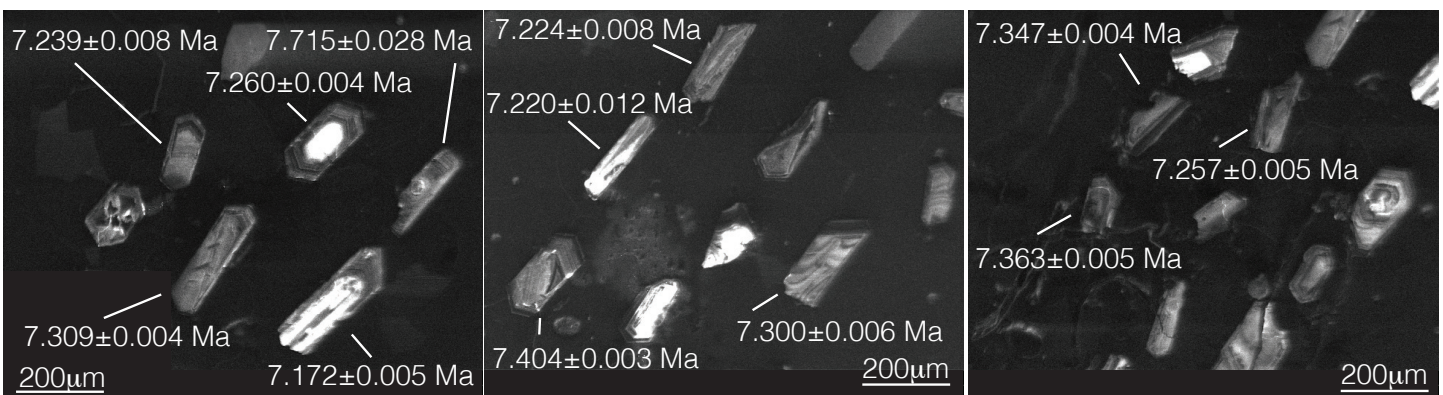


Supplementary Fig.2. CL images of the zircon measured in this study with u-Pb ages (2-sigma uncertainties)

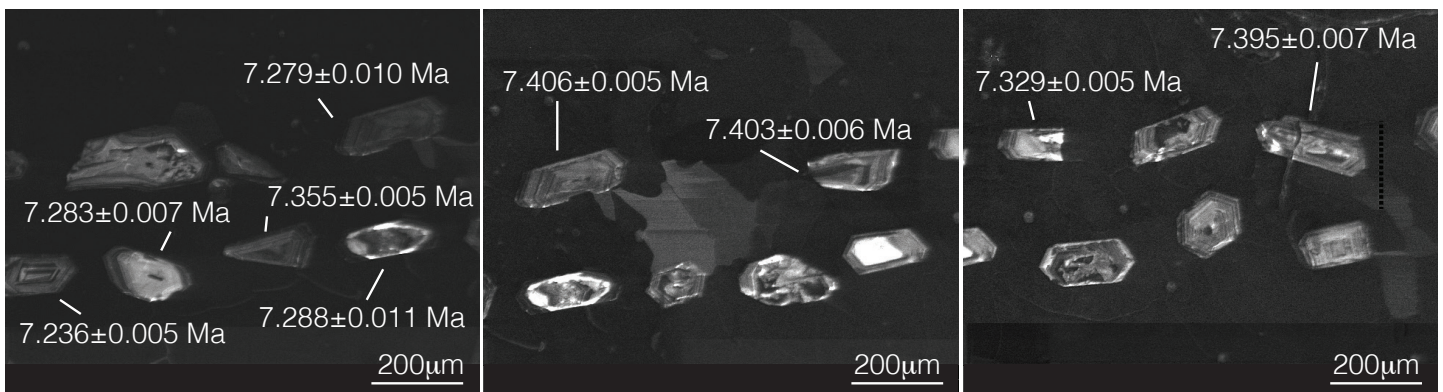
MB12-4 San Francesco



MB12-8 San Francesco



MB12-9 Sant'Andrea



Supplementary Fig.2. CL images of the zircon measured in this study with u-Pb ages (2-sigma uncertainties)

Supplementary Table 2: U-Pb isotopic data

Sample	Compositional parameters							Radiogenic Isotope Ratios							Dates (Ma)						
	<u>Th</u>	<u>Th</u>	<u>Pb</u>	<u>Pb*</u>	<u>Pbc</u>	<u>Pbc</u>	²⁰⁶ Pb / ²⁰⁴ Pb	²⁰⁷ Pb / ²⁰⁶ Pb	% err	²⁰⁷ Pb / ²³⁵ U	% err	²⁰⁶ Pb / ²³⁸ U	% err	corr. coef.	²⁰⁷ Pb / ²⁰⁶ Pb	²⁰⁷ Pb / ²³⁵ U	% err	²⁰⁶ Pb / ²³⁸ U	²⁰⁶ Pb / ²³⁴ U	% err	
	<u>U</u>	<u>U</u>	<u>Pb</u>	<u>Pb</u>	(d)	(d)	(e)	(f)	(f)	(g)	(g)	(f)	(g)	(h)	(g)	(h)	(g)	(h)	(g)	(h)	(g)
MB11-6 Sant'Andrea granite (Capanne pluton) - (N 42°80'80.1" / E 10°14'09.1") n=20; as published in Barboni and Schoene (2014)																					
z11	0.21	0.84	1.5	5.90	115	0.067	0.048482	4.560	0.007598	4.735	0.001137	0.261	0.739	122.9	107.41	7.685	0.362	7.240	0.020	7.323	0.019
z9	0.17	0.69	1.8	1.43	136	0.056	0.045340	4.109	0.007142	4.254	0.001143	0.190	0.840	-37.4	99.74	7.227	0.306	7.279	0.015	7.361	0.014
z2	0.16	0.65	1.8	2.04	139	0.053	0.046022	3.863	0.007265	3.994	0.001145	0.170	0.856	-1.2	93.13	7.350	0.292	7.295	0.013	7.376	0.013
z7	0.13	0.53	6.4	0.99	449	0.043	0.046038	1.099	0.007270	1.143	0.001145	0.072	0.708	-0.4	26.50	7.355	0.084	7.297	0.006	7.378	0.005
z15	0.16	0.65	1.4	3.49	113	0.051	0.047116	4.793	0.007453	4.961	0.001147	0.216	0.860	55.1	114.34	7.540	0.373	7.309	0.017	7.392	0.016
z13	0.14	0.57	1.9	3.49	145	0.046	0.046807	3.584	0.007414	3.706	0.001149	0.163	0.850	39.4	85.74	7.500	0.277	7.320	0.013	7.401	0.012
z7_2	0.18	0.73	7.9	1.16	538	0.058	0.046618	0.901	0.007385	0.938	0.001149	0.080	0.543	29.7	21.60	7.471	0.070	7.320	0.006	7.402	0.006
z23	0.28	1.14	2.7	2.97	189	0.090	0.047055	2.642	0.007489	2.754	0.001154	0.141	0.835	52.0	63.07	7.576	0.208	7.354	0.011	7.437	0.010
z3	0.16	0.65	3.2	3.64	233	0.052	0.046744	2.124	0.007441	2.198	0.001155	0.121	0.703	36.2	50.85	7.527	0.165	7.356	0.009	7.438	0.009
z11_2	0.16	0.65	2.4	3.65	175	0.052	0.046846	2.888	0.007482	2.991	0.001158	0.139	0.825	41.4	69.08	7.569	0.226	7.381	0.011	7.463	0.010
z22	0.25	1.02	5.7	2.09	388	0.081	0.046349	1.178	0.007406	1.244	0.001159	0.100	0.710	15.8	28.31	7.492	0.093	7.384	0.008	7.466	0.007
z6	0.12	0.49	3.8	1.21	275	0.039	0.046040	1.854	0.007363	1.914	0.001160	0.092	0.764	-0.3	44.70	7.449	0.142	7.391	0.007	7.473	0.007
z18	0.16	0.67	7.9	2.41	542	0.053	0.046263	0.884	0.007410	0.922	0.001162	0.066	0.647	11.3	21.27	7.496	0.069	7.402	0.005	7.484	0.005
<u>z19</u>	<u>0.07</u>	<u>0.29</u>	<u>5.6</u>	<u>2.62</u>	<u>404</u>	<u>0.023</u>	<u>0.043999</u>	<u>1.465</u>	<u>0.007058</u>	<u>1.471</u>	<u>0.001163</u>	<u>0.137</u>	<u>0.202</u>	<u>-110.7</u>	<u>36.08</u>	<u>7.141</u>	<u>0.105</u>	<u>7.413</u>	<u>0.011</u>	<u>7.495</u>	<u>0.010</u>
z4	0.14	0.57	10.7	1.75	730	0.045	0.046928	0.661	0.007539	0.685	0.001165	0.058	0.517	45.6	15.80	7.626	0.052	7.424	0.004	7.507	0.004
z21	0.24	0.98	8.8	1.75	587	0.077	0.046743	0.802	0.007524	0.836	0.001167	0.066	0.590	36.1	19.20	7.611	0.063	7.439	0.005	7.521	0.005
z16	0.23	0.94	1.3	3.72	101	0.075	0.046618	5.557	0.007533	5.763	0.001172	0.254	0.865	29.7	133.20	7.620	0.438	7.468	0.020	7.551	0.019
z16_2	0.56	2.28	7.2	2.47	446	0.181	0.046765	1.063	0.007574	1.109	0.001175	0.074	0.666	37.3	25.44	7.661	0.085	7.485	0.006	7.568	0.006
z20	0.17	0.70	17.9	1.19	1202	0.056	0.046207	0.407	0.007563	0.439	0.001187	0.063	0.580	8.4	9.79	7.650	0.033	7.566	0.005	7.648	0.005
z17	0.24	0.96	4.6	2.31	319	0.076	0.046835	1.526	0.007892	1.588	0.001222	0.102	0.688	40.8	36.50	7.982	0.126	7.791	0.008	7.873	0.008
MB11-14 San Martino porphyry (N 42°74'65.4" / E 10°25'02.8") n=15; as published in Barboni and Schoene (2014)																					
z23	0.35	1.43	4.6	0.87	309	0.112	0.044224	1.927	0.007038	2.043	0.0011543	0.144	0.830	-98.2	47.34	7.122	0.145	7.354	0.011	7.437	0.011
z18	0.19	0.78	10.6	0.67	715	0.062	0.046483	0.689	0.007410	0.720	0.0011562	0.060	0.597	22.8	16.54	7.497	0.054	7.367	0.005	7.449	0.004
z25	0.38	1.55	8.7	1.58	563	0.122	0.046755	0.969	0.007456	1.012	0.0011566	0.102	0.475	36.7	23.20	7.543	0.076	7.369	0.008	7.452	0.008
z16	0.30	1.18	7.7	1.17	511	0.096	0.046252	0.961	0.007388	1.003	0.0011585	0.071	0.639	10.8	23.12	7.474	0.075	7.382	0.005	7.464	0.005
z17	0.27	1.10	2.2	1.89	161	0.086	0.046485	3.487	0.007462	3.622	0.0011642	0.193	0.750	22.8	83.68	7.549	0.272	7.418	0.015	7.501	0.014
z21	0.16	0.65	9.7	0.60	665	0.052	0.046413	0.797	0.007451	0.838	0.0011643	0.080	0.590	19.1	19.15	7.537	0.063	7.419	0.006	7.501	0.006
z12	0.26	1.05	5.6	0.98	379	0.083	0.045513	1.358	0.007309	1.390	0.0011647	0.086	0.446	-28.1	32.91	7.394	0.102	7.421	0.007	7.504	0.006
z8	0.21	0.85	3.5	2.32	247	0.068	0.047013	2.006	0.007550	2.089	0.0011647	0.113	0.790	49.9	47.90	7.637	0.159	7.421	0.009	7.504	0.008
z14	0.17	0.69	12.3	2.66	830	0.055	0.046555	0.569	0.007482	0.597	0.0011657	0.067	0.498	26.4	13.66	7.569	0.045	7.428	0.005	7.510	0.005
z22	0.29	1.18	18.0	0.94	1166	0.095	0.046696	0.485	0.007506	0.461	0.0011658	0.057	0.517	33.7	10.42	7.593	0.035	7.429	0.004	7.511	0.004
z26	0.32	1.31	7.2	1.44	473	0.105	0.045889	1.175	0.007387	1.213	0.0011676	0.160	0.317	-8.2	28.38	7.473	0.090	7.443	0.007	7.522	0.012
z10	0.29	1.19	5.5	0.97	367	0.094	0.045939	1.414	0.007398	1.474	0.0011681	0.092	0.701	-5.6	34.13	7.485	0.110	7.440	0.012	7.525	0.007
z24	0.31	1.27	11.8	0.87	766	0.101	0.046337	0.688	0.007478	0.722	0.0011705	0.079	0.379	15.2	16.77	7.565	0.054	7.459	0.006	7.541	0.006
z11	0.08	0.31	8.7	1.17	612	0.025	0.046824	0.790	0.007799	0.820	0.001208	0.068	0.592	40.2	18.89	7.888	0.064	7.701	0.006	7.783	0.005
z7	0.04	0.15	9.1	2.14	642	0.012	0.046786	0.747	0.007957	0.761	0.0012335	0.063	0.556	38.3	17.88	8.048	0.061	7.865	0.005	7.947	0.005

Supplementary Table 2: U-Pb isotopic data (cont.)

Sample	Compositional parameters						Radiogenic Isotope Ratios						Dates (Ma)							
	$\frac{\text{Th}}{\text{U}}$		$\frac{\text{Pb}^*}{\text{Pbc}}$		$\frac{\text{Pbc}}{\text{Pb}}$		$\frac{\text{Th}}{\text{U}}$		$\frac{\text{Pb}^*}{\text{Pb}}$		$\frac{\text{Pb}}{\text{Pb}}$		$\frac{\text{Th}}{\text{U}}$		$\frac{\text{Pb}^*}{\text{Pb}}$		$\frac{\text{Pb}}{\text{Pb}}$			
	(b)	(c)	(d)	(e)	(f)	(g)	(h)	(i)	(j)	(k)	(l)	(m)	(n)	(o)	(p)	(q)	(r)	(s)	(t)	
MB11-1	San Piero granite (Capanne pluton) - (N 42°7'46.7" / E 10°20'88.5") n=16																			
z17	0.19	0.78	18.1	0.52	1208	0.063	0.046512	0.445	0.006972	0.488	0.0010879	0.064	0.459	24.3	10.68	7.059	0.033	6.927	0.005	7.009
z22	0.16	0.67	1.3	1.87	105	0.053	0.046180	5.490	0.006935	5.693	0.0010919	0.053	0.857	7.0	132.15	7.023	0.398	6.940	0.019	7.022
z10	0.22	0.90	6.2	0.83	423	0.072	0.045444	1.280	0.006837	1.336	0.0010973	0.084	0.641	-31.8	31.04	6.923	0.092	6.953	0.006	7.035
z5	0.14	0.57	2.3	0.95	174	0.045	0.046070	3.341	0.006965	3.451	0.0010973	0.163	0.756	1.3	80.50	7.053	0.242	6.987	0.012	7.070
z8	0.27	1.09	6.7	1.70	452	0.087	0.046787	1.055	0.007114	1.109	0.0011035	0.074	0.659	38.4	25.26	7.203	0.079	7.027	0.005	7.110
z11	0.19	0.78	4.7	0.81	329	0.060	0.046196	1.613	0.007106	1.682	0.0011164	0.093	0.744	7.8	38.81	7.194	0.120	7.109	0.007	7.192
z9	0.23	0.94	18.8	1.79	1238	0.075	0.046454	0.398	0.007157	0.444	0.0011182	0.066	0.484	21.2	9.55	7.246	0.031	7.122	0.005	7.204
z7	0.16	0.65	33.2	2.45	2221	0.052	0.046603	0.245	0.007311	0.320	0.0011385	0.111	0.604	28.9	5.87	7.401	0.022	7.253	0.008	7.335
z1	0.20	0.83	1.8	2.57	136	0.066	0.046727	3.869	0.007333	4.012	0.0011389	0.179	0.840	35.3	92.64	7.423	0.296	7.256	0.014	7.338
z4	0.16	0.65	14.0	1.68	945	0.052	0.046675	0.503	0.007337	0.545	0.0011408	0.064	0.507	32.6	12.05	7.427	0.039	7.268	0.005	7.350
z13	0.13	0.53	3.1	3.60	228	0.043	0.047016	2.166	0.007428	2.247	0.0011465	0.111	0.789	50.1	51.73	7.519	0.168	7.305	0.009	7.387
z16	0.24	0.98	16.6	0.56	1092	0.077	0.046453	0.451	0.007424	0.494	0.0011599	0.063	0.481	21.2	10.84	7.515	0.036	7.390	0.005	7.473
z14	0.28	1.14	4.7	0.81	318	0.092	0.046708	1.872	0.007511	1.949	0.0011669	0.136	0.591	34.3	44.82	7.602	0.147	7.436	0.011	7.518
z15	0.27	1.10	19.2	0.63	1254	0.087	0.046451	0.437	0.007489	0.478	0.001170	0.067	0.436	21.1	10.51	7.580	0.035	7.455	0.005	7.538
Σz	0.34	1.39	15.4	0.76	987	0.112	0.046317	0.513	0.007746	0.557	0.0012137	0.063	0.537	14.1	12.34	7.840	0.042	7.737	0.005	7.819
z12	0.11	0.45	17.5	0.78	1176	0.034	0.068451	0.287	0.017678	0.321	0.0018736	0.059	0.591	882.2	5.95	17.798	0.056	11.983	0.007	12.067
MB11-2	San Piero granite (Capanne pluton) - (N 42°7'46.7" / E 10°20'07.6") n=22																			
z7	0.38	1.53	8.6	1.83	312	0.122	0.046548	1.600	0.006975	1.700	0.001088	0.110	0.712	26.0	39.0	7.060	0.120	6.925	0.008	7.007
z25	0.14	0.57	1.5	1.17	102	0.046	0.046467	5.800	0.006995	6.000	0.001093	0.260	0.864	21.0	140.00	7.080	0.420	6.960	0.020	7.042
z26	0.09	0.37	12.8	0.95	935	0.029	0.046383	0.570	0.007012	0.610	0.001098	0.061	0.463	16.0	14.00	7.099	0.042	6.989	0.004	7.072
z21	0.1	0.41	17.6	1.13	1077	0.032	0.046684	0.490	0.007084	0.540	0.001102	0.082	0.520	32.0	12.00	7.172	0.038	7.016	0.006	7.099
z3	0.22	0.9	9.2	1.67	378	0.071	0.046905	1.300	0.007165	1.300	0.001109	0.085	0.643	44.0	31.00	7.254	0.096	7.060	0.006	7.143
z12	0.14	0.57	30.3	0.63	3230	0.045	0.046583	0.180	0.007129	0.250	0.001111	0.075	0.608	27.9	4.30	7.218	0.015	7.074	0.005	7.156
z2	0.25	1.02	8.5	1.82	321	0.081	0.046803	1.500	0.007167	1.600	0.001111	0.099	0.686	39.0	36.00	7.260	0.110	7.078	0.007	7.160
z8	0.19	0.76	31.6	2.05	1030	0.06	0.046386	0.460	0.007114	0.510	0.001113	0.069	0.550	18.0	11.00	7.203	0.036	7.089	0.005	7.171
z17	0.15	0.61	16.4	0.76	1451	0.049	0.046639	0.340	0.007155	0.380	0.001113	0.057	0.482	30.8	8.10	7.244	0.026	7.092	0.004	7.174
z10	0.2	0.82	13.8	0.58	1583	0.064	0.046658	0.320	0.007189	0.370	0.001118	0.058	0.494	31.8	7.80	7.278	0.025	7.122	0.004	7.204
z16	0.18	0.73	24.0	0.77	2081	0.059	0.046532	0.280	0.00717	0.350	0.001118	0.069	0.771	25.3	6.60	7.259	0.024	7.123	0.005	7.205
z22	0.14	0.57	16.0	0.90	1200	0.044	0.046801	0.400	0.007237	0.440	0.001122	0.060	0.499	39.1	9.60	7.326	0.031	7.147	0.004	7.230
z24	0.18	0.73	14.3	0.91	1056	0.057	0.046403	0.460	0.007189	0.500	0.001125	0.061	0.485	18.0	11.00	7.278	0.035	7.164	0.005	7.247
z14	0.13	0.53	17.3	0.8	1458	0.043	0.046327	0.380	0.007199	0.430	0.001128	0.066	0.525	14.6	9.10	7.288	0.029	7.184	0.005	7.266
z23	0.16	0.65	8.4	0.58	980	0.052	0.046554	0.540	0.007235	0.590	0.001128	0.060	0.520	25.0	13.00	7.325	0.042	7.188	0.005	7.270
z5	0.16	0.67	19.7	2.52	535	0.053	0.046903	0.880	0.007334	0.930	0.001135	0.074	0.637	44.0	21.00	7.424	0.068	7.228	0.006	7.311
z20	0.18	0.73	24.8	1.10	1511	0.057	0.046665	0.350	0.007296	0.400	0.001135	0.080	0.480	31.0	8.40	7.386	0.028	7.231	0.006	7.314
z4	0.16	0.65	24.4	0.87	1872	0.051	0.046593	0.270	0.007302	0.320	0.001137	0.061	0.477	28.4	6.40	7.392	0.021	7.245	0.005	7.328
z19	0.19	0.78	7.3	1.73	298	0.06	0.046508	1.700	0.007335	1.800	0.001145	0.110	0.683	23.0	42.00	7.430	0.130	7.295	0.009	7.378
z13	0.13	0.49	18.5	0.47	2634	0.041	0.046713	0.210	0.007404	0.270	0.001115	0.062	0.544	34.6	5.00	7.495	0.018	7.330	0.005	7.411
z1	0.13	0.53	6.7	1.29	363	0.042	0.046709	1.300	0.007713	1.400	0.001198	0.080	0.715	34.0	32.00	7.810	0.110	7.638	0.007	7.720
z6	0.24	0.97	17.2	1.16	979	0.077	0.05307	0.430	0.014471	0.470	0.001978	0.064	0.497	331.8	9.90	14.593	0.067	12.658	0.008	12.740

Supplementary Table 2: U-Pb isotopic data (cont.)

Sample	Compositional parameters							Radiogenic Isotope Ratios							Dates (Ma)							
	Th _U	Th _U	Pb [*] Pbc (pg)	Pbc 206Pb	208Pb 206Pb	207Pb 206Pb	% err	206Pb 235U	% err	206Pb 238U	% err	corr. coef.	207Pb 206Pb	207Pb 235U	206Pb 238U	±	206Pb 238U	±	206Pb 238U	±	206Pb 238U	±
(a)	(b)	(c)	(d)	(e)	(f)	(g)	(f)	(g)	(f)	(g)	(h)	(g)	(h)	(g)	(i)	(g)	(h)	(g)	(h)	(g)	(h)	(g)
MB11-5	Orano Dykes (N 42°7'589.8"E 10°29'68.2") n=26																					
z24	0.19	0.73	7.6	0.93	519	0.060	0.0466667	0.964	0.007063	1.010	0.001099	0.669	0.608	31.1	23.11	7.151	0.071	6.998	0.005	7.080	0.005	
z22	0.11	0.45	22.9	1.46	1562	0.036	0.046652	0.326	0.007069	0.378	0.001100	0.088	0.455	31.5	7.83	7.157	0.025	7.002	0.006	7.085	0.006	
z8	0.31	0.22	1.8	1.68	133	0.099	0.047198	4.064	0.007240	4.157	0.001113	0.189	0.847	59.3	96.86	7.329	0.303	7.217	0.014	7.172	0.014	
z23	0.30	1.22	2.2	0.87	158	0.097	0.041980	4.060	0.006472	4.221	0.001119	0.195	0.834	-228.8	102.31	6.555	0.275	7.130	0.015	7.212	0.014	
z18	0.33	1.35	3.0	0.72	211	0.108	0.045500	2.808	0.007084	2.933	0.001130	0.157	0.799	-29.9	68.07	7.173	0.209	7.201	0.012	7.284	0.011	
z18	0.35	1.43	2.6	1.63	183	0.112	0.045646	3.051	0.007122	3.178	0.001133	0.157	0.811	-22.1	73.86	7.216	0.228	7.216	0.012	7.299	0.011	
z29	0.35	1.43	2.6	1.63	183	0.112	0.045646	3.051	0.007122	3.178	0.001133	0.157	0.811	-22.1	73.86	7.216	0.012	7.299	0.011			
z6	0.27	1.41	4.9	1.30	332	0.088	0.045199	1.522	0.007063	1.591	0.001134	0.092	0.711	-44.9	37.02	7.151	0.113	7.219	0.007	7.307	0.007	
z21	0.26	1.06	3.0	0.99	215	0.084	0.043481	2.895	0.006795	3.002	0.001135	0.140	0.775	-141.1	71.71	6.881	0.206	7.228	0.011	7.311	0.010	
z17	0.21	0.86	4.8	1.03	335	0.069	0.044983	1.643	0.007046	1.713	0.001137	0.105	0.676	-57.7	40.04	7.134	0.121	7.246	0.008	7.328	0.008	
z14	0.14	0.57	11.0	1.21	755	0.045	0.046482	0.687	0.007298	0.727	0.001140	0.070	0.497	21.6	16.50	7.388	0.053	7.262	0.005	7.344	0.005	
z15	0.14	0.57	11.0	0.92	752	0.045	0.046444	0.681	0.007293	0.723	0.001140	0.070	0.511	19.6	16.38	7.383	0.052	7.263	0.005	7.345	0.005	
z16	0.35	1.43	9.0	1.30	586	0.113	0.046772	0.869	0.007349	0.925	0.001141	0.093	0.557	36.5	20.81	7.439	0.068	7.268	0.007	7.350	0.007	
z1b	0.27	1.08	2.9	3.40	202	0.086	0.047080	2.458	0.007401	2.585	0.001141	0.380	0.409	53.3	58.65	7.492	0.193	7.268	0.028	7.350	0.028	
z20	0.28	1.14	7.5	0.93	503	0.089	0.045566	1.036	0.007162	1.088	0.001141	0.074	0.638	-26.4	25.11	7.250	0.078	7.269	0.006	7.352	0.005	
z22	0.11	0.45	23.6	0.84	1608	0.034	0.046539	0.317	0.007318	0.363	0.001142	0.055	0.500	24.6	7.64	7.408	0.025	7.272	0.004	7.355	0.004	
z1t	0.20	0.81	5.4	3.75	375	0.064	0.046746	1.276	0.007360	1.333	0.001143	0.084	0.669	36.3	30.55	7.450	0.098	7.279	0.006	7.361	0.006	
z10	0.16	0.72	1.2	1.13	97	0.051	0.040770	6.951	0.006421	7.180	0.001143	0.281	0.856	-302.0	177.73	6.504	0.465	7.280	0.022	7.365	0.021	
z5	0.24	1.11	4.1	1.68	286	0.078	0.045511	1.819	0.007170	1.897	0.001143	0.108	0.722	-28.2	44.09	7.259	0.137	7.281	0.008	7.366	0.008	
z26	0.14	0.57	15.9	0.53	1081	0.044	0.046567	0.480	0.007337	0.527	0.001144	0.086	0.452	26.0	11.54	7.427	0.038	7.287	0.006	7.370	0.006	
z11	0.18	2.80	4.0	3.37	283	0.057	0.046795	1.715	0.007376	1.791	0.001144	0.104	0.703	38.8	41.04	7.467	0.133	7.268	0.008	7.370	0.008	
z3	0.25	1.04	2.7	3.12	192	0.082	0.046490	2.726	0.007387	2.828	0.001153	0.155	0.687	23.1	65.42	7.477	0.210	7.347	0.012	7.429	0.012	
z25	0.05	0.20	6.0	1.03	431	0.016	0.046083	1.193	0.007359	1.233	0.001159	0.077	0.701	0.9	28.77	7.449	0.091	7.389	0.006	7.470	0.006	
z19	0.20	0.82	11.7	0.96	788	0.064	0.045868	0.633	0.007333	0.676	0.001161	0.067	0.524	-10.4	15.30	7.424	0.049	7.396	0.005	7.479	0.005	
z22	0.17	0.69	4.3	1.46	304	0.057	0.046201	1.661	0.007411	1.729	0.001165	0.094	0.740	7.0	39.99	7.502	0.129	7.422	0.007	7.503	0.007	
z9	0.05	0.64	14.2	1.99	994	0.018	0.046247	0.489	0.007645	0.531	0.001200	0.066	0.510	10.5	11.77	7.738	0.040	7.629	0.005	7.729	0.005	
z28	0.39	1.59	3.7	1.07	249	0.125	0.045977	2.084	0.007772	2.173	0.001227	0.115	0.766	-4.7	50.28	7.865	0.170	7.824	0.009	7.906	0.009	
MB11-11	Portoferraio Porphyry (N 42°49'21.6"E 10°17'13.6") n=14																					
z11	0.49	2.00	7.7	1.05	482	0.160	0.0450387	1.134	0.007647	1.177	0.001233	0.095	0.425	-29.4	7.740	0.090	7.860	0.008	7.942	0.008		
z19	0.63	2.57	6.3	2.30	387	0.204	0.045738	1.533	0.007787	1.607	0.001236	0.113	0.642	7.8	36.84	7.881	0.126	7.881	0.009	7.963	0.009	
z16	0.33	1.35	3.6	0.69	245	0.106	0.0445817	2.427	0.007604	2.522	0.001238	0.132	0.720	-54.1	58.96	7.697	0.193	7.896	0.011	7.978	0.011	
z13	0.22	0.90	1.6	1.47	122	0.070	0.0478542	4.572	0.008179	4.754	0.001241	0.223	0.849	115.6	107.31	8.276	0.391	7.911	0.019	7.994	0.018	
z7	0.38	1.55	11.7	0.52	748	0.122	0.0465837	0.652	0.007963	0.687	0.001241	0.054	0.509	51.7	15.54	8.059	0.054	7.913	0.004	7.996	0.004	
z22	0.15	0.57	17.5	0.78	1183	0.047	0.0464617	0.495	0.007944	0.534	0.001241	0.049	0.584	45.1	11.78	8.039	0.042	7.916	0.004	7.997	0.004	
z18	0.14	0.57	7.0	1.14	483	0.046	0.0449932	1.085	0.007694	1.139	0.001242	0.068	0.757	-32.2	26.14	7.787	0.088	7.917	0.006	7.999	0.005	
z8	0.28	1.14	7.1	1.59	474	0.092	0.0464122	1.035	0.007937	1.084	0.001242	0.068	0.658	42.7	24.67	8.032	0.086	7.917	0.006	7.999	0.005	
z20	0.18	0.73	6.5	1.07	445	0.057	0.0462939	1.164	0.007918	1.194	0.001242	0.061	0.489	36.8	8.013	0.095	7.917	0.005	7.996	0.005		
z15	0.18	0.73	6.3	1.04	436	0.059	0.0466768	1.178	0.007985	1.220	0.001242	0.066	0.615	56.3	27.96	8.080	0.098	7.919	0.006	8.001	0.005	
z2	0.22	0.90	8.5	0.92	570	0.072	0.046565	0.855	0.007970	0.896	0.001243	0.061	0.595	50.5	20.34	8.066	0.071	7.924	0.005	8.006	0.005	

Supplementary Table 2: U-Pb isotopic data (cont.)

Sample	Compositional parameters							Radiogenic Isotope Ratios							Dates (Ma)							
	$\frac{\text{Th}}{\text{U}}$	$\frac{\text{Th}}{\text{Pb}}$	$\frac{\text{Pb}^*}{\text{Pbc}}$	$\frac{\text{Pbc}}{(\text{pg})}$	$\frac{\text{Pb}}{\text{Pb}}$																	
(a)	(b)	(c)	(d)	(e)	(f)	(g)	(h)	(i)	(j)	(k)	(l)	(m)	(n)	(o)	(p)	(q)	(r)	(s)	(t)	(u)	(v)	(w)
MB11-11 Portoferraio Porphyry (N 42°49'21.6"E 10°17'13.6") (cont.)																						
z21	0.17	0.69	5.3	1.23	370	0.055	0.0461816	1.386	0.007907	1.444	0.001243	0.083	0.705	30.8	33.04	8.002	0.115	7.926	0.007	8.008	0.007	8.008
z1	0.19	0.78	3.4	3.34	243	0.062	0.0464509	2.024	0.007957	2.104	0.001243	0.146	0.596	45.8	48.12	8.052	0.168	7.927	0.012	8.009	0.012	8.009
z3	0.37	1.51	8.4	2.77	543	0.119	0.0494844	0.814	0.017911	0.851	0.002627	0.054	0.657	181.2	18.96	18.030	0.152	16.830	0.009	16.913	0.009	16.913
MB12-4 San Francesco granite (Cappane pluton) - (N 42°77'09.5"E 10°16'89.5") n=27																						
z1	0.16	0.66	5.3	4.27	369	0.053	0.046504	1.319	0.007127	1.378	0.001112	0.100	0.610	51.4	31.26	7.216	0.099	7.084	0.007	7.166	0.007	7.166
z28	0.18	0.73	4.3	1.89	300	0.058	0.046940	1.619	0.007284	1.688	0.001127	0.097	0.722	72.2	38.27	7.374	0.124	7.176	0.007	7.259	0.007	7.259
z36	0.09	0.37	8.3	0.73	581	0.030	0.046585	0.865	0.007242	0.899	0.001129	0.065	0.514	54.0	20.42	7.382	0.065	7.191	0.005	7.272	0.005	7.272
z38	0.21	0.86	5.9	0.95	403	0.069	0.046002	1.334	0.007156	1.399	0.001129	0.102	0.625	24.0	31.86	7.244	0.100	7.194	0.008	7.276	0.007	7.276
⁻¹⁴ z32	0.14	0.57	5.8	1.07	403	0.046	0.045232	1.271	0.007045	1.329	0.001131	0.080	0.711	-16.8	30.52	7.133	0.094	7.204	0.006	7.286	0.006	7.286
z27	0.14	0.57	2.0	1.32	149	0.046	0.045860	3.815	0.007151	3.957	0.001132	0.188	0.821	17.4	90.97	7.240	0.285	7.209	0.015	7.291	0.014	7.291
z37	0.10	0.41	6.5	1.08	460	0.034	0.046898	1.082	0.007310	1.126	0.001132	0.079	0.599	69.8	25.47	7.400	0.082	7.210	0.006	7.291	0.006	7.291
z39	0.10	0.41	7.8	0.87	547	0.033	0.046441	0.947	0.007241	0.988	0.001132	0.078	0.537	46.7	22.41	7.331	0.072	7.212	0.006	7.294	0.006	7.294
z35	0.13	0.53	13.4	0.46	916.5	0.043	0.046318	0.614	0.007256	0.656	0.001137	0.065	0.534	40.1	14.58	7.346	0.047	7.246	0.005	7.328	0.005	7.328
z21	0.22	0.90	5.6	0.55	386.7	0.070	0.046616	1.332	0.007316	1.394	0.001139	0.093	0.662	56.8	31.60	7.406	0.102	7.255	0.007	7.338	0.007	7.338
z26	0.19	0.78	11.6	1.14	783.7	0.062	0.046482	0.683	0.007295	0.726	0.001139	0.071	0.515	49.7	16.23	7.385	0.053	7.256	0.005	7.338	0.005	7.338
z9	0.19	0.78	7.8	1.49	533.9	0.062	0.046629	0.907	0.007333	0.956	0.001141	0.088	0.527	57.2	21.51	7.423	0.070	7.271	0.007	7.353	0.006	7.353
z11	0.18	0.73	1.7	1.53	128.9	0.058	0.046990	4.128	0.007391	4.284	0.001141	0.196	0.844	75.6	97.49	7.481	0.319	7.272	0.015	7.354	0.014	7.354
z24	0.21	0.86	3.6	0.40	253.7	0.069	0.046402	2.118	0.007302	2.205	0.001142	0.117	0.764	45.4	50.35	7.392	0.162	7.276	0.009	7.358	0.009	7.358
z29	0.12	0.49	5.3	2.38	376.9	0.039	0.046791	1.285	0.007390	1.339	0.001147	0.080	0.701	64.3	30.35	7.481	0.099	7.305	0.006	7.388	0.006	7.388
z23	0.23	0.94	7.1	0.47	477.7	0.075	0.046253	1.164	0.007309	1.223	0.001147	0.088	0.644	37.7	27.73	7.399	0.090	7.306	0.007	7.388	0.006	7.388
z22	0.30	1.22	21.8	0.48	1404	0.098	0.046526	0.404	0.007364	0.440	0.001149	0.060	0.371	51.6	9.61	7.455	0.031	7.318	0.004	7.400	0.004	7.400
z25	0.19	0.78	10.2	0.43	691.2	0.063	0.046553	0.800	0.007375	0.839	0.001150	0.071	0.485	53.0	18.99	7.466	0.062	7.326	0.005	7.408	0.005	7.408
z7	0.11	0.43	1.1	1.99	93.77	0.034	0.046630	6.504	0.007390	6.703	0.001150	0.266	0.872	57.0	153.51	7.481	0.499	7.328	0.022	7.410	0.020	7.410
z8	0.22	0.90	3.8	0.89	266.1	0.072	0.046522	1.933	0.007381	2.011	0.001151	0.108	0.736	51.5	45.93	7.471	0.149	7.335	0.008	7.418	0.008	7.418
z19	0.14	0.57	5.8	0.70	405.6	0.045	0.046319	1.292	0.007353	1.317	0.001152	0.065	0.399	41.1	30.70	7.444	0.097	7.340	0.005	7.423	0.005	7.423
z12	0.18	0.73	4.7	2.56	326.9	0.058	0.046939	1.463	0.007467	1.527	0.001155	0.086	0.751	72.6	34.57	7.559	0.115	7.356	0.007	7.438	0.006	7.438
z30	0.18	0.73	8.6	0.85	587.3	0.058	0.046480	0.859	0.007424	0.978	0.001160	0.116	0.954	48.0	20.39	7.515	0.073	7.389	0.009	7.471	0.009	7.471
z34	0.22	0.9	12.7	0.80	845	0.072	0.046838	0.595	0.007573	0.638	0.001174	0.071	0.496	66.0	14.11	7.665	0.048	7.481	0.005	7.563	0.005	7.563
z40	0.16	0.65	8.5	0.82	585.2	0.052	0.046054	1.012	0.007525	1.076	0.001186	0.091	0.681	25.4	24.12	7.617	0.081	7.561	0.007	7.643	0.007	7.643
z31	0.14	0.56	11.0	0.67	748.3	0.046	0.053683	0.640	0.009709	0.708	0.001313	0.077	0.849	378.5	14.30	9.816	0.069	8.377	0.007	8.458	0.007	8.458
z18	0.09	0.37	10.8	0.98	752.2	0.028	0.048976	0.620	0.009761	0.660	0.001446	0.062	0.605	167.7	14.39	9.867	0.064	9.232	0.006	9.316	0.006	9.316

Supplementary Table 2: U-Pb isotopic data (cont.)

Sample	Compositional parameters						Radiogenic Isotope Ratios						Dates (Ma)								
	Th U	Th U	Pbc (pg)	Pbc* Pbc	^{206}Pb ^{206}Pb	^{208}Pb ^{208}Pb	^{207}Pb ^{235}U	% err	^{206}Pb ^{238}U	% err	^{207}Pb ^{235}U	% err	corr. coeff.	^{207}Pb ^{206}Pb	^{206}Pb ^{238}U	\pm	^{206}Pb ^{238}U	\pm	^{206}Pb ^{238}U	\pm	
(a)	(b)	(c)	(d)	(e)	(f)	(g)	(f)	(g)	(f)	(g)	(f)	(g)	(h)	(g)	(i)	(g)	(h)	(g)	(h)	(g)	
MB12-8	San Francesco granite (Cappane pluton) - (N 42°7'6" E 10°18'77.9") n=16																				
z2	0.17	0.67	9.4	1.65	640	0.054	0.045977	0.798	0.007052	0.844	0.001113	0.064	0.633	24.1	19.0	7.140	0.059	7.089	0.005	7.172	0.005
z1	0.19	0.77	6.7	2.69	459	0.062	0.046177	1.064	0.007090	1.111	0.001114	0.064	0.682	34.5	25.3	7.179	0.079	7.097	0.005	7.180	0.005
z21	0.26	1.06	2.4	0.63	176	0.083	0.046673	3.077	0.007204	3.198	0.001121	0.169	0.739	59.0	73.0	7.293	0.232	7.138	0.013	7.220	0.012
z20	0.22	0.90	5.0	0.65	347	0.072	0.045618	1.589	0.007045	1.673	0.001121	0.106	0.774	4.0	38.1	7.133	0.118	7.142	0.008	7.224	0.008
z13	0.26	1.06	5.6	1.33	377	0.085	0.046175	1.526	0.007149	1.598	0.001124	0.112	0.642	34.2	36.4	7.238	0.115	7.157	0.008	7.239	0.008
z10	0.11	0.45	11.7	0.93	807	0.036	0.046767	0.656	0.007258	0.693	0.001126	0.072	0.449	64.7	15.5	7.348	0.050	7.174	0.005	7.257	0.005
z16	0.14	0.57	6.9	0.86	476	0.045	0.046607	1.029	0.007237	1.071	0.001127	0.059	0.683	56.5	24.4	7.327	0.078	7.178	0.004	7.260	0.004
z22	0.13	0.53	25.1	0.63	1699	0.044	0.046632	0.302	0.007251	0.341	0.001129	0.046	0.395	56.2	7.2	7.341	0.023	7.193	0.003	7.274	0.003
z14	0.13	0.53	15.4	0.40	1052	0.041	0.046609	0.512	0.007254	0.539	0.001129	0.047	0.358	56.7	12.1	7.344	0.038	7.194	0.003	7.277	0.003
z11	0.14	0.57	7.9	0.82	546	0.046	0.046558	0.954	0.007269	1.001	0.001133	0.079	0.584	53.7	22.6	7.359	0.073	7.218	0.006	7.300	0.006
z4	0.17	0.68	4.9	1.28	343.2	0.0541	0.0465217	1.444	0.007270	1.501	0.001134	0.086	0.678	51.9	34.3	7.360	0.110	7.224	0.007	7.307	0.006
z24	0.22	0.90	20.4	0.53	1348	0.0711	0.0466782	0.389	0.007297	0.428	0.001134	0.060	0.420	59.9	9.2	7.387	0.030	7.226	0.004	7.309	0.004
z15	0.22	0.90	9.3	0.99	621.8	0.0717	0.0464455	0.772	0.007298	0.811	0.001140	0.053	0.613	47.8	18.4	7.388	0.059	7.264	0.004	7.347	0.004
z5	0.17	0.65	7.0	0.63	482.1	0.0535	0.0462571	1.095	0.007284	1.142	0.001143	0.065	0.685	37.7	26.0	7.374	0.083	7.281	0.005	7.363	0.005
z18	0.10	0.41	19.6	0.73	1345	0.0327	0.0465314	0.375	0.007368	0.407	0.001149	0.038	0.429	52.0	8.9	7.459	0.029	7.322	0.003	7.404	0.003
Σz_{19}	0.22	0.90	0.9	1.43	76	0.0719	0.0461928	8.111	0.007619	8.413	0.001197	0.358	0.879	32.3	193.4	7.711	0.646	7.633	0.029	7.715	0.028
MB12-9	San Francesco granite (Cappane pluton) - (N 42°7'6" E 10°18'77.9") n=12																				
z12	0.21	0.82	18.7	0.61	1240	0.0684	0.046551	0.419	0.007204	0.465	0.001123	0.070	0.478	53.2	10.0	7.294	0.032	7.155	0.005	7.236	0.005
z13	0.23	0.94	2.5	2.72	184	0.0751	0.046815	2.735	0.007257	2.843	0.001125	0.133	0.835	67.0	64.8	7.346	0.208	7.166	0.010	7.248	0.010
z16	0.30	1.22	3.0	0.49	208.9	0.0983	0.045715	2.663	0.007114	2.775	0.001130	0.140	0.801	8.8	63.9	7.202	0.199	7.197	0.011	7.279	0.010
z18	0.21	0.86	4.8	1.19	334.2	0.0673	0.046972	1.464	0.007313	1.528	0.001130	0.086	0.734	74.0	34.6	7.403	0.112	7.200	0.006	7.282	0.006
z5	0.16	0.67	18.0	1.37	1209	0.053	0.046247	0.407	0.007203	0.466	0.001130	0.099	0.520	37.9	9.7	7.293	0.033	7.200	0.007	7.283	0.007
z6	0.11	0.44	3.0	3.72	218.3	0.0347	0.045296	2.699	0.007060	2.798	0.001131	0.151	0.739	-12.1	64.6	7.148	0.199	7.205	0.012	7.288	0.011
z3	0.09	0.38	19.3	1.65	1324	0.0305	0.046560	0.386	0.007298	0.442	0.001137	0.072	0.609	53.7	9.1	7.388	0.031	7.247	0.005	7.329	0.005
z4	0.17	0.70	11.2	1.54	756.3	0.0554	0.046360	0.689	0.007293	0.738	0.001142	0.073	0.585	43.4	16.4	7.383	0.053	7.273	0.005	7.355	0.005
z19	0.16	0.85	10.4	1.07	706.3	0.0526	0.046598	0.707	0.007332	0.741	0.001142	0.058	0.484	54.3	16.8	7.422	0.054	7.278	0.004	7.360	0.004
z1	0.14	0.55	8.4	2.55	579.7	0.0441	0.046106	0.859	0.007292	0.908	0.001148	0.098	0.503	30.0	20.4	7.382	0.066	7.313	0.007	7.395	0.007
z14	0.30	1.22	9.3	0.63	607.4	0.0976	0.046740	0.855	0.007397	0.901	0.001149	0.079	0.525	61.6	20.3	7.488	0.067	7.321	0.006	7.403	0.006
Σz_{15}	0.13	0.53	19.1	0.69	1298	0.0422	0.046593	0.387	0.007376	0.433	0.001149	0.061	0.518	54.1	9.2	7.467	0.031	7.323	0.005	7.406	0.005

(a) z1, z2 etc. are labels for single zircon grains or fragment of grain; all zircons annealed and chemically abraded after Mattinson (2005).

(b) Model Th/U ratio calculated from radiogenic 208Pb/206Pb ratio and 207Pb/235U age

(c) Th/U melt was calculated using the model Th/U zircon of (b) and k'ds from Rubatto and Herman (2007)

(d) Pb* and Pbc represent radiogenic and common Pb, respectively

(e) Measured ratio corrected for spike and fractionation only

(f) Corrected for fractionation, spike and common Pb, which was assumed to be blank: 206Pb/204Pb = 18.50±0.10; 207Pb/204Pb = 15.56±0.21; 208Pb/204Pb = 37.48±0.34 (2-sigma standard deviation)

(g) Errors are 2-sigma, propagated using the algorithm of McLean et al., (2011) and Crowley et al., (2007)

(h) Calculations are based on the decay constants of Jaffey et al., (1971). 206Pb/238U and 207Pb/206Pb ages corrected for initial disequilibrium in 230Th/238U

(i) Raw 206Pb/238U ages before correction for initial disequilibrium in 230Th/238U

Supplementary Table 2 Rhyolite-MELTS modeling results: melt composition

San Francesco (P = 2.3 Kbar; initial water content = 2 wt%; OPX out; Qz-Fa-Mag buffer)

Temperature (°C)	wt% SiO ₂ melt	wt% TiO ₂ melt	wt% Al ₂ O ₃ melt	wt% FeO melt	wt% MgO melt	wt% CaO melt	wt% Na ₂ O melt	wt% K ₂ O melt	wt% H ₂ O melt
1006	67.44	0.58	16.03	1.94	1.21	2.51	3.50	4.08	1.99
996	67.50	0.58	16.09	1.88	1.13	2.51	3.51	4.10	2.00
986	67.56	0.58	16.14	1.82	1.05	2.51	3.53	4.11	2.01
976	67.69	0.59	16.12	1.76	0.97	2.48	3.52	4.16	2.03
966	67.99	0.61	15.96	1.70	0.89	2.36	3.45	4.26	2.10
956	68.28	0.62	15.80	1.65	0.82	2.25	3.37	4.37	2.16
946	68.56	0.64	15.64	1.58	0.75	2.15	3.29	4.48	2.22
936	68.82	0.66	15.49	1.52	0.69	2.06	3.20	4.59	2.29
926	69.09	0.68	15.35	1.45	0.64	1.98	3.10	4.69	2.35
916	69.34	0.70	15.21	1.38	0.59	1.91	3.00	4.80	2.42
906	69.58	0.71	15.07	1.31	0.54	1.84	2.89	4.90	2.48
896	69.89	0.68	14.93	1.22	0.50	1.78	2.79	5.00	2.55
886	70.20	0.64	14.80	1.13	0.47	1.72	2.67	5.10	2.62
876	70.49	0.61	14.67	1.04	0.44	1.67	2.56	5.20	2.69
866	70.77	0.57	14.54	0.96	0.41	1.62	2.45	5.30	2.76
856	71.05	0.54	14.42	0.88	0.38	1.58	2.33	5.39	2.82
846	71.31	0.51	14.30	0.80	0.36	1.54	2.22	5.47	2.89
836	71.56	0.48	14.18	0.74	0.34	1.50	2.11	5.55	2.95
826	71.80	0.45	14.06	0.67	0.32	1.47	2.00	5.63	3.02
816	72.03	0.43	13.95	0.61	0.30	1.44	1.89	5.70	3.08
806	72.05	0.40	13.93	0.56	0.29	1.41	1.79	5.82	3.18
796	71.84	0.37	14.02	0.51	0.27	1.39	1.71	5.97	3.33
786	71.60	0.34	14.12	0.49	0.27	1.40	1.69	5.91	3.58
776	71.30	0.30	14.22	0.49	0.25	1.41	1.67	5.85	3.85
766	70.93	0.26	14.35	0.53	0.21	1.43	1.66	5.77	4.14
756	70.53	0.22	14.48	0.56	0.18	1.45	1.65	5.68	4.46
746	70.02	0.19	14.70	0.57	0.16	1.49	1.63	5.59	4.78
736	69.54	0.17	14.89	0.55	0.14	1.51	1.63	5.49	5.16
726	68.08	0.16	16.28	0.50	0.13	1.68	1.29	5.44	5.18
716	65.94	0.15	16.85	0.42	0.12	2.58	1.12	5.25	5.28
706	64.78	0.16	17.93	0.33	0.11	2.73	0.94	5.13	5.34
696	63.63	0.15	18.86	0.27	0.10	2.94	0.81	4.99	5.41
686	62.44	0.15	19.69	0.22	0.09	3.21	0.71	4.84	5.49
676	58.24	0.13	19.39	0.23	0.09	4.67	0.70	4.18	6.33

Supplementary Table 2 Rhyolite-MELTS modeling results: melt composition

Sant'Andrea (P = 2.3 Kbar; initial water content = 2 wt%; OPX out; Qz-Fa-Mag buffer)

Temperature (°C)	wt% SiO ₂ melt	wt% TiO ₂ melt	wt% Al ₂ O ₃ melt	wt% FeO melt	wt% MgO melt	wt% CaO melt	wt% Na ₂ O melt	wt% K ₂ O melt	wt% H ₂ O melt
968	69.08	0.39	15.89	1.68	0.85	2.20	3.09	4.25	1.99
958	69.25	0.39	15.85	1.62	0.79	2.15	3.06	4.31	2.02
948	69.55	0.40	15.69	1.56	0.72	2.04	2.98	4.41	2.08
938	69.85	0.41	15.55	1.50	0.66	1.94	2.90	4.51	2.13
928	70.13	0.42	15.40	1.43	0.61	1.85	2.80	4.61	2.19
918	70.41	0.44	15.26	1.37	0.56	1.77	2.71	4.70	2.24
908	70.67	0.45	15.13	1.30	0.51	1.69	2.61	4.80	2.30
898	70.93	0.46	15.00	1.22	0.47	1.63	2.51	4.89	2.36
888	71.19	0.47	14.88	1.15	0.44	1.56	2.40	4.98	2.41
878	71.43	0.48	14.75	1.08	0.40	1.51	2.29	5.07	2.47
868	71.67	0.49	14.64	1.01	0.37	1.45	2.19	5.16	2.53
858	71.90	0.50	14.52	0.94	0.35	1.40	2.08	5.24	2.58
848	72.13	0.51	14.41	0.87	0.32	1.36	1.97	5.32	2.64
838	72.39	0.49	14.30	0.79	0.30	1.32	1.86	5.40	2.69
828	72.23	0.45	14.40	0.73	0.29	1.27	1.77	5.58	2.81
818	72.05	0.42	14.51	0.67	0.27	1.24	1.68	5.77	2.93
808	71.86	0.40	14.62	0.62	0.26	1.20	1.59	5.94	3.05
798	71.65	0.37	14.75	0.57	0.25	1.18	1.52	6.05	3.21
788	71.40	0.34	14.89	0.54	0.24	1.17	1.49	6.01	3.44
778	71.14	0.31	15.05	0.51	0.23	1.17	1.46	5.95	3.69
768	70.82	0.27	15.22	0.51	0.22	1.17	1.43	5.88	3.96
758	70.43	0.23	15.43	0.54	0.19	1.16	1.41	5.80	4.24
748	70.01	0.20	15.66	0.56	0.16	1.16	1.39	5.71	4.55
738	69.48	0.18	16.05	0.53	0.14	1.16	1.34	5.62	4.84
728	68.86	0.17	16.56	0.50	0.13	1.16	1.27	5.53	5.12
718	67.44	0.16	17.61	0.41	0.12	1.49	1.07	5.41	5.16
708	66.37	0.17	18.69	0.32	0.11	1.62	0.90	5.30	5.19
698	65.37	0.16	19.66	0.26	0.10	1.76	0.78	5.18	5.24
688	64.04	0.16	20.33	0.21	0.09	2.19	0.68	5.02	5.31

Supplementary Table 2 Rhyolite-MELTS modeling results: melt composition

San Piero (P = 2.3 Kbar; initial water content = 2 wt%; OPX out; Qz-Fa-Mag buffer)

Temperature (°C)	wt% SiO ₂ melt	wt% TiO ₂ melt	wt% Al ₂ O ₃ melt	wt% FeO melt	wt% MgO melt	wt% CaO melt	wt% Na ₂ O melt	wt% K ₂ O melt	wt% H ₂ O melt
1076	68.21	0.58	14.87	2.81	1.72	1.95	2.23	4.84	2.01
1066	68.29	0.58	14.94	2.73	1.60	1.96	2.24	4.86	2.02
1056	68.37	0.59	15.01	2.65	1.49	1.96	2.25	4.88	2.03
1046	68.45	0.59	15.07	2.57	1.39	1.97	2.26	4.91	2.04
1036	68.53	0.59	15.13	2.49	1.29	1.97	2.27	4.93	2.05
1026	68.61	0.59	15.20	2.40	1.20	1.98	2.28	4.96	2.06
1016	68.69	0.60	15.25	2.31	1.11	1.98	2.29	4.98	2.07
1006	68.77	0.60	15.31	2.22	1.03	1.98	2.30	5.00	2.08
996	68.85	0.60	15.37	2.12	0.96	1.98	2.31	5.02	2.08
986	68.93	0.60	15.42	2.03	0.89	1.98	2.32	5.05	2.09
976	69.01	0.61	15.48	1.93	0.83	1.98	2.33	5.07	2.10
966	69.09	0.61	15.53	1.83	0.77	1.98	2.34	5.09	2.11
956	69.17	0.61	15.58	1.74	0.71	1.98	2.35	5.11	2.12
946	69.25	0.61	15.63	1.64	0.66	1.97	2.36	5.13	2.13
936	69.33	0.61	15.67	1.54	0.61	1.97	2.37	5.15	2.14
926	69.41	0.62	15.72	1.45	0.57	1.96	2.38	5.17	2.14
916	69.62	0.63	15.65	1.36	0.53	1.90	2.32	5.24	2.18
906	69.89	0.64	15.52	1.27	0.49	1.81	2.24	5.35	2.23
896	70.15	0.65	15.40	1.18	0.45	1.73	2.15	5.45	2.28
886	70.40	0.67	15.28	1.10	0.42	1.65	2.06	5.55	2.33
876	70.68	0.65	15.16	1.01	0.39	1.58	1.96	5.65	2.39
866	70.97	0.61	15.05	0.92	0.37	1.52	1.86	5.75	2.44
856	71.25	0.58	14.94	0.84	0.35	1.46	1.76	5.84	2.49
846	71.51	0.55	14.84	0.77	0.32	1.41	1.67	5.93	2.54
836	71.76	0.52	14.74	0.70	0.31	1.36	1.57	6.01	2.59
826	71.99	0.49	14.64	0.63	0.29	1.31	1.47	6.09	2.63
816	71.84	0.46	14.74	0.58	0.27	1.27	1.38	6.27	2.74
806	71.63	0.42	14.88	0.54	0.27	1.27	1.33	6.25	2.94
796	71.41	0.39	15.02	0.51	0.26	1.27	1.29	6.21	3.16
786	71.16	0.36	15.18	0.48	0.25	1.27	1.25	6.17	3.38
776	70.89	0.32	15.35	0.46	0.25	1.27	1.22	6.11	3.63
766	70.52	0.28	15.56	0.49	0.21	1.27	1.18	6.04	3.88
756	70.13	0.24	15.79	0.52	0.18	1.26	1.15	5.96	4.15
746	69.70	0.21	16.05	0.54	0.16	1.26	1.12	5.87	4.44
736	69.10	0.19	16.56	0.51	0.14	1.26	1.05	5.78	4.68
726	68.36	0.17	16.47	0.49	0.12	1.52	1.12	5.60	5.10
716	67.03	0.17	17.57	0.38	0.11	1.77	0.92	5.50	5.14
706	65.87	0.17	18.56	0.30	0.11	1.98	0.77	5.37	5.19
696	64.75	0.17	19.46	0.25	0.10	2.18	0.66	5.23	5.25
686	63.54	0.16	20.22	0.20	0.09	2.50	0.58	5.06	5.33
676	58.87	0.13	19.55	0.22	0.09	4.36	0.58	4.34	6.20

Supplementary Table 2 (cont) Rhyolite-MELTS modeling results: modal proportions**San Francesco** (P = 2.3 Kbar; initial water content = 2 wt%; OPX out; Qz-Fa-Mag buffer)

Temperature (°C)	% liquid	% crystal	% Kld	% qz	% plag	% biotite	% ilmnite	% cpx
1006	1.00	0.00	-	-	-	-	-	0.23
996	1.00	0.00	-	-	-	-	-	0.62
986	0.99	0.01	-	-	-	-	-	1.01
976	0.98	0.02	-	-	0.74	-	-	1.44
966	0.95	0.05	-	-	3.12	-	-	1.94
956	0.93	0.07	-	-	5.42	-	-	2.42
946	0.90	0.10	-	-	7.62	-	-	2.85
936	0.87	0.13	-	-	9.74	-	-	3.26
926	0.85	0.15	-	-	11.77	-	-	3.64
916	0.83	0.17	-	-	13.71	-	-	4.00
906	0.81	0.19	-	-	15.56	-	-	4.33
896	0.78	0.22	-	-	17.39	-	0.08	4.59
886	0.76	0.24	-	-	19.13	-	0.17	4.81
876	0.74	0.26	-	-	20.79	-	0.26	5.02
866	0.73	0.27	-	-	22.36	-	0.33	5.20
856	0.71	0.29	-	-	23.84	-	0.40	5.37
846	0.69	0.31	-	-	25.26	-	0.46	5.52
836	0.68	0.32	-	-	26.59	-	0.52	5.66
826	0.66	0.34	-	-	27.86	-	0.57	5.78
816	0.65	0.35	-	-	29.07	-	0.62	5.89
806	0.63	0.37	-	0.55	30.36	-	0.67	5.99
796	0.60	0.40	0.34	1.70	31.56	-	0.72	6.08
786	0.56	0.44	3.10	3.16	31.44	-	0.79	6.15
776	0.51	0.49	5.39	4.90	31.61	0.43	0.87	5.84
766	0.47	0.53	7.25	6.83	31.99	1.23	0.95	5.24
756	0.43	0.57	8.92	8.53	32.33	1.87	1.01	4.75
746	0.38	0.62	9.22	12.65	33.72	4.44	0.63	-
736	0.35	0.65	10.74	13.73	33.85	4.57	0.68	-
726	0.23	0.77	15.79	17.83	35.53	4.68	0.74	-
716	0.10	0.90	22.79	21.31	35.03	3.56	1.18	-
706	0.08	0.92	23.84	22.06	35.33	3.39	1.18	-
696	0.06	0.94	24.43	22.51	35.56	3.28	1.18	-
686	0.05	0.95	24.79	22.81	35.75	3.20	1.18	-
676	0.00	1.00	26.44	24.36	35.74	3.27	1.20	-

Supplementary Table 2 (cont) Rhyolite-MELTS modeling results: modal proportions

Sant'Andrea (P = 2.3 Kbar; initial water content = 2 wt%; OPX out; Qz-Fa-Mag buffer)

Temperature (°C)	% liquid	% crystal	% KId	% qz	% plag	% biotite	% ilmnite	% cpx
968	1.00	0.00	-	-	-	-	-	0.94
958	0.99	0.01	-	-	0.98	-	-	1.34
948	0.96	0.04	-	-	3.16	-	-	1.78
938	0.94	0.06	-	-	5.26	-	-	2.20
928	0.91	0.09	-	-	7.28	-	-	2.59
918	0.89	0.11	-	-	9.21	-	-	2.95
908	0.87	0.13	-	-	11.06	-	-	3.29
898	0.85	0.15	-	-	12.83	-	-	3.61
888	0.83	0.17	-	-	14.52	-	-	3.90
878	0.81	0.19	-	-	16.13	-	-	4.18
868	0.79	0.21	-	-	17.66	-	-	4.43
858	0.78	0.23	-	-	19.12	-	-	4.66
848	0.76	0.24	-	-	20.50	-	-	4.88
838	0.74	0.26	-	-	21.84	-	0.05	5.03
828	0.71	0.29	-	1.29	23.45	-	0.13	5.18
818	0.68	0.32	-	2.53	24.96	-	0.20	5.30
808	0.66	0.35	-	3.70	26.39	-	0.26	5.41
798	0.62	0.38	0.89	4.94	27.29	-	0.33	5.51
788	0.58	0.42	3.60	6.41	27.22	-	0.40	5.58
778	0.54	0.46	6.03	7.77	27.23	-	0.46	5.64
768	0.50	0.50	8.11	9.28	27.40	0.27	0.52	5.48
758	0.46	0.54	9.79	10.99	27.77	0.91	0.58	5.00
748	0.43	0.57	11.32	12.52	28.10	1.45	0.63	4.61
738	0.38	0.62	11.53	16.34	29.34	3.73	0.24	-
728	0.34	0.66	13.63	17.95	29.76	3.84	0.29	-
718	0.18	0.83	21.99	22.39	29.53	2.65	0.75	-
708	0.14	0.86	23.47	23.52	29.98	2.52	0.76	-
698	0.12	0.88	24.38	24.24	30.30	2.43	0.77	-
688	0.00	1.00	25.64	25.32	30.52	2.38	0.78	-

Supplementary Table 2 (cont) Rhyolite-MELTS modeling results: modal proportions

San Piero (P = 2.3 Kbar; initial water content = 2 wt%; OPX out; Qz-Fa-Mag buffer)

Temperature (°C)	% liquid	% crystal	% KId	% qz	% plag	% biotite	% ilmnite	% cpx
1076	1.00	0.00	-	-	-	-	-	0.26
1066	0.99	0.01	-	-	-	-	-	0.78
1056	0.99	0.01	-	-	-	-	-	1.27
1046	0.98	0.02	-	-	-	-	-	1.76
1036	0.98	0.02	-	-	-	-	-	2.23
1026	0.97	0.03	-	-	-	-	-	2.69
1016	0.97	0.03	-	-	-	-	-	3.13
1006	0.96	0.04	-	-	-	-	-	3.57
996	0.96	0.04	-	-	-	-	-	3.99
986	0.96	0.05	-	-	-	-	-	4.40
976	0.95	0.05	-	-	-	-	-	4.80
966	0.95	0.05	-	-	-	-	-	5.19
956	0.94	0.06	-	-	-	-	-	5.57
946	0.94	0.06	-	-	-	-	-	5.93
936	0.94	0.06	-	-	-	-	-	6.29
926	0.93	0.07	-	-	-	-	-	6.63
916	0.92	0.08	-	-	-	-	-	7.00
906	0.90	0.10	-	-	-	-	-	7.36
896	0.88	0.12	-	-	-	-	-	7.70
886	0.86	0.14	-	-	-	-	-	8.00
876	0.84	0.16	-	-	-	-	0.06	8.24
866	0.82	0.18	-	-	-	-	0.14	8.43
856	0.80	0.20	-	-	-	-	0.22	8.60
846	0.79	0.21	-	-	1.20	-	0.29	8.76
836	0.77	0.23	-	-	4.32	-	0.36	8.89
826	0.76	0.24	-	-	7.05	-	0.42	9.02
816	0.73	0.27	0.03	1.20	9.45	-	0.49	9.13
806	0.68	0.32	3.08	2.90	11.58	-	0.59	9.21
796	0.63	0.37	5.80	4.48	13.49	-	0.68	9.29
786	0.59	0.41	8.24	5.95	15.22	-	0.75	9.35
776	0.55	0.45	10.42	7.39	16.58	0.07	0.82	9.35
766	0.50	0.50	11.96	9.63	17.55	1.23	0.91	8.47
756	0.46	0.54	13.35	11.56	18.41	2.17	0.97	7.75
746	0.42	0.58	14.60	13.27	19.06	2.97	1.03	7.15
736	0.37	0.63	14.08	18.53	20.28	6.45	0.42	-
726	0.23	0.77	21.84	21.97	24.53	5.24	1.06	-
716	0.15	0.85	25.46	24.33	26.30	4.76	1.16	-
706	0.12	0.88	26.82	25.38	27.32	4.57	1.16	-
696	0.10	0.90	27.64	26.05	27.96	4.43	1.17	-
686	0.08	0.92	28.33	26.67	30.74	4.34	1.17	-
676	0.00	1.00	31.08	29.32	31.08	4.51	1.20	-

Supplementary Table 2 (cont) Rhyolite-MELTS modeling results: feldspar compositions

San Francesco (P = 2.3 Kbar; initial water content = 2 wt%; OPX out; Qz-Fa-Mag buffer)

Plagioclase

Temperature (°C)	wt% SiO ₂	wt% Al ₂ O ₃	wt% CaO	wt% Na ₂ O	wt% K ₂ O	% ab	% an	% or
976	58.79	26.01	7.74	6.85	0.62	0.59	0.37	0.04
966	59.12	25.77	7.47	6.98	0.66	0.61	0.36	0.04
956	59.44	25.55	7.21	7.10	0.70	0.62	0.35	0.04
946	59.73	25.35	6.97	7.21	0.74	0.62	0.33	0.04
936	60.00	25.16	6.75	7.31	0.78	0.63	0.32	0.04
926	60.24	24.98	6.55	7.40	0.83	0.64	0.31	0.05
916	60.47	24.82	6.37	7.48	0.87	0.65	0.30	0.05
906	60.68	24.67	6.19	7.55	0.91	0.65	0.30	0.05
896	60.86	24.53	6.04	7.61	0.96	0.66	0.29	0.05
886	61.03	24.41	5.90	7.66	1.01	0.66	0.28	0.06
876	61.19	24.29	5.76	7.70	1.05	0.67	0.28	0.06
866	61.33	24.19	5.64	7.74	1.10	0.67	0.27	0.06
856	61.46	24.09	5.53	7.77	1.15	0.67	0.26	0.07
846	61.58	24.00	5.43	7.80	1.20	0.67	0.26	0.07
836	61.69	23.91	5.33	7.82	1.25	0.67	0.25	0.07
826	61.79	23.83	5.25	7.84	1.29	0.68	0.25	0.07
816	61.88	23.76	5.17	7.85	1.34	0.68	0.25	0.08
806	61.95	23.70	5.10	7.84	1.41	0.68	0.24	0.08
796	61.98	23.66	5.06	7.82	1.48	0.67	0.24	0.08
786	61.81	23.80	5.21	7.79	1.39	0.67	0.25	0.08
776	61.65	23.92	5.35	7.77	1.30	0.67	0.26	0.07
766	61.51	24.04	5.48	7.75	1.23	0.67	0.26	0.07
756	61.39	24.13	5.59	7.73	1.16	0.67	0.27	0.07
746	61.25	24.24	5.71	7.71	1.09	0.67	0.27	0.06
736	61.16	24.31	5.79	7.71	1.03	0.67	0.28	0.06
726	61.07	24.39	5.87	7.70	0.98	0.66	0.28	0.06
716	61.21	24.30	5.76	7.78	0.95	0.67	0.27	0.05
706	61.18	24.33	5.80	7.79	0.90	0.67	0.28	0.05
696	61.16	24.35	5.82	7.80	0.86	0.67	0.28	0.05
686	61.15	24.37	5.84	7.82	0.82	0.68	0.28	0.05
676	61.15	24.38	5.84	7.85	0.78	0.68	0.28	0.04

K-feldspar

Temperature (°C)	wt% SiO ₂	wt% Al ₂ O ₃	wt% CaO	wt% Na ₂ O	wt% K ₂ O	% ab	% an	% or
796	65.56	19.08	0.44	3.79	11.13	0.33	0.02	0.64
786	65.55	19.04	0.41	3.66	11.34	0.32	0.02	0.66
776	65.54	19.00	0.39	3.53	11.54	0.31	0.02	0.67
766	65.52	18.97	0.36	3.41	11.73	0.30	0.02	0.68
756	65.51	18.94	0.34	3.30	11.91	0.29	0.02	0.69
746	65.50	18.91	0.31	3.19	12.09	0.28	0.02	0.70
736	65.49	18.88	0.29	3.10	12.24	0.27	0.01	0.71
726	65.48	18.85	0.27	3.00	12.40	0.27	0.01	0.72
716	65.49	18.83	0.25	2.96	12.47	0.26	0.01	0.73
706	65.48	18.81	0.24	2.88	12.60	0.25	0.01	0.73
696	65.47	18.78	0.22	2.80	12.72	0.25	0.01	0.74
686	65.46	18.76	0.21	2.73	12.85	0.24	0.01	0.75
676	65.45	18.74	0.19	2.66	12.96	0.24	0.01	0.76

Supplementary Table 2 (cont) Rhyolite-MELTS modeling results: feldspar compositions

Sant'Andrea (P = 2.3 Kbar; initial water content = 2 wt%; OPX out; Qz-Fa-Mag buffer)

Plagioclase

Temperature (°C)	wt% SiO ₂	wt% Al ₂ O ₃	wt% CaO	wt% Na ₂ O	wt% K ₂ O	% ab	% an	% or
958	59.21	25.71	7.39	7.01	0.67	0.61	0.35	0.04
948	59.52	25.49	7.14	7.13	0.71	0.62	0.34	0.04
938	59.81	25.29	6.91	7.24	0.75	0.63	0.33	0.04
928	60.07	25.10	6.69	7.34	0.80	0.63	0.32	0.05
918	60.32	24.93	6.49	7.43	0.84	0.64	0.31	0.05
908	60.54	24.77	6.31	7.50	0.88	0.65	0.30	0.05
898	60.74	24.62	6.14	7.57	0.92	0.65	0.29	0.05
888	60.93	24.49	5.98	7.63	0.97	0.66	0.29	0.05
878	61.10	24.36	5.84	7.69	1.01	0.66	0.28	0.06
868	61.25	24.25	5.71	7.74	1.05	0.67	0.27	0.06
858	61.40	24.14	5.59	7.78	1.09	0.67	0.27	0.06
848	61.52	24.05	5.48	7.81	1.14	0.67	0.26	0.06
838	61.64	23.96	5.39	7.84	1.18	0.68	0.26	0.07
828	61.71	23.90	5.32	7.82	1.25	0.68	0.25	0.07
818	61.77	23.83	5.25	7.81	1.34	0.67	0.25	0.08
808	61.84	23.77	5.18	7.79	1.42	0.67	0.25	0.08
798	61.82	23.77	5.19	7.76	1.46	0.67	0.25	0.08
788	61.64	23.92	5.35	7.73	1.37	0.67	0.26	0.08
778	61.47	24.05	5.50	7.70	1.28	0.66	0.26	0.07
768	61.33	24.17	5.63	7.68	1.21	0.66	0.27	0.07
758	61.19	24.27	5.75	7.66	1.14	0.66	0.27	0.06
748	61.08	24.36	5.85	7.64	1.07	0.66	0.28	0.06
738	60.97	24.45	5.94	7.63	1.01	0.66	0.28	0.06
728	60.89	24.52	6.02	7.62	0.96	0.66	0.29	0.05
718	60.99	24.45	5.94	7.69	0.93	0.66	0.28	0.05
708	60.94	24.50	5.99	7.69	0.88	0.66	0.29	0.05
698	60.91	24.53	6.02	7.70	0.84	0.66	0.29	0.05
688	60.87	24.56	6.06	7.71	0.80	0.67	0.29	0.05

K-feldspar

Temperature (°C)	wt% SiO ₂	wt% Al ₂ O ₃	wt% CaO	wt% Na ₂ O	wt% K ₂ O	% ab	% an	% or
798	65.55	19.08	0.45	3.75	11.18	0.33	0.02	0.65
788	65.53	19.04	0.42	3.61	11.40	0.32	0.02	0.66
778	65.52	19.00	0.39	3.49	11.60	0.31	0.02	0.67
768	65.51	18.97	0.36	3.37	11.79	0.30	0.02	0.68
758	65.49	18.94	0.34	3.26	11.97	0.29	0.02	0.70
748	65.48	18.91	0.32	3.16	12.13	0.28	0.02	0.71
738	65.47	18.88	0.30	3.06	12.29	0.27	0.01	0.72
728	65.46	18.85	0.28	2.97	12.44	0.26	0.01	0.72
718	65.47	18.83	0.26	2.92	12.52	0.26	0.01	0.73
708	65.46	18.81	0.24	2.84	12.66	0.25	0.01	0.74
698	65.45	18.78	0.23	2.76	12.78	0.24	0.01	0.74
688	65.44	18.76	0.21	2.68	12.91	0.24	0.01	0.75

Supplementary Table 2 (cont) Rhyolite-MELTS modeling results: feldspar compositions

San Piero (P = 2.3 Kbar; initial water content = 2 wt%; OPX out; Qz-Fa-Mag buffer)

Plagioclase

Temperature (°C)	wt% SiO ₂	wt% Al ₂ O ₃	wt% CaO	wt% Na ₂ O	wt% K ₂ O	% ab	% an	% or
916	59.47	25.50	7.16	7.02	0.86	0.61	0.34	0.05
906	59.75	25.29	6.93	7.12	0.91	0.62	0.33	0.05
896	60.01	25.11	6.71	7.21	0.96	0.62	0.32	0.05
886	60.24	24.94	6.52	7.29	1.01	0.63	0.31	0.06
876	60.45	24.78	6.34	7.35	1.07	0.64	0.30	0.06
866	60.64	24.65	6.18	7.41	1.12	0.64	0.30	0.06
856	60.81	24.52	6.04	7.45	1.18	0.64	0.29	0.07
846	60.97	24.40	5.90	7.49	1.24	0.65	0.28	0.07
836	61.11	24.29	5.78	7.52	1.30	0.65	0.28	0.07
826	61.24	24.19	5.67	7.54	1.37	0.65	0.27	0.08
816	61.32	24.11	5.59	7.52	1.46	0.65	0.27	0.08
806	61.02	24.34	5.84	7.45	1.35	0.64	0.28	0.08
796	60.76	24.54	6.07	7.38	1.26	0.64	0.29	0.07
786	60.51	24.72	6.27	7.32	1.17	0.63	0.30	0.07
776	60.29	24.88	6.46	7.27	1.10	0.63	0.31	0.06
766	60.08	25.04	6.64	7.21	1.03	0.62	0.32	0.06
756	59.91	25.18	6.79	7.16	0.96	0.62	0.32	0.05
746	59.76	25.29	6.92	7.13	0.91	0.62	0.33	0.05
736	59.60	25.41	7.06	7.09	0.85	0.61	0.34	0.05
726	59.88	25.22	6.83	7.22	0.84	0.63	0.33	0.05
716	59.79	25.29	6.92	7.21	0.80	0.62	0.33	0.05
706	59.69	25.37	7.00	7.19	0.75	0.62	0.33	0.04
696	59.63	25.41	7.05	7.18	0.72	0.62	0.34	0.04
686	59.59	25.45	7.09	7.18	0.68	0.62	0.34	0.04
676	59.58	25.47	7.11	7.20	0.65	0.62	0.34	0.04

K-feldspar

Temperature (°C)	wt% SiO ₂	wt% Al ₂ O ₃	wt% CaO	wt% Na ₂ O	wt% K ₂ O	% ab	% an	% or
816	65.47	19.13	0.50	3.71	11.19	0.33	0.02	0.65
806	65.45	19.08	0.47	3.55	11.45	0.31	0.02	0.66
796	65.44	19.04	0.44	3.40	11.68	0.30	0.02	0.68
786	65.42	19.00	0.41	3.27	11.90	0.29	0.02	0.69
776	65.41	18.97	0.39	3.14	12.10	0.28	0.02	0.70
766	65.39	18.93	0.36	3.03	12.28	0.27	0.02	0.71
756	65.38	18.90	0.34	2.92	12.46	0.26	0.02	0.72
746	65.37	18.88	0.32	2.82	12.61	0.25	0.02	0.73
736	65.36	18.85	0.30	2.73	12.77	0.24	0.01	0.74
726	65.38	18.83	0.28	2.72	12.79	0.24	0.01	0.75
716	65.37	18.81	0.26	2.64	12.92	0.23	0.01	0.75
706	65.36	18.78	0.24	2.56	13.06	0.23	0.01	0.76
696	65.35	18.76	0.23	2.48	13.18	0.22	0.01	0.77
686	65.34	18.74	0.21	2.41	13.29	0.21	0.01	0.78
676	65.34	18.72	0.20	2.34	13.40	0.21	0.01	0.78

Supplementary Table 2 (cont) Rhyolite-MELTS modeling results: biotite compositions

San Francesco (P = 2.3 Kbar; initial water content = 2 wt%; OPX out; Qz-Fa-Mag buffer)

Temperature (°C)	wt% SiO ₂	wt% Al ₂ O ₃	wt% FeO	wt% MgO	wt% K ₂ O	wt% H ₂ O
776	42.93	12.14	1.40	28.02	11.22	4.29
766	42.82	12.11	1.98	27.62	11.19	4.28
756	42.68	12.07	2.74	27.09	11.15	4.27
746	42.51	12.02	3.61	26.49	11.11	4.25
736	42.40	11.99	4.23	26.07	11.08	4.24
726	42.34	11.97	4.55	25.85	11.06	4.23
716	42.41	12.00	4.15	26.12	11.08	4.24
706	42.57	12.04	3.33	26.68	11.12	4.25
696	42.67	12.07	2.79	27.06	11.15	4.26
686	42.75	12.09	2.39	27.33	11.17	4.27
676	42.73	12.08	2.49	27.26	11.16	4.27

Sant'Andrea (P = 2.3 Kbar; initial water content = 2 wt%; OPX out; Qz-Fa-Mag buffer)

Temperature (°C)	wt% SiO ₂	wt% Al ₂ O ₃	wt% FeO	wt% MgO	wt% K ₂ O	wt% H ₂ O
768	42.86	12.12	1.79	27.75	11.20	4.28
758	42.73	12.09	2.47	27.28	11.17	4.27
748	42.56	12.04	3.36	26.67	11.12	4.25
738	42.46	12.01	3.90	26.29	11.09	4.24
728	42.35	11.98	4.48	25.90	11.07	4.23
718	42.49	12.02	3.74	26.40	11.10	4.25
708	42.62	12.06	3.03	26.89	11.14	4.26
698	42.72	12.08	2.55	27.23	11.16	4.27
688	42.77	12.10	2.24	27.44	11.18	4.28

San Piero (P = 2.3 Kbar; initial water content = 2 wt%; OPX out; Qz-Fa-Mag buffer)

Temperature (°C)	wt% SiO ₂	wt% Al ₂ O ₃	wt% FeO	wt% MgO	wt% K ₂ O	wt% H ₂ O
776	42.95	12.15	1.32	28.07	11.22	4.29
766	42.85	12.12	1.86	27.70	11.20	4.28
756	42.71	12.08	2.57	27.21	11.16	4.27
746	42.54	12.03	3.48	26.58	11.12	4.25
736	42.44	12.00	3.98	26.24	11.09	4.24
726	42.31	11.97	4.68	25.76	11.06	4.23
716	42.50	12.02	3.69	26.44	11.11	4.25
706	42.62	12.06	3.03	26.89	11.14	4.26
696	42.71	12.08	2.57	27.21	11.16	4.27
686	42.77	12.10	2.24	27.44	11.18	4.28
676	42.74	12.09	2.44	27.30	11.17	4.27

Supplementary Table 3a Zircon saturation temperature modeling (Sant'Andrea granite)

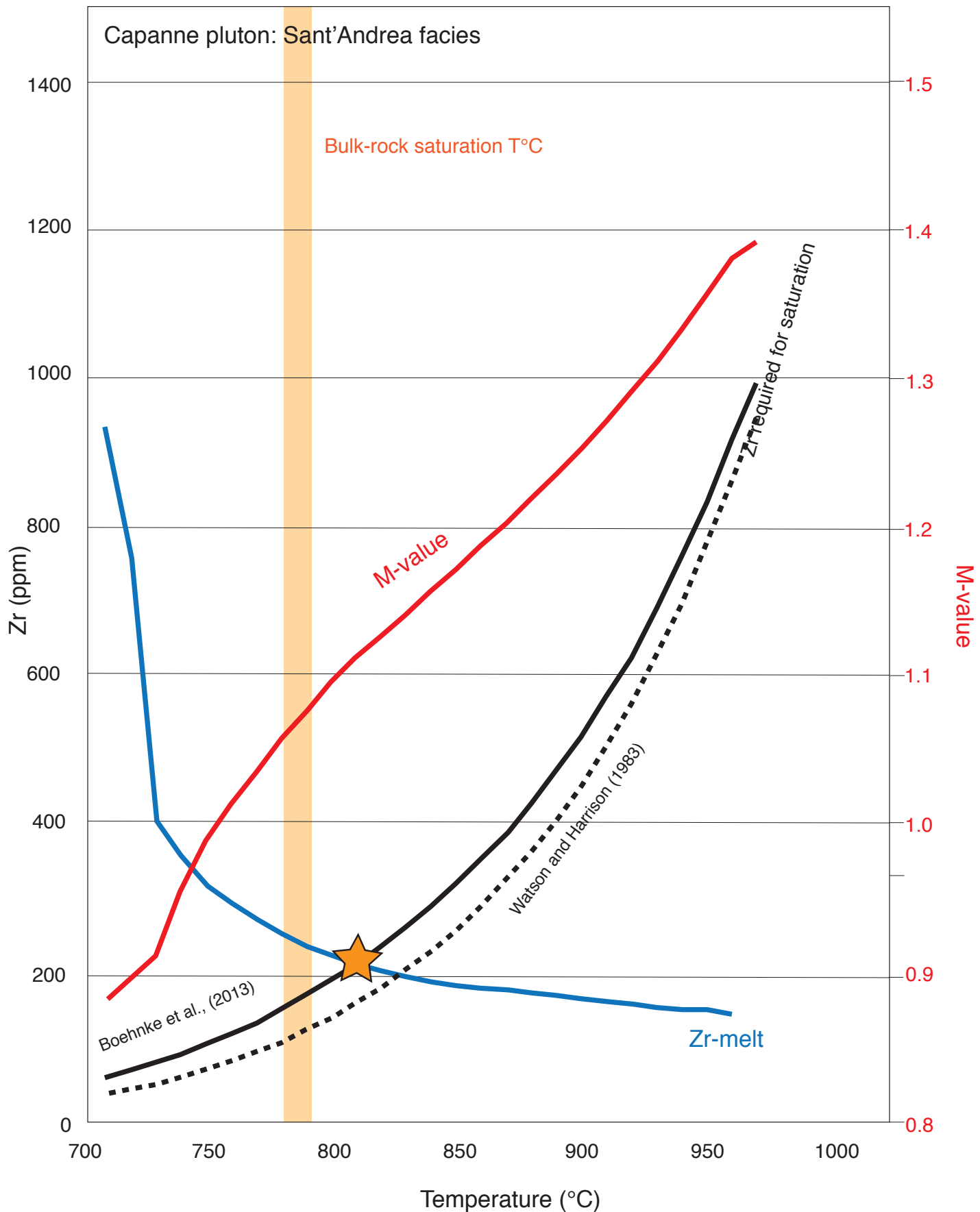
T°C <i>MELTS outputs</i>	M values <i>Calculated from MELTS compositions</i>	Zr for saturation (ppm) <i>Watson and Harrison (1983)</i>	Zr for saturation (ppm) <i>Boehnke et al., (2013)</i>	Zr melt (ppm) <i>using kd's and MELTS outputs</i>
968	1.39	949	1000	-
958	1.38	864	924	145
948	1.36	777	840	149
938	1.34	698	764	152
928	1.31	627	695	156
918	1.29	563	632	160
908	1.27	505	575	163
898	1.26	453	523	167
888	1.24	406	476	171
878	1.22	363	433	174
868	1.20	325	393	178
858	1.19	290	357	181
848	1.17	258	324	185
838	1.16	230	293	188
828	1.14	204	265	196
818	1.13	181	240	204
808	1.11	160	216	212
798	1.10	142	195	223
788	1.08	124	174	238
778	1.06	109	155	255
768	1.04	95	138	274
758	1.02	83	123	296
748	0.99	72	108	319
738	0.96	61	94	359
728	0.91	52	81	404
718	0.92	46	74	761
708	0.88	39	64	931
698	0.86	33	56	1087
688	0.92	31	54	-
Kd K-fld	0.03	<i>Kd from EarthRef.org</i>		
Kd plаг	0.05	<i>Initial melt Zr = bulk rock Zr content (sample PP-334 from Dini et al., 2002)</i>		
Kd quartz	0			
Kd bt	0.432			
Kd cpx	0.278			
Kd ilmenite	0.568			

Supplementary Table 3b Zircon saturation temperature modeling (San Francesco granite)

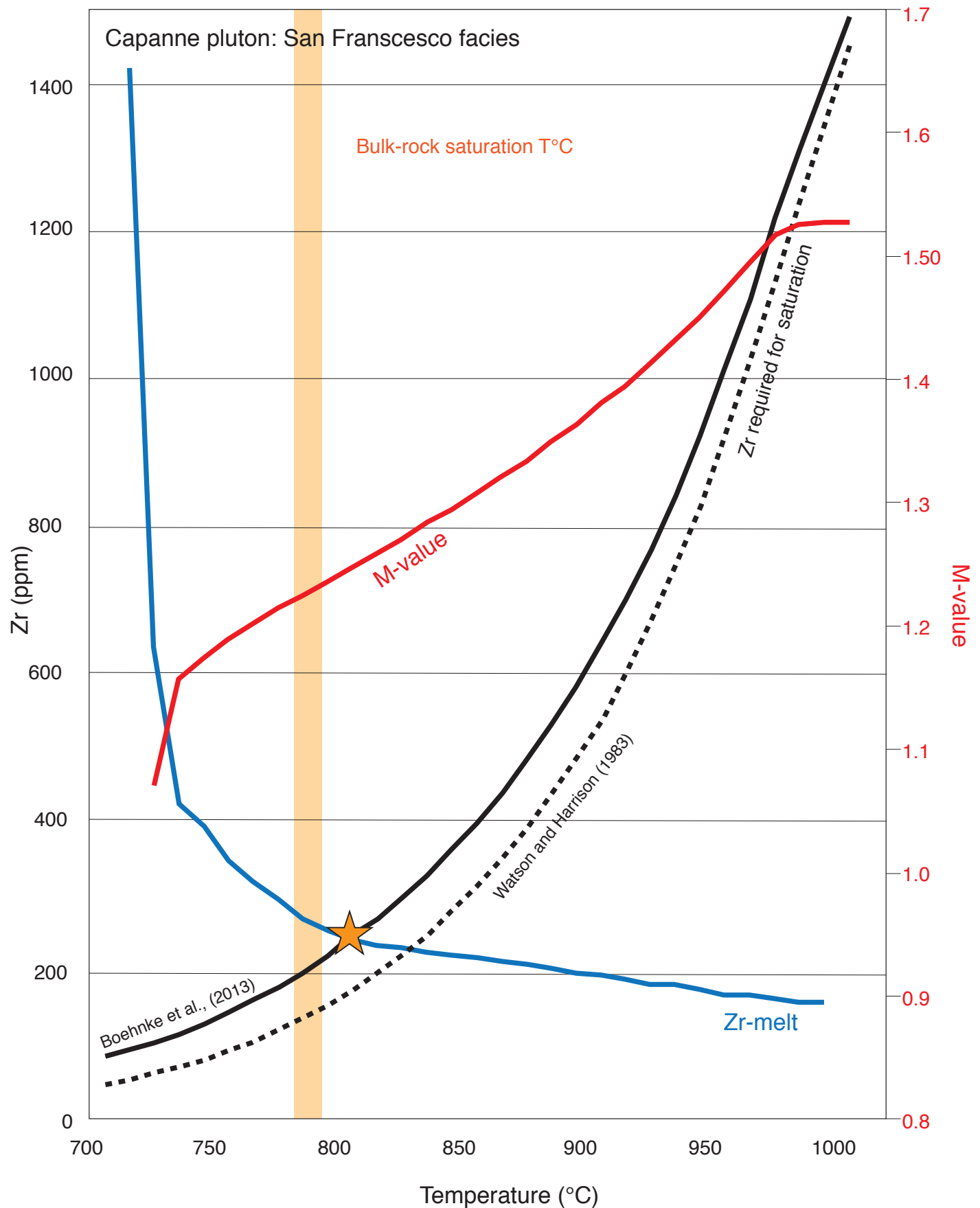
T°C	M values	Zr for saturation (ppm)	Zr for saturation (ppm)	Zr melt (ppm)
MELTS outputs	Calculated from MELTS compositions	Watson and Harrison (1983)	Boehnke et al., (2013)	using kd's and MELTS outputs
1006	1.53	1454	1493	-
996	1.53	1342	1402	160
986	1.53	1237	1315	161
976	1.52	1132	1222	163
966	1.50	1021	1114	167
956	1.47	920	1016	171
946	1.45	830	927	176
936	1.43	748	847	181
926	1.42	674	773	185
916	1.40	607	706	189
906	1.38	546	645	193
896	1.37	490	588	200
886	1.35	440	536	205
876	1.34	395	489	210
866	1.32	353	445	212
856	1.31	316	405	218
846	1.30	282	369	224
836	1.28	252	335	227
826	1.27	224	304	233
816	1.26	199	276	236
806	1.25	177	250	243
796	1.24	157	226	255
786	1.23	138	204	272
776	1.22	122	184	297
766	1.20	107	165	321
756	1.19	94	148	349
746	1.18	82	132	396
736	1.16	72	118	428
726	1.07	58	96	639
716	1.27	60	108	1421
706	1.21	50	92	1761
696	1.19	43	81	2320
686	1.20	38	73	2763
Kd K-fld	0.03	<i>Kd from EarthRef.org</i>		
Kd plag	0.05	<i>Initial melt Zr = bulk rock Zr content (sample PP-364 from Dini et al., 2002)</i>		
Kd quartz	0			
Kd bt	0.432			
Kd cpx	0.278			
Kd illmenite	0.568			

Supplementary Table 3c Zircon saturation temperature modeling (San Piero granite)

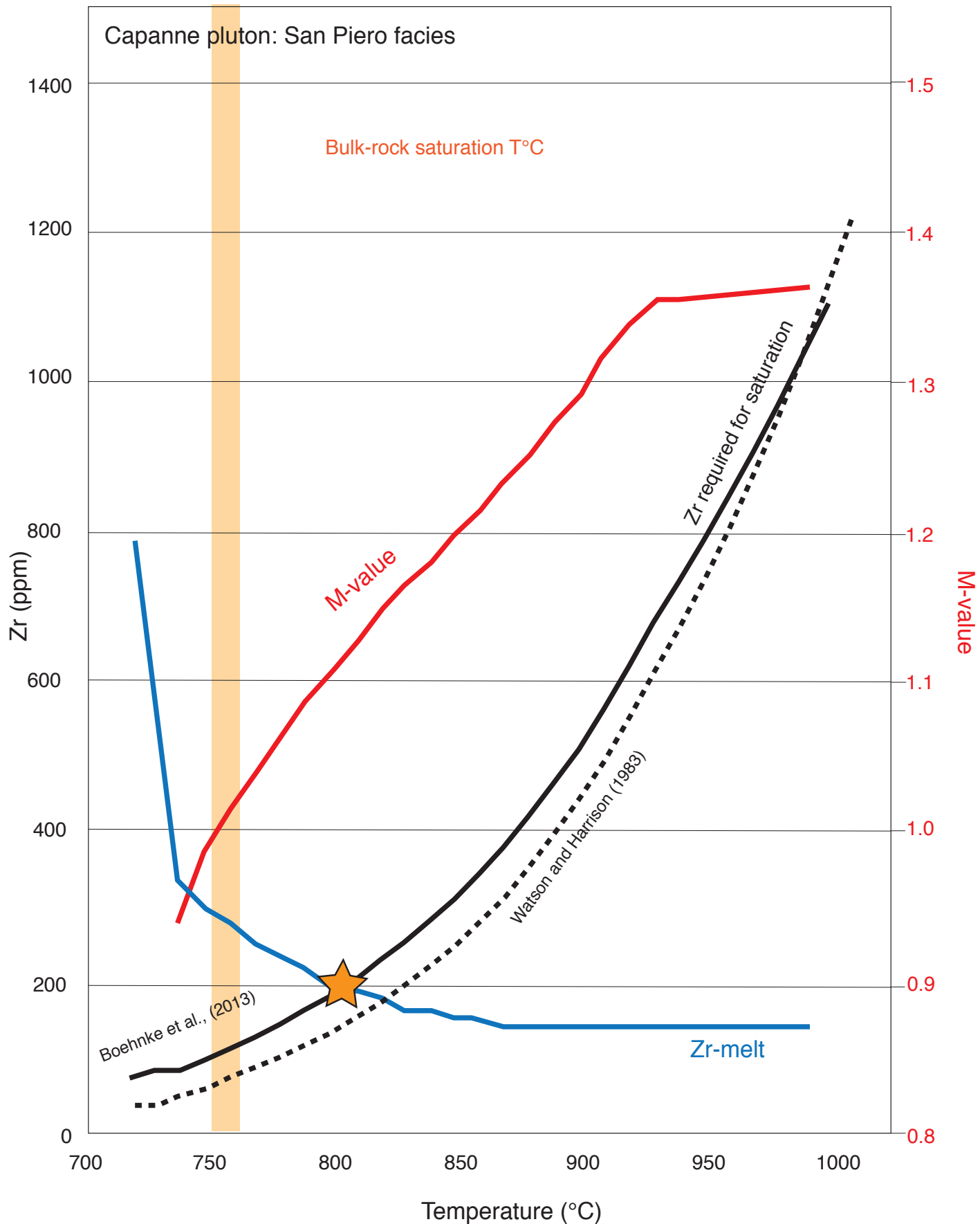
T°C <i>MELTS outputs</i>	M values <i>Calculated from MELTS compositions</i>	Zr for saturation (ppm) <i>Watson and Harrison (1983)</i>	Zr for saturation (ppm) <i>Boehnke et al., (2013)</i>	Zr melt (ppm) <i>using kd's and MELTS outputs</i>
1076	1.33	2070	1787	-
1066	1.33	1928	1690	136
1056	1.33	1793	1597	136
1046	1.33	1666	1508	137
1036	1.33	1546	1422	137
1026	1.33	1433	1339	138
1016	1.33	1326	1260	138
1006	1.33	1225	1184	139
996	1.33	1131	1112	139
986	1.33	1042	1042	140
976	1.33	959	976	140
966	1.33	882	913	140
956	1.33	809	853	141
946	1.32	741	796	141
936	1.32	678	741	142
926	1.32	619	689	142
916	1.30	558	631	144
906	1.28	500	573	146
896	1.26	447	520	149
886	1.24	400	472	151
876	1.23	358	428	153
866	1.21	319	388	156
856	1.19	285	352	158
846	1.17	253	319	161
836	1.16	225	289	165
826	1.14	200	261	169
816	1.13	177	236	176
806	1.11	157	212	189
796	1.09	138	190	202
786	1.07	121	170	216
776	1.05	106	151	232
766	1.03	92	134	253
756	1.00	80	119	274
746	0.98	69	105	297
736	0.93	59	90	343
726	1.01	55	89	540
716	0.99	48	79	794
706	0.97	41	69	985
696	0.96	36	62	1169
686	0.99	32	57	1421
<i>Kd K-fld</i>				
Kd K-fld	0.03	<i>Kd from EarthRef.org</i>		
Kd plag	0.05	<i>Initial melt Zr = bulk rock Zr content (sample MB11-2)</i>		
Kd quartz	0			
Kd bt	0.432			
Kd cpx	0.278			
Kd illmenite	0.568			



Supplementary Fig. 3a. Zr saturation model (Sant'Andrea facies)



Supplementary Fig. 3b. Zr saturation model (San Franscesco facies)



Supplementary Fig. 3c. Zr saturation model (San Piero facies)